DEVELOPMENT OF A LOW-COST BIOPRINTING SYSTEM FOR THE FABRICATION OF CELL-LADEN SODIUM ALGINATE HYDROGELS

A thesis submitted in fulfilment of the
requirements for the degree of

MASTER OF SCIENCE

of

RHODES UNIVERSITY

By

JOHN ROBERT HONIBALL

February 2017

Declaration

I declare that this thesis is my own, unaided work. It is being submitted for the degree of Master of Science of Rhodes University. It has not been submitted for any degree or examination at any other university.

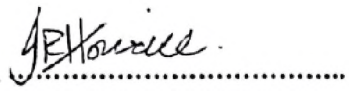

Mr John Robert Honiball

Abstract

Bioprinting is a rapidly expanding technology with the ability to fabricate *in vitro* 3D tissues in a layer-by-layer manner to ultimately produce a living tissue which physiologically resembles native *in vivo* tissue functionality. Unfortunately, large costs associated with commercially available bioprinters severely limit the amount of people/research groups with access to the technology. Here, we investigated the potential for modifying a commercially available RepRap Prusa iteration 3 (i3) three-dimensional (3D) printer, by replacing the traditional plastic-based print-head with various open-source syringe-housed microextrusion print-head units, such that deposition of composite bioinks consisting of cells, biopolymer scaffolds and/or biomolecules may be achieved at a relatively low cost. Using adipose-derived human mesenchymal stromal stem cells (ad-HMSC) induced for adipogenic differentiation, as well as human umbilical vein endothelial cells (HUVEC), the potential for fabricating vascularised adipose tissue was investigated. The non-toxic, inexpensive algal polysaccharide, sodium alginate, was used to test the printability of the system, as well as for investigating the functionality unmodified sodium alginate has for use as a potential bioink in adipose tissue engineering. Cell viability assays, namely WST-1 and fluorescein diacetate (FDA)/propidium iodide (PI) live/dead cell staining, revealed that ad-HMSC were viable after 7 days of culture. However, viability of HUVEC encapsulated hydrogels revealed significantly lower cell viability. Live/dead cell staining revealed that the modified printing system was able to print ad-HMSC/HUVEC co-cocultures with a large degree of cell viability after 1 day of culture. However, after 7 days of culture, the majority of cells were revealed to be dead. Furthermore, due to the lack of mechanical integrity possessed by alginate in a liquid-like state, printing sodium alginate hydrogels in air consistently resulted in deformation of printed constructs. The newly developed 3D printing technique termed freeform reversible embedding of suspended hydrogels (FRESH) was therefore investigated as a means for achieving 3D spatial control of printed hydrogels using the modified system. Printing cell-free sodium alginate hydrogels within gelatin sacrificial support baths allowed for fabricating constructs in a spatially defined manner. However, overprinting and swelling of alginate hydrogels negatively affected the overall printing accuracy. The present study aimed to pave the way for further system modifications and refinements, such that the ultimate goal of low-cost bioprinting may be achieved. Further optimisation of printing parameters, hydrogel

characteristics and sterilisation techniques may allow for fabricating viable, physiologically relevant tissues using the modified system developed.

Acknowledgements

I would firstly like to thank my supervisor, Dr Earl Prinsloo, for all of the assistance and motivation he has provided me over the years. I would like to thank Distinguished Prof Tabello Nyokong and Marcel Louzada for their eagerness to help. I would like to thank my father, Andrew, my mother, Mariana, and my step-mother, Nikki, for all of their emotional and financial support without which I would not have been able to complete my tertiary education. I acknowledge my laboratory colleagues, Pascalené, Lebohang, Sinethemba and Rose, for all of their help, guidance and friendship. Last but not least, I would like to thank Ada & Bertie Levenstein, as well as the National Research Foundation for financial support throughout my post-graduate studies.

Outputs

Conference Outputs

Prinsloo, E., Honiball, J.E., Makhene, L., Kadye, R. (2016). Development of Additive Manufacturing Technologies for Engineering *in vitro* Adipose Tissue Constructs. Indian Ocean Rim Muscle Colloquium, 24-26 January 2016, Asara Wine Estate, Stellenbosch, South Africa – Oral Presentation.

Prinsloo, E., Kramer, A.H., Joos-Vandewalle, J., Honiball, J.R. (2014). Development of Novel Real-Time Methodologies for the *in vitro* Monitoring of Cellular Differentiation. International Conference of Tissue Engineering & Regenerative Medicine (ICTERM), 27-31 August, 2014, Tshwane University of Technology, Pretoria, South Africa – Oral Presentation.

Table of Contents

List of Figures

List of Tables

List of Equations

List of G-codes

List of Abbreviations

2D	Two-Dimensional
3D	Three-Dimensional
ad-HMSC	Adipose-derived Human Mesenchymal Stromal Stem Cells
AM	Additive Manufacturing
ad-SC	Adipose-Derived Stem Cell
AFM	Atomic Force Microscopy
AIM	Adipogenic Induction Media
AMM	Adipogenic Maintenance Media
AMP	Adenosine Monophosphate
bm-MSC	Bone Marrow-Derived Mesenchymal Stromal Cells
C/EPB	CCAAT/Enhancer Binding Proteins
CAD	Computer-Aided Design
Cat. No.	Catalogue Number
CI	Cell Index
CT	Computer Tomography
DAPI	4',6-Diamidino-2-Phenylindole
dd	Double Deionized
dECM	Decellularised Extracellular Matrix
DMEM	Dulbecco's Modified Eagle Medium
DMSO	Dimethyl Sulfoxide
DPBS	Dulbecco's Phosphate Buffered Saline
dsRed	Red Fluorescent Protein
ECGM	Endothelial Cell Growth Medium
ECGS	Endothelial Cell Growth Supplement
ECM	Extracellular Matrix
	Endothelial Cell Medium
EGM	Endothelial Growth Media
FAK	Focal Adhesion Kinase
FBS	Foetal Bovine Serum
FDA	Fluorescein Diacetate
FGF-2	Fibroblast Growth Factor 2
FITC	Fluorescein Isothiocyanate
FL	Fluorescence
FRESH	Freeform Reversible Embedding of Suspended Hydrogels
GelMA	Gelatin Methacrylate
hADSC	Human Adipose Tissue Stromal Cells
HUVEC	Human Umbilical Vein Endothelial Cells
IBMX	3-Isobutyl-1-Methylxanthine
IGF-1	Insulin-like Growth Dactor-1
iPS	Induced Pluripotent Stem Cell

LED	Light Emitting Diode
MAPK	Mitogen-activated Protein Kinase
MCPs	Multipotent Cardiovascular Progenitor cells
MRI	Magnetic Resonance Imaging
MSC	Mesenchymal Stem Cells
MSCGS	Mesenchymal Stem Cell Growth Supplement
MSCM	Mesenchymal Stem Cell Media
OIM	Osteogenic Induction Media
P/S	Penicillin/Streptomycin
PBS	Phosphate Buffered Saline
PDMS	Poly(Dimethylsiloxane)
PEG	Poly(ethylene) Glycol
PEGDMA	Poly(ethylene glycol) Dimethacrylate
PI	Propidium Iodide
PKA	Protein Kinase A
PPARγ	Peroxisome proliferator-activated receptor-gamma
PSA	Penicillin/Streptomycin/Amphotericin B
RepRap	Replicating Rapid Prototyper
RGD	Arginine-Glycine-Aspartic acid
rpm	Revolutions Per Minute
RTCA	Real-Time Cell Analyser
SP	Single Plate
STL	STereoLithography
USA	United States of America
USD	United States Dollar
UV	Ultraviolet
v	Volume
VEGF	Vascular Endothelial Growth Factor
w	Weight
ZAR	South African Rand
α-MEM	Minimum Essential Medium Eagle Alpha Modification

List of Symbols

%	Percent
µL	Microlitre
µM	Micromolar
µm	Micrometre
cm	Centimetre
E	Young's Modulus
g	Gram
G'	Storage Modulus
G'	Storage Modulus
G''	Loss Modulus
G''	Loss Modulus
kPa	Kilopascal
L	Litre
M	Molar
mL	Millilitre
mm	Millimetre
mM	Milimolar
nM	Nanomolar
^{o}C	Degrees Celsius
Pa	Pascal
X	Times

Chapter 1: Literature Review

1.1 Introduction

With the rapid growth of the global human population, donor organs are becoming increasingly sought after, but remain in short supply. The result is that every year thousands of patients are unable to receive organ transplants due to the lack of available organs (Marga *et al.*, 2012). However, recent advances in medical science, particularly in tissue engineering, have sparked the potential to revolutionise the way in which tissues/whole organs may be obtained, namely by engineering the required tissue/organ. Tissue engineering is a field which utilises a multitude of disciplines. Representing the convergence of science, engineering and clinical disciplines, tissue engineering aims to study the biology of a tissue/whole organ with respect to its development, homeostasis and repair, such that tissue/organ functionality may be re-established (Campbell & Weiss, 2007). Tissue engineering addresses two important aspects of biomedical science; both patient-specific therapies as well as drug discovery research are at the core of tissue engineering innovation and have benefited and will continue to benefit from discoveries made within the field. In terms of patient-specific therapies, major advances made through fabricating specific tissues, using patient-derived cells, eliminates the waiting period for finding appropriate donors. The risk of organ rejection by the recipient patient's immune system is also greatly reduced (Vacanti & Langer, 1999). Aside from patient tissue/organ replacement therapies, innovations in tissue engineering have the potential to address the ethical concerns related to the use of animals as models for disease. The ability to produce *in vitro* tissues expressing disease phenotypes has proven to not only be more relevant and low-risk than utilising animals as models for human diseases but also costs less than maintaining excised animal tissues for extended periods of time (Elliott & Yuan, 2011). It is understood that the field of tissue engineering evolves in a manner which is largely dependent on its parent disciplines. Thus, with the global popularity and accessibility of three-dimensional (3D) printing technology, a newly developed technology termed "bioprinting" has gained major worldwide attention. In order to understand bioprinting, a brief understanding of conventional 3D printing is required. Three-dimensional printing is defined as the process of developing three-dimensional objects through additive layering of a given material (Calvert, 2001). Three-dimensional printers have the ability to create virtually any type of design, depending on the 3D printable files they read. This additive production approach

for fabricating constructs is unique compared to traditional manufacturing approaches which often involve subtractive processes such as sculpting or milling. With 3D printing the manufacturer has access to all three Cartesian (X, Y and Z) coordinates. This allows for the fabrication of constructs which can only be produced through additive manufacturing technologies (Miller, 2014). Due to the technology becoming increasingly available and affordable, research groups have put great interest into designing components for modifying 3D printers to perform certain tasks. One such task is the controlled fabrication of biological materials to form 3D tissue structures. This technology is termed bioprinting and is defined as the deposition of living cells, extracellular matrix (ECM) components, biochemical factors, biomaterials and/or scaffold materials through the use of printing technology (Campbell & Weiss, 2007; Tasoglu & Demirci, 2013). Bioprinting allows for delivering cells in a defined and organised manner due to the control of cell densities, constituents of the cellular microenvironment and also deposition characteristics (cell patterning). The following review of literature aims to describe and critique 3D tissue engineering as well as fundamental bioprinting in terms of recent technologies and techniques, with the focus on that of fabricating soft adipose-tissue.

1.2 Three-dimensional (3D) Tissue Engineering

Most research involving cells has traditionally assumed that cellular monolayers largely reflect native chemical and physical properties associated when cells are present in living tissues (Pampaloni *et al.*, 2007). Mammalian cells are most commonly grown as 2D monolayers using hard materials such as glass or plastic as substrate. A major downside to this method lies in the fact that several micro- and macro-interactions taking place when cells are present in native tissues do not in fact occur when cells are grown in monolayers. Biochemical processes such as cell-cell interactions as well as cellular architectures (variability in 3D structure) seen in tissue specific cell-types do not get accurately reflected when cells are grown in monolayers using simplified substrates (Huh *et al.*, 2011). For example, fibroblasts cultured on 2D substrates have been shown to have different shapes and distribution of adhesion proteins compared to when they are cultured on 3D collagen scaffolds (Cukierman *et al.*, 2001; Meshel *et al.*, 2005). Assumptions made regarding cellular processes are therefore more accurate when cell-based data is obtained from tissues with physiological characteristics nearly identical to those in the living

organism. This was first demonstrated in 1992 when Bissell and co-workers showed how culturing human breast epithelial cells in monolayer produced tumor-like cells, however when transferred to 3D cell culture, reverted back to normal growth behaviours (Petersen *et al.*, 1992).

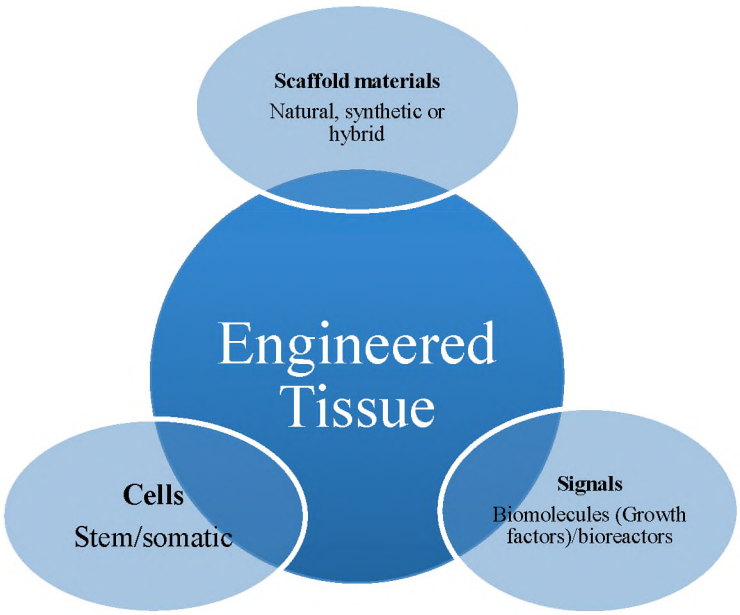

Figure 1.1: Requirements for tissue engineering. The triad of cells, scaffold materials (for cell attachment and migration) as well as signalling factors (such as growth factors or bioreactors) are all required to produce living tissues through tissue engineering techniques. (Adapted from O'Brien, 2011).

The advent of engineering 3D tissue cultures thus provides an alternate and more relevant means for analysing cells by reducing the gap between *ex vivo* cell cultures and near physiologically-identical tissues (Pampaloni *et al.*, 2007). Furthermore, engineering 3D tissues designed to behave as diseased tissue may provide far better insights as to how to prevent or cure certain diseases. A clearer understanding of disease progression may be obtained. As an example, Alzheimers diseased models have traditionally relied on employing 2D neuronal tissue cultures for the study of neuron loss induced by beta amyloid (Kar *et al.*, 2004). However, the lack of pathophysiological characteristics present in 3D *in vivo* neuronal tissue has motivated researchers to produce 3D *in vitro* tissues which may be used as stable models for the disease. Choi *et al.* (2013) demonstrated how networked neurospheres, sensitive to beta amyloid, can be produced through simply culturing neural progenitors in concave poly(dimethylsiloxane)

(PDMS) molds. Grown in PDMS molds, the neurospheres produced displayed far greater neuron interaction when compared to cells grown in 2D culture. Such innovations may therefor significantly improve the turnover time associated with new drugs undergoing pharmaceutical trials. Further to this, the use of animals as models for disease may significantly be reduced if 3D tissues are used as the primary subject for undergoing drug discovery/testing (Huh *et al.*, 2011). At the core of tissue engineering are three fundamental considerations; the triad of living cells, biomaterial scaffold material and growth factors/bioreactors are all required for successful tissue formation/regeneration (Figure 1.1.) (O'Brien, 2011; Miller, 2014). Scaffolds used in tissue engineering are generally highly porous 3D substrates which provide a surface for cells to adhere to and multiply within. Survival of cells within a scaffold relies on scaffold dimensions and architectures determined by characteristics such as pores sizes and channels (Derby, 2012). The scaffold microarchitecture ought to reflect the native tissue architecture. Hence, an understanding of native tissue ECM chemical/physical characteristics provides an accurate means for understanding the requirements cells have for producing physiologically relevant *in vitro* tissues. Tissue engineers thus require tweaking or altering certain scaffold materials by changing their mechanical properties or structural modifications at the nano-scale, which may ultimately direct cell attachment (surface adhesion), proliferation or differentiation. For a scaffold to be of use for tissue engineering applications, several considerations need to be considered prior to the introduction of cells. Scaffolds ought to be designed to be biocompatible, biodegradable and have mechanical properties in-line with that of the tissue to be fabricated. Moreover, scaffold architecture ought to allow for cell attachment and proliferation (Chen *et al.*, 2002; O'Brien, 2011).

1.3 Biotechnological Applications of Three-dimensional (3D) Tissues

1.3.1 Tissue/Organ Replacement Therapy

Several diseases, such as cancer or trauma, often results in tissue/organ damage so severe that conventional pharmaceutical treatments are no longer applicable. In such cases, artificial tissues/organs or whole organ transplantation become the first choice of treatment (Ikada, 2006). However, tissue/organ replacement therapy is not as straight forward as it may sound. Apart from the large amount of money required to perform such treatments, largely due to the high

demand for donated organs, immune rejection by the organ recipient is not uncommon (Vacanti & Langer, 1999). There have been major efforts from researchers in the biomedical industry and academia to better understand what is required for initiating and maintaining biocompatibility and biofunctionality of replaced tissues/organs. A recent and promising approach for functional organ replacement is that of decellularisation of allogeneic or xenogeneic organs, providing a naturally occurring 3D biological scaffold which subsequently gets recellularised through seeding of selected cell populations. Decellularisation employs detergents, salts, enzymes and/or physical treatments for removing cells from tissues/whole organs such that an ECM scaffold with native tissue architecture, bioactivity and mechanical integrity may be utilised for tissue engineering (Badylak *et al.*, 2011; Scarritt *et al.*, 2015; Jung *et al.*, 2016). Where transplantation of organs (such as the heart, liver and lung) require an intact vascular network before transplantation, this decellularisation/recellularisation approach becomes highly valuable due to the opportunity for direct vasculature connection to the patient. Challenges to this approach remain in that selecting optimal decellularisation approaches and recellularisation techniques as well as selecting appropriate cell populations and bioreactors require better understanding for individual organs (Badylak *et al.*, 2011). A recently developed and attractive approach for maintaining *in situ* organogenesis was initiated through the discoveries made by Shinya Yamanaka and his team in 2006, when it was shown how to obtain induced pluripotent stem cells (iPS cells) from somatic cell sources (Takahashi & Yamanaka, 2006). This major advancement in the field of stem cell biology has opened up the possibility for producing personalised organs. Through decellularisation of ECM scaffolds and subsequent recellularisation using a patient's own iPS cells, proliferation of the cells within the intact ECM may promote the generation of certain tissues *in situ* (Jung *et al.*, 2016). This was demonstrated by Lu *et al.* (2013), where decellularised mouse heart was recellularised with human iPS-derived multipotent cardiovascular progenitor cells (MCPs). The group showed how recellularised MCPs migrate, proliferate and differentiate into cardiomyocytes, smooth muscle cells and endothelial cells which exhibit spontaneous contractions as well as drug responses.

1.3.2. Drug Discovery

Animals have been used as models for human disease for several decades. Apart from the ethical concerns regarding the in-humane means drug discovery research is being conducted on animals,

the relevance and feasibility of using animal models has been put to question due to differences in genetic make-up as well as cost and potential complications associated with maintaining excised tissue viability (Elliott & Yuan, 2011). One of the major advantages of using animals as models for human diseases lies in the ability to perform multi-organ response systems. However, these systems often require the use of knockout or transgenic animals to have relevance in a physiological or pathophysiological response, ultimately leading to further complications and potential shortcomings (Ghaemmaghami *et al.*, 2012). An alternative to the use of animal models has been to develop *in vitro* tissue models for the study of disease and drug efficiency. Such models can be more tightly controlled in terms of their exposure to biochemical factors and are usually less expensive and time consuming compared to animal models (Elliott & Yuan, 2011). Two-dimensional (2D) monolayer culturing of cells is the most commonly used *in vitro* method for analysing cell-based data. As previously described, several intrinsic limitations including the inability to fully recapitulate native cellular architectures, experienced *in vivo*, severely limit the validity of relying solely on 2D culture systems for the study of human diseases and drug responses. Hence, compared to 2D models, 3D tissues provide a far more relevant means for studying disease progression and drug efficiencies, largely due to the increase in cell-cell and cell-ECM interactions (Ghaemmaghami *et al.*, 2012). Recent advances in microengineering have sparked the development of the next wave of 3D cell culture models. "Organs-on-chips" systems, which have gained major world-wide attention, are attractive candidates for conducting drug discovery techniques due to their dynamic mechanical properties and biochemical functionalities of whole living organs. These "organ-on-a-chip" systems integrate cells fabricated and cultured on electronic 3D microchip devices with microfluidic technologies, enabling the study of human physiology in an organ-specific context. As such, *in vitro* disease models can be specifically engineered for human diseases (Huh *et al.*, 2011).

1.4 Bioprinting

A bioprinter produces 3D tissues or whole organs by layering several 2D Cartesian plane bioink (i.e. material which is deposited about the XYZ positioning during bioprinting processes) slices on top of one another to produce a fabricated living construct (Murphy & Atala, 2014) (Figure 1.2). Bioprinting technology is defined as the use of printing technology to deposit living cells, ECM components, biochemical factors, proteins, drugs and/or biomaterials on a receiving solid

or gel substrate or liquid reservoir (Mironov *et al.*, 2008; Tasoglu & Demirici, 2013; Pati *et al.*, 2015). The technology could potentially lead to the development of fully functional tissues or organs, eliminating the need for tissue grafts or mechanical devices to be used on patients (Okabe *et al.*, 2009). The bead of material created is directed by computer-aided design (CAD) software, controlled by a computer. This allows for the fabrication of biomimetic-shaped 3D structures from medical images such as computer tomography (CT) and magnetic resonance imaging (MRI) scans (Seol *et al.*, 2014). Major challenges involved with bioprinting of 3D tissues include adapting conventional 3D printing technologies using plastics and metals to the printing of living biological materials which are sensitive in nature. Formulation and design of a bioink which resembles native cellular ECM characteristics as well as architectural organisation remains the core challenge faced by researchers in the field (Murphy & Atala, 2014). There has recently been a great increase in the number of companies manufacturing commercially available bioprinters. The range of printable materials, printing speed and resolution all favour the use of commercially available systems such as those created by Organovo and EnvisionTEC (Marga *et al.*, 2012). However, very high prices associated with bioprinters create a demand for novel technologies which are able to perform similar functions. Modifying conventional 3D printers to allow for construction of 3D tissues has therefore been the focus of several research groups aiming to engineer tissues at relatively low cost.

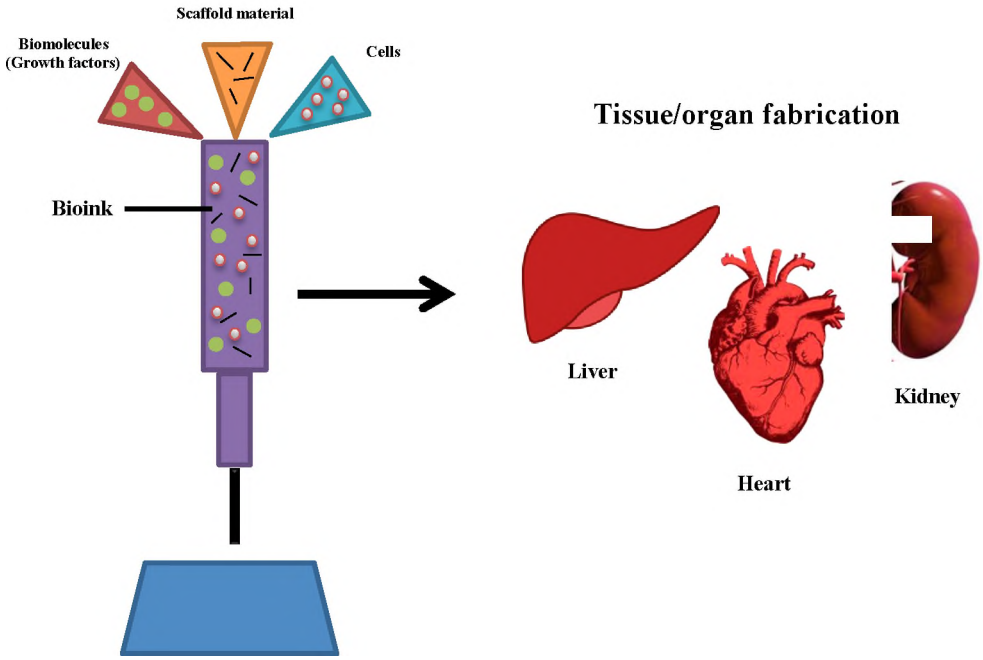

Figure 1.2: The bioprinting process. Bioprinting involves the deposition of cells, scaffold materials and biological molecules to fabricate three-dimensional tissues and organs in a spacially defined manner (Adapted from Seol *et al.*, 2014).

1.4.1 Comparison of Bioprinting to Decellularisation/Recellularisation

Treating patients with kidney failure, requiring arteriovenous access for hemodialysis, or patients with cardiovascular disease, requiring arterial bypass, largely relies on vascularised autologous tissue grafts for tissue/organ repair. However, some patients may lack suitable autologous tissue when a patient's own vasculature cannot be used for grafting, due to the tissue being diseased or because suitable vasculature has already been harvested (Dahl *et al.*, 2011). Such patients could benefit greatly from vascularised tissue grafts produced by tissue engineering. Decellularisation/recellularisation of ECM scaffolds, as well as 3D bioprinting of tissue constructs, have the potential for creating *ex vivo* tissues/whole organs utilisable by patients requiring tissue repair or organ replacement. However, depending on the type of tissue to be transplanted, several considerations may favour one regenerative approach over the other. A key advantage of bioprinting over organ decellularisation lies in the ability of bioprinters for achieving spatial control of cells, scaffold materials and biomolecules. Due to the nature of the technology, that being fabricating tissue in a layer-by-layer manner from the bottom up, bioprinting is able to place cells and biomaterials at precise locations with high resolution. Moreover, the ability to tailor bioinks, through incorporating signaling molecules or controlling mechanical properties, improves the flexibility of the technology such that a wide range of materials may be printed (Murphy & Atala, 2014). In contrast, while organ decellularisation approaches provide nearly identical structures to native tissues, largely dependent on cellular perfusion, control of cell attachment, mobility and differentiation is far more difficult to control in decellularisation/recellularisation approaches when compared to bioprinting techniques (Jung *et al.*, 2016). The potential for creating patient-specific organ replacement therapies also favors the use of bioprinting technologies. The ability to obtain whole organ imaging data (via the use of magnetic resonance imaging scans, as an example) allows for fabricating tissues with the exact shape and size of the organ/tissue which needs repair or replacing (Seol *et al.*, 2014). Concerns over incorrect organ incorporation are thus reduced. However, fabrication of near-physiologically identical whole organs is still a long road away. While thin tissues require comparatively few cells for enabling cellular proliferation, which often times enables normal tissue function, thin tissues do not necessarily compensate for a whole organ. Whole organ replacements require major scaling up of cellular densities if solid, functional organs are to be

properly incorporated into patients. Replacement of solid organs requires cell densities in the range of 1-10 billion functioning cells and achieving such densities remains a key challenge for experts within the field (Miller, 2014). The debate whether the form of an organ is necessarily required for organ function will be pivotal in the future of tissue engineering innovation. Clearer understanding as to what the exact anatomical components are required for tissue functionality will provide insight as to which means for producing functional tissues may be used most effectively and tissue engineers are currently presented with multiple approaches for producing such tissues (3D bioprinting, organ decellularisation/recellularisation and organ-on-a-chip systems). Another key consideration in tissue engineering is that of immune rejection of transplanted organs. A major drawback to traditional organ transplantation is the requirement recipient patients have for life-long immunosuppression (Scarritt *et al.*, 2015). Decellularisation/recellularisation as well as bioprinting approaches have the opportunity to reduce the need for such continuous immunosuppression. Immune rejection is considered to be more prevalent with decellularisation/recellularisation approaches when compared to bioprinting technologies. However, immunogenicity in 3D bioprinting remains relatively unexplored. Physical, chemical or enzymatic decellularisation of organs involves eliminating most immunological components (such as the major histocompatibility complex (MHC) and the human leukocyte antigen (HLE)) and other genetic material from the tissue (Jung *et al.*, 2016). However, lack of immunological components may still result in immune rejection of a transplanted organ by the recipient. In contrast, bioprinting technology allows for incorporating immunological components when designing bioink materials. Immunological responses in recipient patients may thus be outright avoided when including immunomodulatory agents in bioink materials (Jung *et al.*, 2016). Yet another example of where the use of patient-derived and differentiated iPS cells becomes highly valuable. Research into the exact immunological components required for proper organ transplantation requires a far better understanding than what is currently known. However, one thing that is clear is that flexibility in organ design is far more prevalent through the use of bioprinting technologies when compared to methods for organ decellularisation and recellularisation.

1.5 Bioprinting Technologies

The most widely used technologies for depositing and patterning biological materials through bioprinting include jetting-based and valve-based (microextrusion) bioprinting (Figure 1.3; Derby, 2012; Khatiwala *et al*., 2012; Tasoglu & Demirci, 2013).

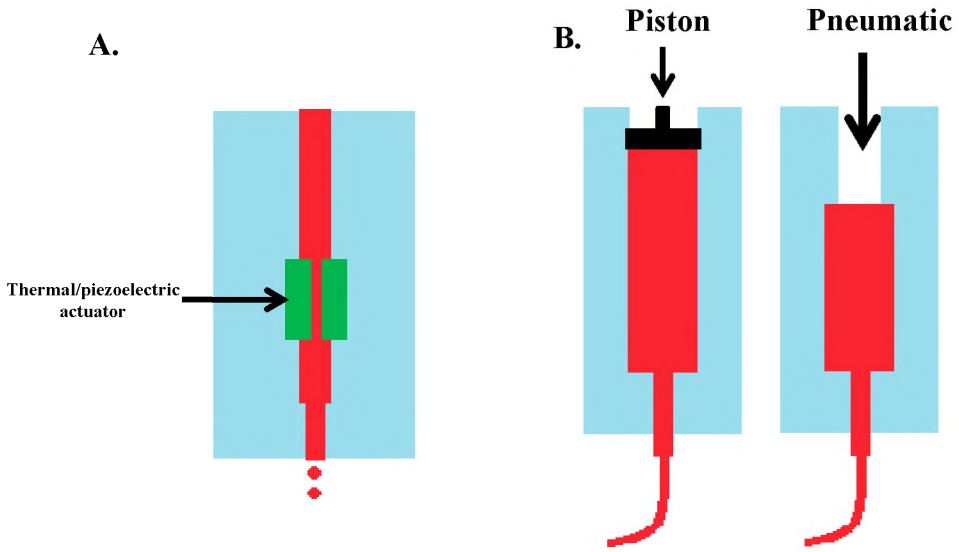

Figure 1.3: Bioprinting technologies. A: Inkjet and B: Microextrusion bioprinting techniques. (Adapted from Murphy & Atala, 2014).

1.5.1 Jetting-based Bioprinting

Jetting-based (often referred to as inkjet bioprinting) involves the deposition of picolitre bioink droplets layered onto a substrate in a non-contact method (Mironov *et al*., 2009). This printing technology is the most widely used for biological (and non-biological) applications and can be characterised according to its mechanism of bioink droplet formation. The most widely used mechanisms for jetting-based bioprinting is that of thermal and piezoelectric-based printers (Figure 1.3 A.). Thermal inkjet printers work by electrically heating the print head such that pressure in the nozzle force bioink droplets from it. Piezoelectric-based inkjet printers contain

piezoelectric crystals which produce acoustic waves, dividing the bioink into droplets within the print head. Other, less popular, mechanisms for jetting-based bioink deposition include laser-induced forward transfer, pneumatic pressure and valve-based bioprinting systems (Murphy & Atala, 2014; Seol *et al.*, 2014; Atala & Yoo, 2015). Major advantages for employing jetting-based bioprinting technology lies in the high resolution constructs the picolitre-sized bioink droplets form. However, printing at high resolutions requires the time of printing to significantly increase. This is seen as a disadvantage when it comes to bioprinting as some tissues/cell types fail to live outside of a humidified environment for a very long period of time (Seol *et al.*, 2014). Another key disadvantage to the technology is its limitation in materials which may be printed. Picolitre-sized bioink droplets cannot be readily obtained from high-viscosity materials. Low-viscosity materials such as saline, thrombin and fibrogen are thus most commonly required for successful fabrication of tissue constructs. This limits the range of tissues and cell types which may be printed using the technology (Cui & Boland, 2009; Khalil *et al.*, 2009).

1.5.2 Extrusion-based Bioprinting

Extrusion-based bioprinting involves the robotically controlled deposition of materials onto a substrate through a microextrusion head. Microextrusion bioprinters allow for layering several biocompatible materials such as hydrogels, copolymers and cell spheroids to fabricate 2D or 3D structures (Peltola *et al.*, 2008). Extruding materials using microextrusion technology is achieved by either pneumatic or mechanical means (Figure 1.3 B.). Both have advantages and disadvantages associated with spatial control and pressure changes during extrusion. For example, mechanically driven extrusion involves more complex components which allow improved spatial control of materials compared to pneumatically driven microextruders which have a delay in the volume of compressed gas. The simpler, less complex drive mechanics of pneumatically driven printers may be considered an advantage over mechanically driven printers (Murphy & Atala, 2014). A requirement for producing functional tissues is maintaining high cell viability after printing. Viability following extrusion using mechanically driven systems results in lower survival rates compared to when cells are extruded using inkjet-based systems. This is likely due to the increased stresses cells undergo while being extruded in a viscous fluid. In order to maintain cell viability, extrusion pressures ought to be low and nozzle sizes fairly large. Print resolution will however be negatively affected by this strategy (Murphy & Atala, 2014). To date

there have been various tissue types fabricated using bioprinting technologies. Table 1.1 highlights some of the tissues produced and which cell types, bioprinting techniques and materials were utilised for their fabrication.

Table 1.1: Tissue engineering applications using bioprinting technology

Tissue	Cell type	Bioprinting technique	Materials	Reference
Blood vessel	Human umbilical vein endothelial cells Fibroblasts	Extrusion-based	Gelatin methacrylate (GelMA) Pluronic F-127	Kolesky *et al.* (2014)
	QCE6 endothelial cells	Extrusion-based	Pluronic F-127	Jakab *et al.* (2006)
Aortic valve	Smooth muscle cells Aortic valve interstitial cells	Extrusion-based	Alginate/gelatin	Duan *et al.* (2013)
Cartilage	Articular chondrocytes	Jetting-based	Poly(ethylene glycol) dimethacrylate (PEGDMA)	Cui *et al.* (2012)
Bone	Bone marrow stromal cells	Extrusion-based	Agarose	Golez *et al.* (2014)
Adipose	Human mesenchymal stem cells	Extrusion-based	Decellularised extracellular matrix (dECM)	Pati *et al.* (2014)

1.6 Bioink Scaffolds used in Bioprinting

A major challenge for engineering polymer-based 3D tissue scaffolds is finding biocompatible polymers which maintain cell survival and do not prevent cells access to biological materials. Commonly used scaffold biomaterials used for tissue engineering include decellularised extracellular matrix (dECM) (Lu *et al.*, 2013; Pati *et al.*, 2014), ceramics (López-Álvarez *et al.*, 2013), polymers (natural, synthetic or hybrid) (Kohane & Langer, 2008; Gloria *et al.*, 2010) and metals (Alvarez & Nakajima, 2009; Alavi & Kheradvar, 2012). For bioprinting applications, most scaffold design is based on either naturally or synthetically produced polymers which are both compatible with the printing process and provide the desired physical/chemical properties

for the desired construct. Naturally-derived scaffolds commonly include components existing in natural ECM. Synthetic scaffolds, unlike natural polymers, are synthetically produced through chemical processes and are generally more controllable in terms of their chemical/physical characteristics compared to natural scaffolds (Mandrycky *et al.*, 2015). Following printer deposition, biopolymers require suitable crosslinking mechanisms, suitable swelling characteristics and short-term stability for maintaining initial mechanical strength. Biopolymer hydrogels should be gelled or solidified rapidly subsequent to extrusion such that deformation of the printed structure may be avoided (Pati *et al.*, 2015).

1.6.1 Scaffold Elasticity & Mechanotransduction

The mechanical characteristics of soft scaffolds, such as those used for bioprinting applications, are far more challenging to determine when compared to hard scaffolds, due to the fragility possessed by soft scaffolds (Zhu *et al.*, 2011). It has been shown that cells grown in soft scaffolds respond far more significantly to scaffold mechanical properties compared to when cells are grown on hard scaffolds, such as glass or plastics. This is largely due to cells influencing mechanical properties, such as altering scaffold stiffness, hundreds of micrometres away from their cell walls (Winer *et al.*, 2009). Thus, for tissue engineering, a clear understanding of scaffold mechanical properties and the cell responses imposed becomes highly relevant. Techniques for analysing the rheological properties, such as the elastic modulus of scaffold materials, include the use of rheometers or more recently, atomic force microscopy (AFM). A key mechanical property to consider when performing specific scaffold design is scaffold elasticity. Elasticity describes the ability materials have for returning to their original shape after a deforming force or stress has been removed (Wells & Liang, 2011). In viscoelastic materials, the storage modulus (G') describes the elastic properties of the material whereas the loss modulus (G'') describes the viscous properties (Van Den Bulcke *et al.*, 2000). The ratio of stress (force acting on a unit area) to strain (change in shape or size) is called the modulus of elasticity (Young's modulus - longitudinal elasticity) (Wells & Liang, 2011). For the most part, tissue engineers aim to create scaffold materials with near-identical mechanical properties (most importantly scaffold elasticity) as those observed in *in vivo* tissue environments. The elasticity observed in some native tissue environments is highlighted in Table 1.2. Another key consideration for scaffold design is porosity. Scaffolds are required to be porous enough to allow

sufficient space for cell adhesion, ECM generation as well as to allow cell distribution throughout the scaffold such that homogenous tissues may be formed (Chen *et al.*, 2002). Eukaryotic cells explore cellular environments via extension of actin protrusions and formation of integrin adhesions within their respective surroundings (Alberts *et al.*, 2002). It is the combination of both chemical and environmental mechanical signals which induces cellular migration (Nicolas *et al.*, 2004; Chen, 2008). Cells receive mechanical feedback from the substrates they adhere to through a process called mechanotransduction. Mechanotransduction is defined as the conversion of mechanical stimuli to a chemical response (Wang *et al.*, 1993). Substrate elasticity (i.e. Young's Modulus), in particular, has been shown to have a direct effect on cell migration. This process has been termed durotaxis and describes the migration of cells toward mechanically stiff regions. Durotaxis is thought to contribute to development, immune response and cancer metastasis (Harland *et al.*, 2011; Plotnikov *et al.*, 2012). It is therefore of utmost importance to control cell migration and cytoskeletal organisation for engineering physiologically relevant tissues which are able to restore tissue function or act as models for disease. Furthermore, designing scaffold substrates to possess particular stiffness properties may define cell morphologies and therefore have an effect on cell migration and differentiation. Native mesenchymal stem cells, for example, have been shown to commit to lineage specific phenotypes with extreme sensitivity to tissue-level elasticity (Engler *et al.*, 2006).

Table 1.2: Native tissue elasticity

Native Tissue	Young's Modulus (*E*) (kPa)	Reference
Breast (adipose)	19	Krouskop *et al.* (1998)
Prostate	62-69	Krouskop *et al.* (1998)
Liver	10	Muller *et al.* (2009)
Muscle	14-16	Egorov *et al.* (2008)

1.6.2 Decellularised Extracellular Matrix (dECM) Scaffolds

Natural ECM is complex and is composed of a variety of proteins and glycosaminoglycans. Specific cellular functions such as proliferation and differentiation are precisely tuned by the combination of these molecules (Hoshiba *et al.*, 2016). Due to the difficulty in constructing *in vitro* ECM maintaining the same level of complexity and tissue specificity, tissue engineers have looked at using natural dECM as scaffolds for tissue engineering applications. Native tissues and organs are the most common source of dECM for tissue engineering applications (tissue-derived ECM). Cell-derived dECM is an alternative method for obtaining dECM by specifically removing cells from 2D substrates or 3D cell culture scaffolds. The downside to cell-derived dECM lies in the difficulty in obtaining dECM which maintains identical microstructure, protein and glycosaminoglycan composition as well as mechanical properties to that of native *in vivo* ECM. This is due to variances in the cell type(s) and culture conditions (for example different passage numbers). In contrast, if correct decellularisation procedures are carried out on native tissues, the dECM is expected to have identical protein and glycosaminoglycan composition and is expected to possess identical mechanical properties (such as stiffness) to native, *in vivo* tissue ECM (Hoshiba *et al.*, 2016). Decellularisation treatments commonly involve physical, chemical, and biological treatments, as well as combinations thereof, dependant of the dECM to be harvested. Stem cell differentiation may be controlled when culturing cells in native ECM microenvironments. This was demonstrated via the use of bioprinting in Pati *et al.* (2014), where lineage specific chondrogenic and adipogenic differentiation was observed when human adipose-derived stem cells (ASC) were grown in analogues dECM bioinks.

1.6.3 Naturally derived Scaffolds

1.6.3.1 Alginate

Alginate is a brown-algae derived polysaccharide used in several medical applications including drug delivery and cell encapsulation. Alginate is very low in toxicity, inexpensive and is readily available, making it an ideal biomaterial for designing tissue scaffolds (Drury & Mooney, 2003; Van Vlierberghe *et al.*, 2011). When dissolved, alginate forms a concentration-dependant viscous solution. Alginate polymers consist of α-L-guluronic acid (G) and (1-4)-linked β-D-mannuronic acid (M) monomers (Figure 1.4). Gelation of the polymer takes place when divalent

cations (such as Ca^{2+} or Ba^{2+}) interact with G monomers. The G monomers form ionic bridges between different alginate polymer chains (Smidsrød & Skjak-Braek, 1990). Modification of alginate polymers has been achieved in Jia *et al.* (2014), where biodegradable oxidised alginates were used as bioink material for bioprinting. Oxidised alginates may be modified by incorporating cell binding arginine-glycine-aspartic acid (RGD) peptide motifs to enhance integrin binding and cellular attachment. Alginate's ability for structural modification, its cytocompatibility as well as its printability has resulted in alginate being one of the most widely looked upon scaffold materials for bioprinting applications. Additionally, sodium alginate has the ability to conform to virtually any shape or size (Liberski *et al.*, 2016)

1.6.3.2 Agarose

Agarose (Figure 1.4), similar to alginate, is another algal polysaccharide. Unlike alginate however, agarose hydrogels are thermally reversible (Wong & Mooney, 1997). Where gelation occurs at temperatures of around 30°C ± 10°C and lower, gel melting occurs at around 90°C ± 10°C and higher, depending on the experimental procedure employed (Fernández *et al.*, 2007). The structure of the gel is controlled by the agarose concentration (which has a direct effect on the pore sizes of the gel). At low agarose concentrations, the large pore sizes and low mechanical stiffness of the gel allows cells to migrate and proliferate (Lee & Mooney, 2001). Peptides promoting cellular adhesion can be coupled to agarose polysaccharides such that cell adhesion to the gel is maximised (Borkenhagen *et al.*, 1998).

1.6.3.3 Gelatin Methacrylate

Gelatin is inexpensive, denatured collagen which can be derived from a variety of sources (Nichol *et al.*, 2010). Gelatin is a well-established protein-based hydrogel commonly used in in tissue engineering applications due to its availability, low immunogenicity and inherent cell adhesion domains (i.e. cell binding motifs such as arginine-glycine-aspartic acid (RGD) domains) (Dang & Leong, 2006; Melchels *et al.*, 2014). Gelatin polymers may be modified (functionalised at amine-containing side groups) with methacrylate groups, allowing for irreversible cross-linking of methacrylate groups by ultraviolet (UV) irradiation (Figure 1.4 C). Termed gelatin methacrylate (GelMA), GelMA has been largely used as bioink material for bioprinting applications due to its biocompatibility with various cell types, its ability for

controlled solution viscosities as well as the precise control of crosslinking densities (Melchels *et al.*, 2014; Huber *et al.*, 2016).

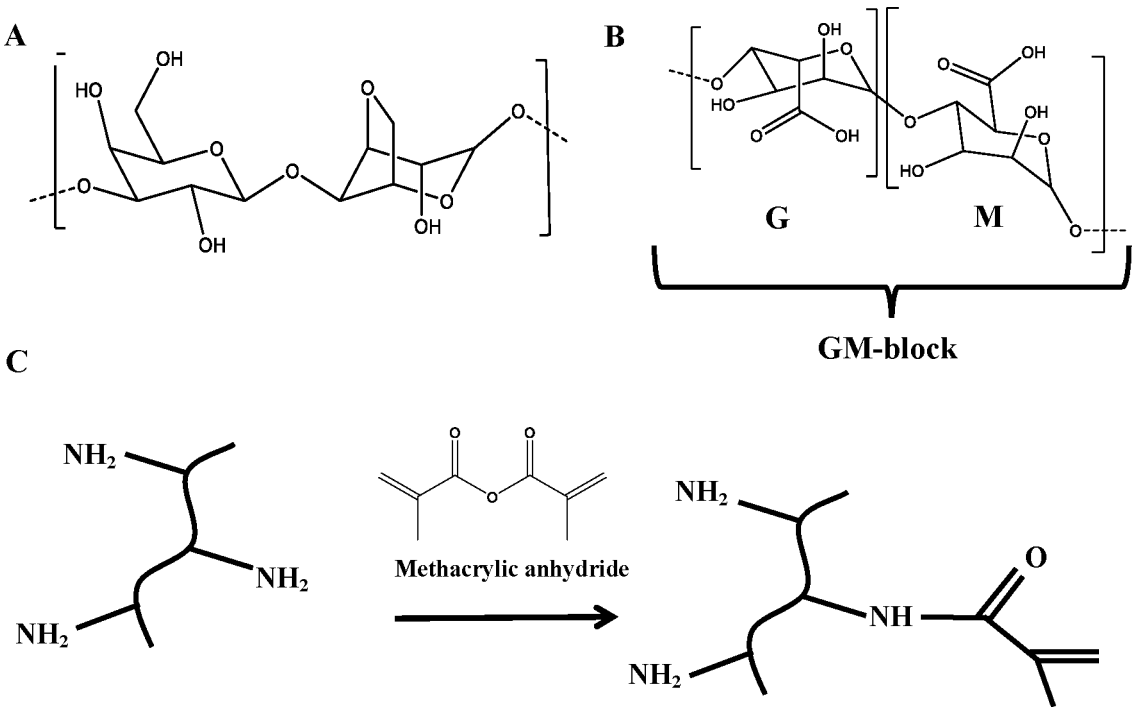

Figure 1.4: Naturally derived hydrogel forming polymers. A: Agarose, B: Alginate. C: Gelatin methacrylate synthesis.

1.6.4 Synthetically Produced Scaffolds

1.6.4.1 Polyethylene Glycol

Synthetically produced polymers include the use of polyethylene glycol (PEG). Experiments using PEG have been on-going for several decades. PEG hydrogels have successfully been used for creating matrices for controlled drug delivery and as scaffolds for regenerative medicine (Lin & Anseth, 2009). PEG has highly versatile macromer chemistry and expresses a high degree of biocompatibility with mammalian cells. Together, this allows for developing numerous specifically designed hydrogels depending on the cell type(s) to be seeded. Versatility in macromer chemistry allows for co-polymerization of PEG polymers with other macromolecules, aiding in engineering cell/tissue specific scaffolds (Lin & Anseth, 2009). Similar to that of

gelatin methacrylate, methacrylate groups may be functionalised to PEG, producing photocrosslinkable PEG methacrylate (Lin-Gibson *et al.*, 2004).

As previously described, scaffolds designed for tissue engineering applications ought to be biodegradable and have architectures which enable cell attachment, proliferation and maintain cell viability (Marga *et al.*, 2012). Following the biodegradation of the scaffold, the goal is for the cells to produce their own functional ECM for structural support and cell-cell signalling. Thousands of studies have shown that the use of natural/synthetic polymers as scaffolds for tissue engineering can be highly feasible for creating simpler, small tissues. However, several limitations and downfalls to scaffold-based tissue engineering have led researchers into creating alternative means for producing complex *in vitro* 3D tissues. The inability to produce fully vascularized thick tissues as well as the lack of precision for engineering tissues comprising of multiple cell types has recently encouraged methods for self-assembly of cellular constructs for the development of 3D tissues (Mironov *et al.*, 2009). Self-assembly by bioprinting typically entails bioink material comprising of small cell spheroids or cylinders containing cell types and ECM components consistent with the tissue to be fabricated (Jakab *et al.*, 2010; Marga *et al.*, 2012).

1.7 Soft-tissue Replacements

Soft-tissue loss from deep burns or tumour resection often requires tissue reconstruction through fat transplantation or alloplastic implants (Sterodimas *et al.*, 2010). Several disadvantages are associated with these approaches such as implant migration as well as rejection of the implant by the recipient. Novel strategies for soft tissue reconstruction or replacement are thus required for treating patients suffering from soft-tissue loss. One approach is engineering functional *in vitro* adipose tissue in high volume. This may one day become the standard for treating patients requiring soft-tissue reconstruction. Stem cells provide key alternatives to the traditional donor-based tissue transplantation strategies due to their ability for self-renewal and their pluripotency. The application of stem cells in regenerative medicine becomes highly valuable when a patient's body rejects donor transplants. Stem cells can be isolated from a patient and grown *in vitro*. Cells can then be induced to differentiate into the somatic cell type(s) required for transplantation. This approach significantly reduces patient immune responses often associated with transplanting

donor tissues (Khatiwala *et al.*, 2012). Adipose tissue, as an example, contains ASC capable of differentiating into mature adipocytes. Adipose-derived stem cells are easily harvested (in contrast to marrow stromal cell extraction) and have the ability to differentiate into cell types of mesodermal, ectodermal and endodermal origin, although they originate from mesodermal lineages (Figure 1.5) (Mizuno, 2012). Treatments for adipose tissue loss mainly focus on using ASC due to their regenerative potential and abundance. Furthermore, their use in preclinical studies as well as in clinical trials has been well documented (Sterodimas *et al.*, 2010; Locke *et al.*, 2011).

1.7.1 Adipose Tissue Engineering

Adipose tissue is commonly referred to as fat tissue and is a highly metabolic, major endocrine organ of the body. It is a highly specialised connective tissue which is found in two forms: white and brown adipose tissue. Both function to cushion and insulate the body but also perform other functions unique to the tissue. Brown adipose tissue functions as the body's primary heat source. Over time, brown adipose tissue is replaced with white adipose tissue which primarily functions as an energy source for the body (Gomillion & Burg, 2006). White adipose tissue is the predominant type of fat in human beings (Kang *et al.*, 2009). Adipose tissue is the major site for the metabolism of sex steroids. It was not until the discovery of leptin (an adipose tissue-derived hormone which functions as a metabolic signal for energy sufficiency) that adipose tissue was considered as an endocrine organ (Kershaw & Flier, 2004). Adipose tissue is a fairly complex vascularised tissue network consisting of cell types including adipocytes, preadipocytes and interstitial cells.

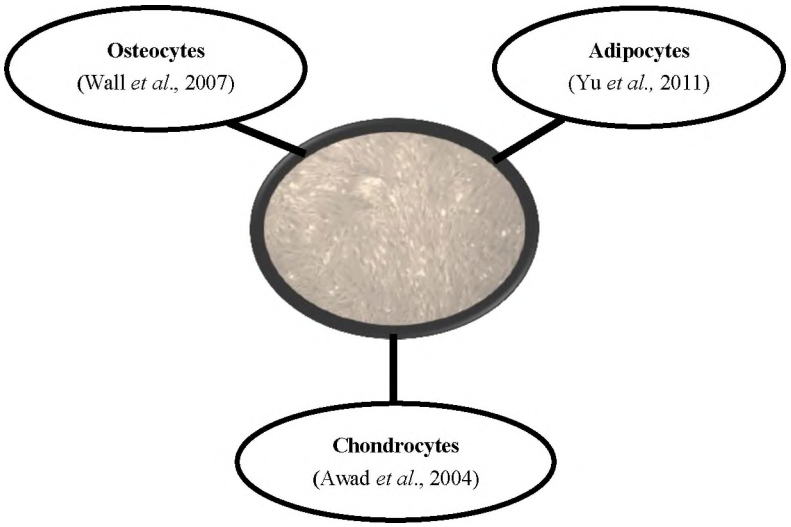

Figure 1.5: Major differentiation lineages of adipose-derived stem cells. Adipose-derived stem cells have the ability for differentiating into lineages of both mesodermal and non-mesodermal origin.

Mesenchymal stem cells (MSC) are of the several stem and precursor cell types present within adipose tissue (Baer and Geiger, 2012). Mesenchymal stem cells were first identified in Friedenstein *et al.* (1966) through their pioneering experiments using rats. Today MSC are most commonly harvested from bone marrow stroma but can also be harvested from umbilical cord blood as well as from adipose tissue (Wei *et al.*, 2013). The potential MSC have for advancing regenerative medicine is largely due to the ability cells have for differentiation into several different lineages of mesodermal origin, including cell types of mesenchymal and non-mesenchymal lineages. Along with being easily harvested (adipose tissue harvesting more so than bone marrow harvesting), easily growing in tissue culture, low immunogenicity and easily adapting to tissue environments, MSC have become key candidates for cellular based therapies (Yarak & Okamoto, 2010). In 2013 it was estimated that MSC were being used in 344 registered clinical trials (in different trial phases) aimed at developing and evaluating MSC-based therapies worldwide (Wei *et al.*, 2013). Mesenchymal stem cells have the capacity to differentiate into cell types such as osteocytes, adipocytes, chondrocytes and myocytes (Hildebrandt *et al.*, 2010). Lineage-specific differentiation can be achieved *in vitro* by treating cells with differentiation-promoting agents and growth factors within their growth medium. Adipogenic differentiation of MSC requires 3-isobutyl-1-methylxanthine (IBMX), dexamethasone, and insulin (Pittenger *et al.*, 1999). Insulin is used to mimic insulin-like growth factor-1 (IGF-1) which results in activation of mitogen-activated protein kinase (MAPK) pathways and clonal expansion (Janderova *et al.*, 2003). The competitive phosphodiesterase inhibitor, IBMX, induces an increase in cyclic adenosine monophosphate (AMP). The increase levels of cyclic AMP subsequently raise the levels of protein kinase A (PKA), which stimulates adipogenesis through transcriptional activation of peroxisome proliferator-activated receptor-gamma (PPARγ) (Scott *et al.*, 2011). Dexamethasone, as well as IBMX, has shown to increase levels of the transcription factors CCAAT/Enhancer Binding Proteins (C/EPB) β and C/EPBδ, both of which are associated with adipogenic differentiation and proliferation (Cao *et al.*, 2007). Cells undergoing adipogenesis form large intercellular lipid vacuoles (droplets). The ECM of adipose tissue is comprised largely of collagen types I, III, IV, V and VI (which is deposited at the cell-ECM border during adipogenic differentiation and functions to support tissue structure) as well as a host of other ECM proteins such as laminin and entactin. Laminin networks associate with collagen type IV such that proper cell attachment and differentiation is achieved. The connection

between laminin and collagen type IV networks is mediated by entactin (Gregoire *et al.*, 1998; Kang *et al.*, 2009). Current *in vitro* adipose tissue models are largely produced through monocultures of differentiated mesenchymal stem cells (bone marrow-derived as well as adipose-derived) as well as embryonic stem cells grown on either synthetic or natural polymer scaffolds (Kang *et al.*, 2009). Recently, however, research groups have significantly increased their interest and efforts into creating functional 3D adipose tissues due to their similarities to native tissues (Table 1.3). A major challenge in *in vitro* adipose tissue engineering is producing tissues with an equally high degree of vasculature present in *in vivo* adipose tissues. Native adipose tissues are generally highly vascularised (Hausman & Richardson, 2004) (Figure 1.6). Studies have shown how the processes of adipogenesis and angiogenesis are not in fact mutually exclusive. A correlation exists whereby a dozen angiogenic factors, among which include leptin, vascular endothelial growth factor (VEGF), fibroblast growth factor 2 (FGF-2) and IGF-1, are secreted by adipocytes in order to maintain vascular homeostasis (Cao, 2007). Vasculature is therefore a requirement for any functional adipose tissue model. Co-culture of endothelial cells with differentiating adipocytes, to create functional 3D adipose tissue, has been demonstrated by Kang *et al.* (2009). The group produced vascularised adipose tissue models through co-culture of human ASC and human umbilical vein endothelial cells (HUVEC) on slow-degrading silk fibroin scaffolds. With estimations indicating that more than half of people living in developed countries are obese or overweight, the use of *in vitro* vascularised adipose tissues which are utilisable as stable disease models may greatly speed up the process of drug discovery and potentially save millions of lives. Moreover, a clearer understanding of disease progression along with improved systematic drug screening techniques may be able to address chronic diseases such as diabetes in the near future.

Table 1.3: Biomaterials used in adipose tissue engineering

Type of Biomaterial	Properties
Collagen/Hyaluronic acid	Composite gel displays enhanced strength and inhibits cell-induced contraction (Davidenko *et al.*, 2010)
Silk fibroin	Low immunogenicity, slow degradation rates and impressive mechanical properties (Mauney *et al.*, 2007; Kang *et al.*, 2009)
Gelatin methacrylate (GelMA)	Photocurable polymer which can be used as a bioink in bioprinting techniques. Construct shape and size can easily be designed for tissue-specific specifications (Huber *et al.*, 2016)
Collagen type I	Collagen type I hydrogels may stimulate the *in vitro* differentiation of preadipocytes (Chun *et al.*, 2006)
Poly(ethylene glycol) (PEG)	PEG hydrogels allow for incorporating various biological molecules to promote cellular proliferation and differentiation (Chiu *et al.*, 2011)
Decellularised extracellular matrix (dECM)	dECM aids in cell-cell connections and 3D organisation which is typical of the complexity of natural ECM. (Pati *et al.*, 2014)

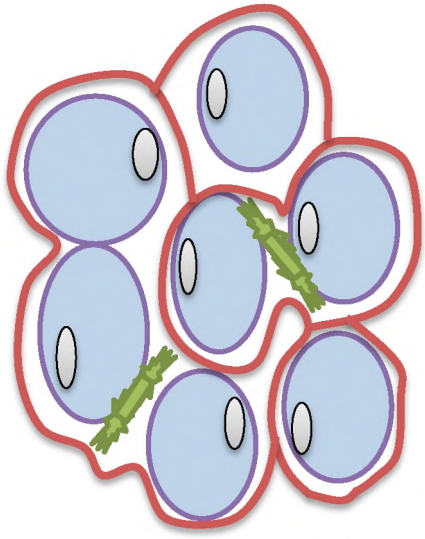

Figure 1.6: Schematic diagram of adipose tissue major cellular constituents. Shown are adipocytes (blue) and adipose-derived stem cells (green) in a vascularised endothelial network (red).

1.8 Problem Statement

The lack of native tissue architectures and cellular interactions experienced when growing cells in 2D monolayer cultures has created a demand for constructing tissue cultures which reduce the gap between native and *ex vivo* tissue physiology. Traditional 2D cell culture methods for analysing cell-based data no longer provide sufficient relevance when compared to 3D tissue cultures. Advances in the fields of regenerative medicine and drug discovery will thus rely heavily on 3D tissues for their use and application. In pharmaceutical industries, engineering disease specific 3D tissue models may greatly reduce the use of animals as models for disease as well as improve the turnover time it takes for drugs entering phase I pharmaceutical trials. Bioprinting is a newly developed technology with the ability to fabricate 3D tissues in a layer by layer manner to ultimately produce a functional tissue. The technology has recently gained attention due to its unique ability to reproducibly produce functional tissues in a spatially defined manner. Although the fabrication of each individual tissue type possesses a unique set of challenges due to the specificity required, bioprinting technology has managed to produce various *in vitro* tissues in laboratory environments. The recent development of this technology has led to very few research groups having access to top of the range bioprinters. The large costs associated with the majority of commercially available bioprinters create a demand for novel strategies for printing 3D tissues. Proposed is an approach to modify conventional fused-filament fabrication technology such that bioprinting may be achieved without the need for purchasing excessively costly equipment. Furthermore, the fabrication of vascularised 3D human adipose tissue will be investigated using sodium alginate hydrogels.

1.9 Hypothesis

It is hypothesised that development of a syringe-housed microextrusion unit, mechanically compatible with a commercially available RepRap Prusa (iteration 3) 3D printer, will allow for the additive three-dimensional layering of bioinks containing adipose-derived human mesenchymal stromal stem cells (ad-HMSC), co-cultured with HUVEC, encapsulated in sodium alginate hydrogel scaffolds.

1.10 Aims & Objectives

The aims of the study were to:

1.10.1 Assemble a commercially available RepRap Prusa i3 3D printer.

Objectives set out were to:

1.10.1.1 Assemble a RepRap Prusa i3 as per manufacturer's instructions.

1) The printer was assembled.
2) The firmware was flashed.
3) The system was calibrated.

1.10.2 Develop syringe-housed microextrusion print-head units.

Objectives set out were to:

1.10.2.1 Modify open source designs for developing syringe-housed microextrusion print-head units.

1) Open-source STereoLithography (STL) designs for syringe-housed microextrusion units were downloaded.
2) Designs were modified using CAD-based software for integration with the RepRap Prusa i3.

1.10.2.2 Assemble microextrusion print-head units

1) Microextrusion print-head units were 3D printed and assembled.
2) Hydrogel printability of microextrusion print-head units was determined.

1.10.3 Validate ad-HMSC differentiation potential

Objectives set out were to:

1.10.3.1 Detect ad-HMSC differentiation using end-point cell staining techniques.

1) Adipogenic differentiation was detected with Oil Red O staining
2) Osteogenic differentiation was detected with Alizarin Red S staining.

1.10.3.2 Monitor ad-HMSC differentiation using Electric Cell-Substrate Impedance sensing (ECIS) technology.

1) Adipogenic and osteogenic differentiation of ad-HMSC was monitored in real-time using the ACEA xCELLigence Real-Time Cell Analyser (RTCA) Single Plate (SP) system.

1.10.4 Formulate sodium alginate hydrogel scaffolds for ad-HMSC and HUVEC encapsulation.

Objectives set out were to:

1.10.4.1 Analyse cell viability of ad-HMSC and HUVEC encapsulated within sodium alginate hydrogels.

1) Live/dead cell staining and confocal microscopy of encapsulated sodium alginate hydrogels was performed.
2) WST-1 cell proliferation assays were performed on encapsulated sodium alginate hydrogels.

1.10.5 Perform 3D printing of sodium alginate hydrogels using the modified RepRap Prusa i3 3D printer.

Objectives set out were to:

10.5.1 Perform 3D printing of co-cultured ad-HMSC/HUVEC sodium alginate bioinks.

1) Printable files (geometries) were created for bioprinting.
2) Cell viability post-printing was analysed by live/dead cell staining and confocal microscopy.

10.5.2 Perform freeform reversible embedding of suspended hydrogels (FRESH) printing of sodium alginate hydrogels.

1) Printable files (geometries) were created for FRESH printing.
2) Cell-free FRESH printing was performed.
3) Biological FRESH printing was performed.

Chapter 2: Assembly of a commercially available RepRap Prusa i3 3D printer

2.1 Introduction

The Replicating Rapid Prototyper (RepRap) project, developed by Dr Adrian Bowyer, was the first project to develop a self-replicating three-dimensional (3D) printing machine. Three-dimensional printing, also referred to as additive manufacturing (AM), is a technique which builds solid objects from a series of layers, whereby each layer is directly printed on top of the previous one (Cummins, 2010). A thorough review of the RepRap project is presented in Jones *et al.* (2010), wherein the often ambiguous terminology associated within the field of self-replicating machines is clarified. RepRap describes a kinematic (physical) self-replicating and self-manufacturing machine which requires human (or other) intervention to reproduce (Jones *et al.*, 2010). Since the inception of the RepRap project, several community portals have been developed, sparking the open-source 3D printing revolution. Largely due to the RepRap projects goal to continuously provide low-cost 3D printing systems, RepRap 3D printers have become the world's most widely-used 3D printing systems within the maker community (*RepRap*, 2016). Although RepRap printers are most commonly designed for thermoplastic-based AM, RepRap systems have been extensively modified for printing a variety of materials. Bioprinting (i.e. the AM of tissues/organs through the use of 3D printing technology; refer to section 1.4) has been achieved through modification of various RepRap 3D printers. Due to the liquid-state of scaffold hydrogel materials commonly used in bioprinting processes, syringe-housed or pump-driven extruders are commonly used for replacing the traditional thermoplastic-based print-heads. Furthermore, thermoplastic Fused Filament Fabrication (FFF) often requires heating plastics (such as acrylonitrile butadiene styrene (ABS) or polylactic acid (PLA)) to temperatures exceeding that of 180 ^{o}C. As mammalian cells are not able to withstand such high temperatures, printing at temperatures allowing for cell survival is a requirement. Hinton *et al.* (2015) describes the 3D printing of biological structures from 3D imaging of whole organs using a RepRap MakerBot (MakerBot Industries) 3D printer fitted with a custom syringe-pump extruder. Similarly, Miller *et al.* (2012) reports the modification of a RepRap MakerBot with a syringe-housed, pneumatically controlled extrusion unit (baricUDA Extruder), which was able to fabricate vascularised solid

tissues from rigid carbohydrate glass filament scaffolds. Further to this, successful bioprinting using a RepRap MendelMax 2.0 3D printer is described in Armstrong *et al.* (2016), whereby a gear-driven paste-extruder is used for replacing the plastic extruder.

Josef Průša (www.prusa3d.com), a developer on the RepRap project, designed his first 3D printer iteration, the Prusa Mendel, in 2010. The aim of the first design was to simplify the existing Mendel design through focusing on shortening the time required to print the 3D printed components (*The story of RepRap Prusa Mendel*, 2014). Shortly after the first development, Průša went about improving his initial design by improving the build simplicity, introducing a belt-driven system attached to stepper motors, as well as including LM8UU linear bearings. This, RepRap Prusa Mendel (iteration 2), 3D printer was released in November 2011 (*Prusa Mendel (Iteration 2)*, 2016). The RepRap Prusa i3 was to follow shortly. The RepRap Prusa i3 was released in 2012 and was a major redesign from previous Prusa versions and other RepRap printers. An aluminium single sheet frame cut was used to replace the triangular threaded rod frame used in previous Prusa models (*Prusa i3*, 2016). This simplified the construction process and allowed far more users the ability to assemble the printer. The RepRap Prusa i3 is an open-source fused deposition modeling 3D printer which has become the most-widely used 3D printer in the world. Largely due to its open frame design, the RepRap Prusa i3 is an ideal 3D printer to modify in order to print a wide range of materials. Furthermore, maintenance of the printer is made a lot easier due to the open functional design (*The story of RepRap Prusa Mendel*, 2016).

The RepRap Prusa i3 kit is available under the RepRap General Public License (GPL). A rendered image of the printer can be found in Figure 2.1. The printer used in this study has a maximum printing size (mm) of: 200 x 200 x 200 and includes two T8 (8 mm) lead screws for improved spatial control about the Z-axis. The following guide explains how to assemble the mechanical components and how to perform the correct electronic wiring for controlling the printer about the X-, Y- and Z-axis. The firmware settings are also described.

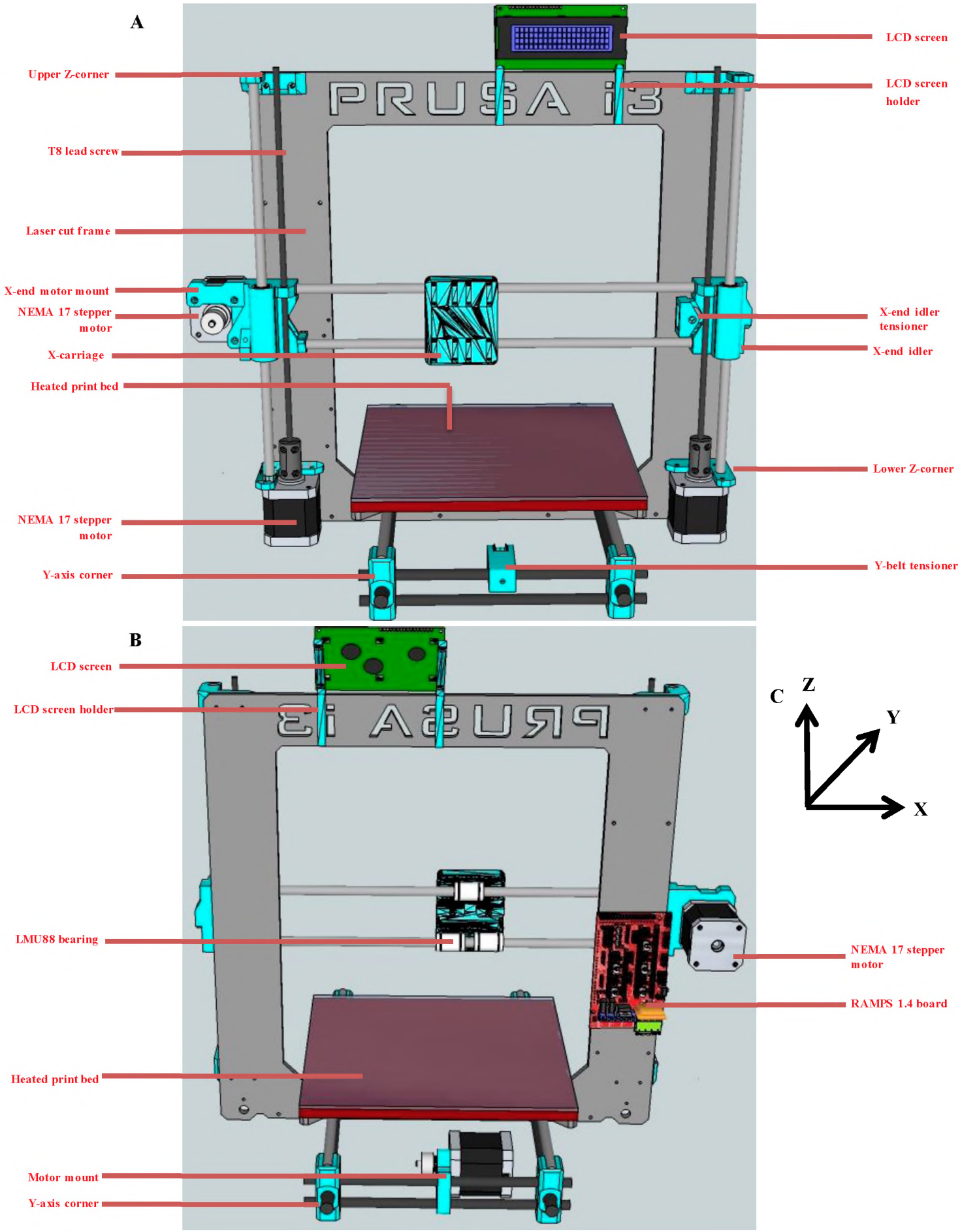

Figure 2.1: RepRap Prusa i3 3D printer. A: Front view. B: Back view. C: Printer Cartesian coordinates. RepRap Prusa i3 SketchUp model was obtained from SketchUp Warehouse (uploaded by Michel M.) under the Trimble SketchUp Make License. Images were rendered in SketchUp Make 2016 (v16.1.1449).

2.2 Methods & Materials

The RepRap Prusa i3 kit was purchased from DIYElectronics (Durban, South Africa). All printed parts provided in the kit were printed in PLA (black). All of the printed parts used were provided within the RepRap Prusa i3 build kit, except for the Y-belt holder and the Liquid Crystal Display (LCD) Smart Controller holders. The standard Y-belt holder provided by DIYElectronics did not provide enough space for inserting the GT2 timing belt. Thus, a modified custom designed Y-belt holder, developed by Nick Sears and available online under a creative commons license (Attribution 3.0 Unported license; Thingiverse #115492; Figure 2.4 A), was 3D printed in polylactic acid (PLA) and used for the assembly of the RepRap Prusa i3. The LCD Smart Controller was mounted to the top of the 6 mm aluminium frame by securing the screen with two PLA-printed LCD Smart Controller holders, developed by Kevin Crossland and available online under a creative commons license (Attribution-ShareAlike 3.0 Unported license; Thingiverse #616987; Figure 2.12 A). Assembly of the printer was done as per suppliers (DIYElectronics) instructions.

2.2.1 Y-Axis Assembly

The Y-axis provided the forward and backward movement of a heated print bed (print surface) and consisted of both vertical and horizontal sides. The Y-axis vertical sides incorporated smooth rods through which the bearing-secured print surface could move. Whereas the horizontal sides functioned to secure a NEMA 17 stepper motor, coupled to a GT2 pulley and timing belt, as well as a printed Y-belt tensioner for controlling the forward and backward movement of the print surface.

Table 2.1: Bill of Materials required for Y-axis vertical side assembly

Printed parts	Non-printed parts
4 x Y-axis corner	2 x M10 (10 mm) x 380 mm threaded rod
	12 x M10 (10 mm) washers
	12 x M10 (10 mm) nuts

Table 2.2: Bill of Materials required for Y-axis horizontal side assembly

Printed parts	Non-printed parts	Electronic components
1 x Y-belt tensioner	4 x M8 (8 mm) x 205 mm threaded rod	1 x NEMA 17 stepper motor (with extended wires)
1 x Bearing guide pair	1 x 623 bearing	
	1 x M4 (4 mm) x 20 mm bolt	
	1 x M3 (3 mm) x 25 mm bolt	
	2 x M3 (3 mm) x 10 mm bolt	
	1 x M4 (4 mm) nut	
	1 x M3 (3 mm) nut	
	2 x M3 (3 mm) washers	
	1 x Aluminium motor mount	
	22 x M8 (8 mm) nuts	
	22 x M8 (8 mm) washers	
	1 x GT2 pulley	
	2 x grub screws	

Table 2.3: Bill of Materials required for Y-bed assembly

Printed parts	Non-printed parts
3 x Linear bearing holder	1 x Laser cut Y-Bed
1 x Y-Belt holder	3 x LM8UU linear bearings
	2 x M8 (8 mm) x 350 mm smooth rods
	6 x M3 (3 mm) x 25 mm screws
	2 x M3 (3 mm) x 10 mm screws

Table 2.4: Bill of Materials required for merging vertical and horizontal frame to Y-bed

Non-printed parts
4 x M8 (8 mm) nut
4 x M8 (8 mm) washer
2 x M8 (8 mm) x 320mm smooth rods
1 x GT2 timing belt

2.2.2 X-Axis Assembly

The X-axis consisted of two parallel smooth rods and a GT2 timing belt which functioned to control the horizontal movement of an extruder carriage. The X-axis was divided into three distinct assemblies which tie in together to merge the entire X-axis. The motor side functioned to mount a NEMA 17 stepper motor, coupled to a GT2 pulley for movement of a GT2 timing belt. The X-axis idler provided tension on the GT2 timing belt for accurate movement of an extruder carriage. An extruder carriage allowed for extruder (i.e. print head) mounting and horizontal movement about the X-axis.

2.2.2.1 Motor Side

Table 2.5: Bill of Materials required for X-axis motor side assembly

Printed parts	Non-printed parts	Electronic components
1 x X-end motor mount	2 x LM8UU linear bearings	1 x NEMA 17 stepper motor (with extended wires)
	2 x M3 (3 mm) x 25 mm screws	
	2 x M3 (3 mm) nuts	
	3 x M3 (3 mm) x 10 mm screws	
	GT2 pulley	
	2 x grub screws	

2.2.2.2 Idler Side

Table 2.6: Bill of Materials required for X-axis idler side assembly

Printed parts	Non-printed parts
1 x X-end idler	1 x 723 bearing
1 x X-end idler tensioner	2 x M3 (3 mm) x 25 mm screws
1x bearing guide pair	1 x M4 (4 mm) x 20 mm screws
	1 x M4 (4 mm) x 25 mm screws
	2 x M3 (3 mm) nut
	2 x M4 (4 mm) nut

2.2.2.3 Extruder Carriage (X-carriage)

Table 2.7: Bill of Materials required for extruder carriage assembly and merging of the X-axis

Printed parts	Non-printed parts
1 x printed X-carriage	3 x LM8UU linear bearings
1 x Y-belt holder	3 x M3 (3 mm) x 25 mm screws
	3 x M3 (3 mm) nuts
	1 x GT2 timing belt
	2 x M8 (8 mm) x 370 mm smooth rods (merging)
	2 x Grub screw
	2 x M5 (5 mm) nuts

2.2.3 Z-Axis Assembly

The RepRap Prusa i3 assembled in this study made use of two T8 lead screws (8 mm diameter) which differs from the standard RepRap Prusa i3, which incorporates threaded rods (3 mm diameter). The T8 lead screws were coupled to NEMA 17 stepper motors and provided improved spatial control of the X-axis about the Z-axis.

Table 2.8: Bill of Materials required for Z-axis assembly

Printed parts	Non-printed parts	Electronic components
2 x printed upper Z-corner pieces	1 x Laser cut Z-axis aluminium frame (6 mm)	2 x NEMA17 stepper motors coupled to T8 (8 mm) lead screw
2 x printed lower Z-corner pieces	3 x M3 (3 mm) x 25 mm screws	
	3 x M3 (3 mm) nuts	
	2 x M8 (8 mm) x 320 mm smooth rods	
	16 x M3 (3 mm) x 10 mm screws	

2.2.4 Heated Print Bed Assembly

The print bed used in the assembly was an MK2b Printed Circuit Board (PCB) heated print bed (120W) with dimensions of: 200 mm x 200 mm. A standard 100K thermistor was taped to the underside of the MK2b heated bed using Kapton tape. Compression springs were incorporated between the aluminium laser cut Y-bed and the MK2b print bed such that sufficient leveling of the print bed could be achieved.

Table 2.9: Bill of Materials required for heated print bed assembly

Non-printed parts	Electronic components
4 x M3 (3 mm) x 20mm screws	1 x MK2b PCB (120W)
1 x glass print bed	1 x 100K thermistor
4 x compression springs	
Kapton tape	

2.2.5 Electronics, Wiring & End-stop Assembly

The assembled RepRap Prusa i3 made use of an Arduino Mega 2560 microcontroller board for connecting to a computer with a Universal Serial Bus (USB) cable. A RepRap Arduino Mega Pololu Shield (RAMPS) 1.4 board was pinned on top of the Arduino Mega 2560 to connect the electronics needed for the printer. The RAMPS 1.4 board included plug in stepper drivers as well as extruder control electronics. The RepRap Prusa i3 included three mechanical switch endstops for referencing the home positions of the Cartesian axes.

Table 2.10: Bill of Materials required for electronic wiring & end-stop assembly

Non-printed parts	Electronic components
3 x M3 (3 mm) x 20 mm screws or cable ties	Arduino Mega 2560 board
	RAMPS 1.4 board
	Mechanical switch X-endstop
	Mechanical switch Y-endstop
	Mechanical switch Z-endstop
	Modular 12V DC power supply (400W)

2.2.6 Liquid Crystal Display (LCD) Smart Controller

The RepRap Prusa i3 included a LCD Smart Controller for monitoring printing status (progress), thermal settings (heated print bed and extruder), as well as extruder coordinates (i.e. extruder position). The Smart Controller contained a Secure Digital (SD) card reader, a rotary encoder and a 20 Character x 4 Line LCD display. The LCD Smart Controller was connected to the RAMPS 1.4 board via the LCD smart adapter.

Table 2.11: Bill of Materials required for liquid crystal display (LCD) screen assembly

Printed parts	Non-printed parts	Electronic components
2 x LCD Smart Controller holder	4 x M3 (3 mm) x 10 mm screws	LCD Smart Controller
	4 x M3 (3 mm) nuts	LCD smart adapter

2.3 Results

2.3.1 Y-Axis Assembly

The print bed (print surface) of the RepRap Prusa i3 was mounted to the Y-axis. The Y-axis controlled the forward and backward movement of the print bed via the Y-axis belt. Movement of the Y-bed was achieved using a GT2 pulley and GT2 timing belt, driven by a NEMA 17 stepper motor.

2.3.1.1 Vertical Sides

1) An M10 nut, two M10 washers and another M10 nut was placed roughly 6 cm from the end of each 380 mm threaded rod.
2) Both threaded rods were fixed to the printed Y-axis corners (Figure 2.2 A) with an M10 nut and M10 washer on either side of the printed Y-corners (Figure 2.2 B).

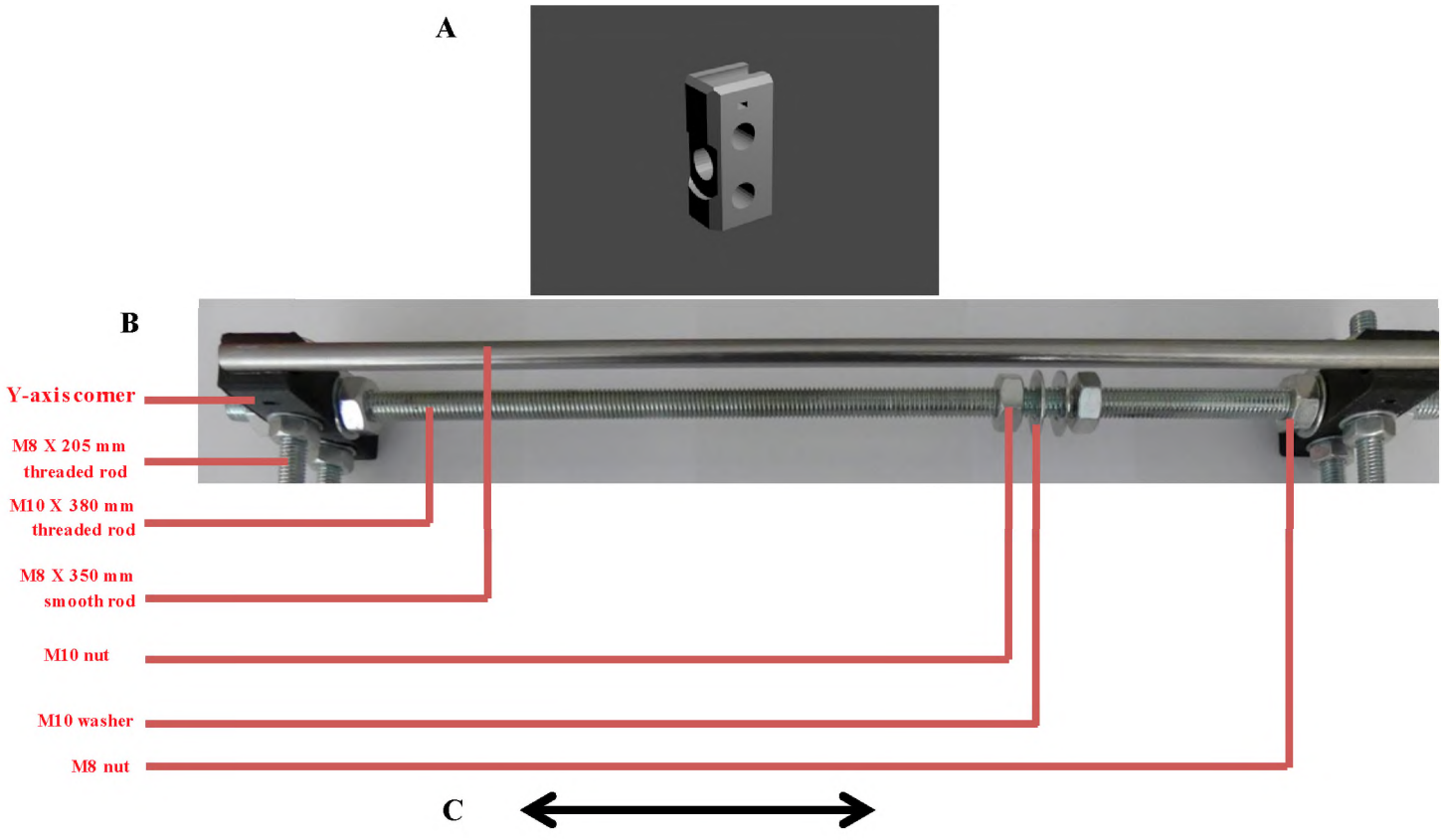

Figure 2.2: Y-axis vertical side. A: Printed Y-axis corner. B: Fixed threaded rod. C: Direction of motion.

2.3.1.2 Horizontal Sides

1) The first part which was assembled was the Y-belt tensioner. A 623 bearing was inserted between both printed bearing guide parts. The printed bearing guide parts were fixed by gently squeezing the parts together (Figure 2.3 A).
2) The bearing guide was inserted into the printed Y-axis tensioner (Figure 2.3 B). The guide was fixed to the tensioner using an M3 x 25 mm bolt, two M3 washers and an M3 nut (Figure 2.3 C).
3) A captive M4 nut was inserted into the nut trap within the Y-axis tensioner, followed by an M4 x 20 mm tensioning bolt.
4) Two of the M8 x 205 mm threaded rods were slid through the aluminium Y-motor mount and one through the previously assembled Y-belt tensioner.
5) The tensioner and motor mount were fixed to the M8 x 205 mm threaded rods using M8 washers and M8 nuts on either side of both pieces.
6) The GT2 pulley was fixed to the NEMA 17 stepper motor by tightening with the two grub screws.
7) The NEMA 17 stepper motor was fixed to the motor mount using two M3 x 10 mm bolts.
8) An M8 nut and M8 washer was inserted on either ends of all four threaded rods.

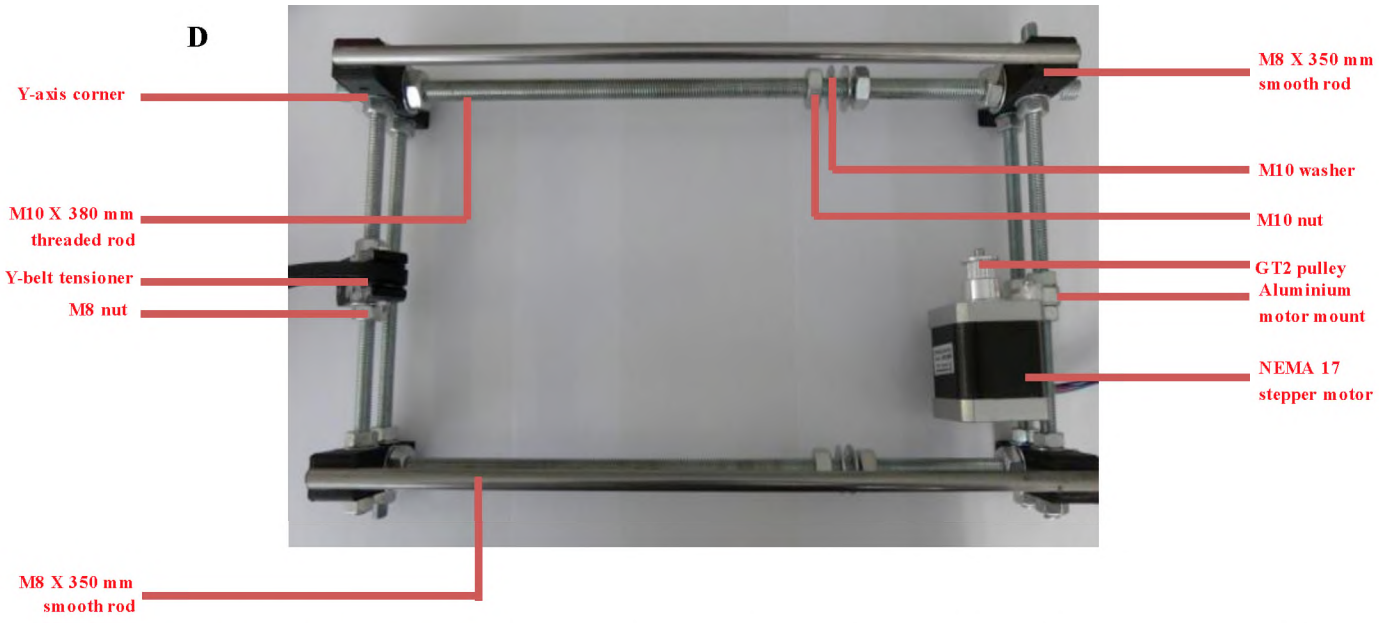

Figure 2.3: Y-axis vertical and horizontal side. A: Printed 623 bearing guide pair. B: Printed Y-belt tensioner. C: Assembled Y-axis tensioner. D: Assembled Y-axis frame.

2.3.1.3 Y-bed

1) The printed Y-belt holder (Figure 2.4 A) was fixed to the center of the Y-bed using two M3 x 10 mm screws (orientation did not matter).
2) The LM8UU bearings were inserted into the printed bearing holders and subsequently slid onto the M8 x 320 mm smooth rods. Two bearings were used per smooth rod.
3) The bearing holders were secured to the bed using two M3 x 25 mm screws per holder. The bolts were screwed directly into the tapped holes in the print bed.

2.3.1.4 Merging Vertical, Horizontal & Y-bed

1) The short horizontal threaded assemblies were screwed into the long vertical side Y-axis corner pieces using an M8 nut and M8 washer.
2) The ends of the M8 x 320 mm smooth rods were snapped down into the top of the Y-corner pieces, securing the rods to the Y-corners.

2.3.1.5 Y-Axis Belt

1) A GT2 belt was installed by threading the belt through the belt pulley and idler. The belt was fixed to the printed Y-belt belt holder using a flathead screwdriver to push the belt in firmly (Figure 2.4 B).
2) After the belt was inserted, a cable tie was used to secure the belt to itself.

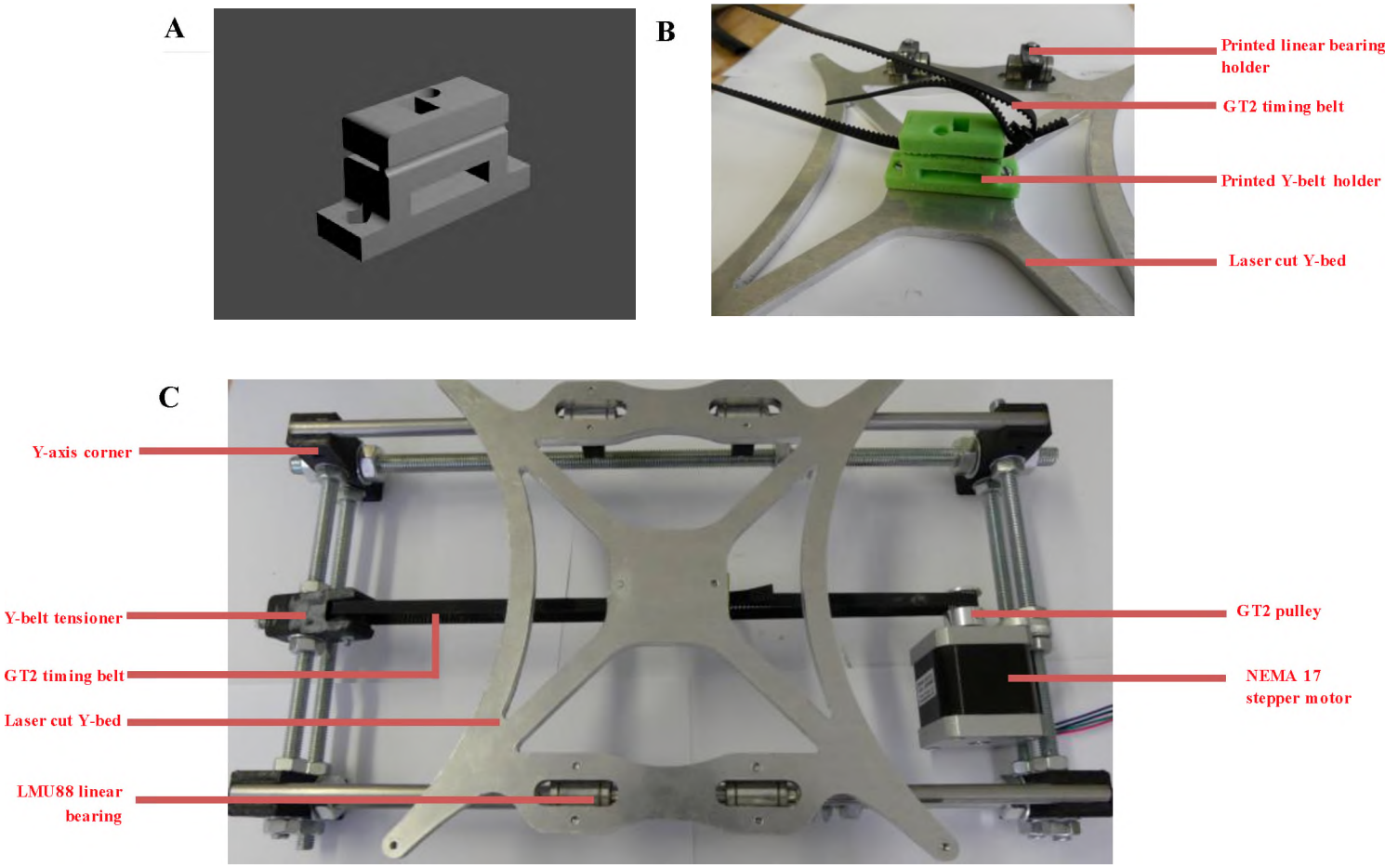

Figure 2.4: Merging vertical and horizontal frame to Y-bed A: Printed Y-belt holder. B: Y-axis belt fixed to printed belt holder. C: Fully assembled Y-axis

2.3.2 X-Axis Assembly

The X-axis functioned to facilitate mounting and movement of an extruder (mounted to an extruder carriage) to the left or to the right. Movement of the extruder carriage was achieved using a GT2 pulley and GT2 timing belt, driven by a NEMA 17 stepper motor.

2.3.2.1 Motor Side

1) Two LM8UU linear bearings were slid into the vertical positions of the printed X-end motor mount (Figure 2.5 A). Bearings were secured using two M3 x 25 mm bolts and M3 nuts.
2) A GT2 pulley was fixed to the NEMA 17 stepper motor and tightened with the two grub screws.
3) The NEMA17 stepper motor was fixed to the X-end motor mount using three M3 x 10 mm screws (Figure 2.5 A).

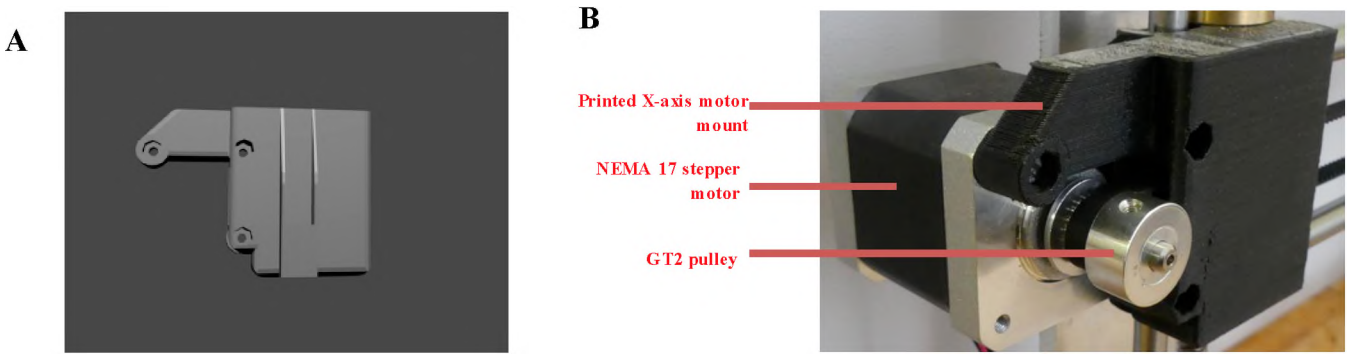

Figure 2.5: X-end motor mount. A: Printed X-end motor mount. B: Assembled X-end motor mount.

2.3.2.2 Idler Side

1) The X-end idler tensioner (Figure 2.6 A) was assembled the same way as described for the Y-belt tensioner (2.2.1.2). A 623 bearing was clamped between a printed 623 bearing guide pair (Figure 2.6 B).
2) The tensioner was positioned within the printed X-end idler (Figure 2.6 C) and secured using a M4 x 25 mm screw.
3) Two LM8UU linear bearings were slid into the X-end idler and secured using two M3 x 25 mm bolts and M3nuts.

Figure 2.6: Printed idler side A: Printed X-end idler tensioner. B: Printed 623 bearing guide pair. C: Printed X-end idler

2.3.2.3 Extruder Carriage (X-carriage)

The extruder carriage was used for screw-mounting an extruder to the X-axis of the RepRap Prusa i3

1) Three LM8UU linear bearings were horizontally inserted into the printed X-carriage (Figure 2.7 A). The bearings were secured to the X-carriage using three M3 x 25 mm bolts and M3 nuts.

2.3.2.4 X-Axis Merging

1) Two M8 x 370 mm smooth rods were pushed into the X-end motor mount side holes.
2) The X-carriage (extruder carriage) was pushed onto the smooth rods (Figure 2.7 B).
3) The X-end idler was pushed into the other end of the smooth rods, ensuring that the orientation of the idler was correct.

2.3.2.5 X-axis Belt & Pulley

1) A GT2 pulley was secured to a NEMA17 stepper motor using two grub screws.
2) A GT2 timing belt was secured to the printed X-carriage in the same way as was done in 2.2.1.5.
3) The GT2 timing belt was fed around the GT2 pulley as well as the X-end tensioner.
4) After the belt was inserted, cable ties were used to secure the belt to itself.

2.3.3 Z-Axis Assembly

Upward and downward movement of the X-axis was controlled by the Z-axis. An aluminium frame, along with two lead screws, made up the bulk of the RepRap Prusa i3 Z-axis.

1) Two printed lower Z-corner pieces were screwed onto the laser cut aluminium frame (6 mm) using three M3 x 10 mm screws per piece.
2) Both NEMA17 stepper motors coupled to T8 lead screws were screwed into each of the lower Z-corner pieces.
3) Two M8 x 320 mm smooth rods were placed longitudinally against the frame, through the holes on the lower Z-corner pieces.
4) The fully assembled X-axis was slid down through the M8 x 320 mm smooth rods, into the T8 lead screws (Figure 2.7 C).
5) The top of the M8 x 320 mm smooth rods were inserted through the printed upper Z-corner pieces.
6) The upper Z-corner pieces were screwed onto the aluminium frame using three M3 x 10 mm screws per piece.

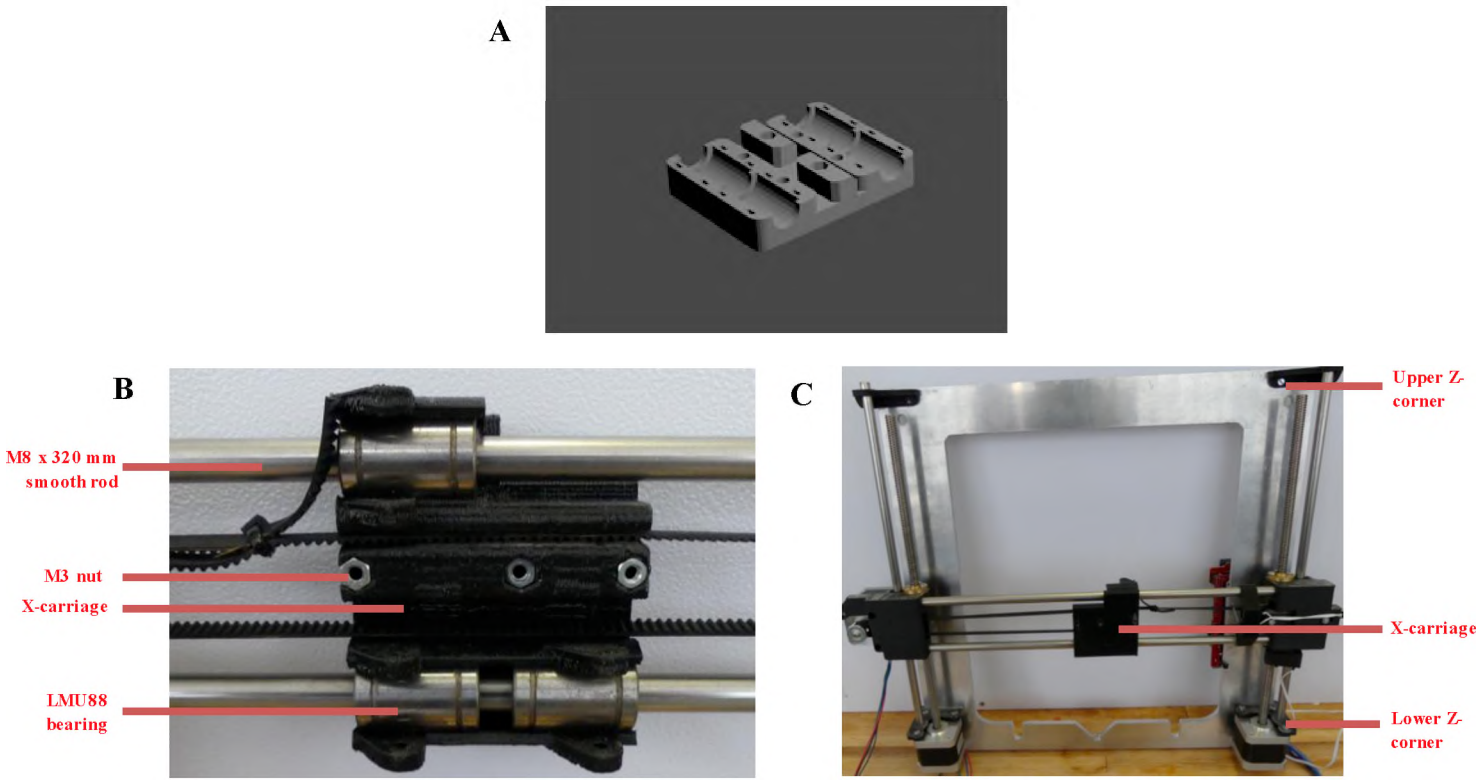

Figure 2.7: XZ-frame. A: Printed X-carriage. B: Assembled X-carriage. C: Fully assembled XZ frame.

2.3.4 Merging Y-Axis to XZ-frame

1) The distance from the Y-axis corner to the rear of the vertical Y-axis M10 nut was measured, ensuring that either side of the vertical Y-axis frame nuts was equal in distance to the horizontal side of the Y-axis (i.e. ensuring the XZ frame is perpendicular to the Y-axis).
2) The Z-axis aluminium frame was placed between the two M10 washers on each bottom threaded rod of the Y-axis frame (Figure 2.3).
3) The M10 nuts on either side of the frame were tightened.

2.3.5 Heated Print Bed Assembly

The heated print bed allowed for heating of the print surface to a desired temperature.

1) A 100K thermistor was secured to the MK2B heated bed (120W) using a small piece of kapton tape (Figure 2.8 A).
2) The heated print bed was secured to the Y-bed using four M3 x 20 mm screws. Compression springs were inserted through the screws, between the heated print bed and the Y-bed (Figure 2.8 B).
3) The print bed was leveled by tightening or loosening individual screws.

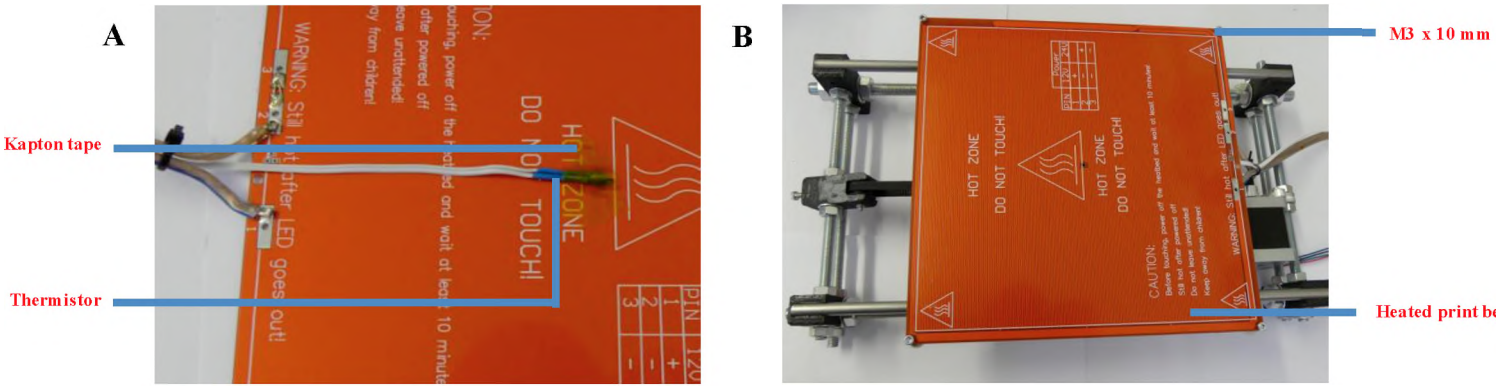

Figure 2.8: Heated print bed assembly. A: Print bed thermistor. B: Mounted heated print bed.

2.3.6 Electronics, Wiring & End-stop Assembly

The printer power, heated print bed thermistor, stepper motors, mechanical end-stops, Liquid Crystal Display (LCD) and extruder were connected to a RAMPS 1.4 board, pinned to an Arduino MEGA 2560 board, for controlling, monitoring and providing power to the various printer components.

1) A RAMPS 1.4 board (Figure 2.9 A) was pinned to an Arduino MEGA 2560 board (Figure 2.10) (RAMPS board on top of Arduino).
2) Using cable ties, the Arduino/RAMPS board was mounted to the rear end of the aluminium frame using the screw holes provided on the frame.
3) Heated print bed power cables were plugged into the D10 switches on the RAMPS 1.4 board (Figure 12.9 B).
4) A modular 12V DC power supply (400W) was plugged into connector plug on the RAMPS 1.4 board (Figure 2.9 B)
5) The heated print bed thermistor was plugged into the T0 pin on the RAMPS 1.4 board (Figure 2.9 C).
6) The X-axis stepper motor was plugged in the X-pin, the Y-axis stepper motor in the Y-pin and both Z-axis stepper motors in the Z-pins (order did not matter) on the RAMPS 1.4 board. Orientation of the stepper motor cables was very important (negative end was facing away from the power inlets and the positive end was facing toward the power inlets) (Figure 2.9 D).
7) A mechanical Z-endstop was attached to the M8 x 320 mm smooth rod on the right hand side of the Z-axis (near the bottom of the rod) (Figure 2.11 A).
8) A mechanical Y-endstop was attached to the rear horizontal end of the Y-axis (Figure 2.11 B).
9) A mechanical X-endstop was attached to the tensioner side of the X-axis (Figure 2.11 C).

10) Mechanical switch endstop connectors were plugged into the RAMPS 1.4 board on the left most pins (Figure 2.10 A.). The orientation of the connectors did not matter.

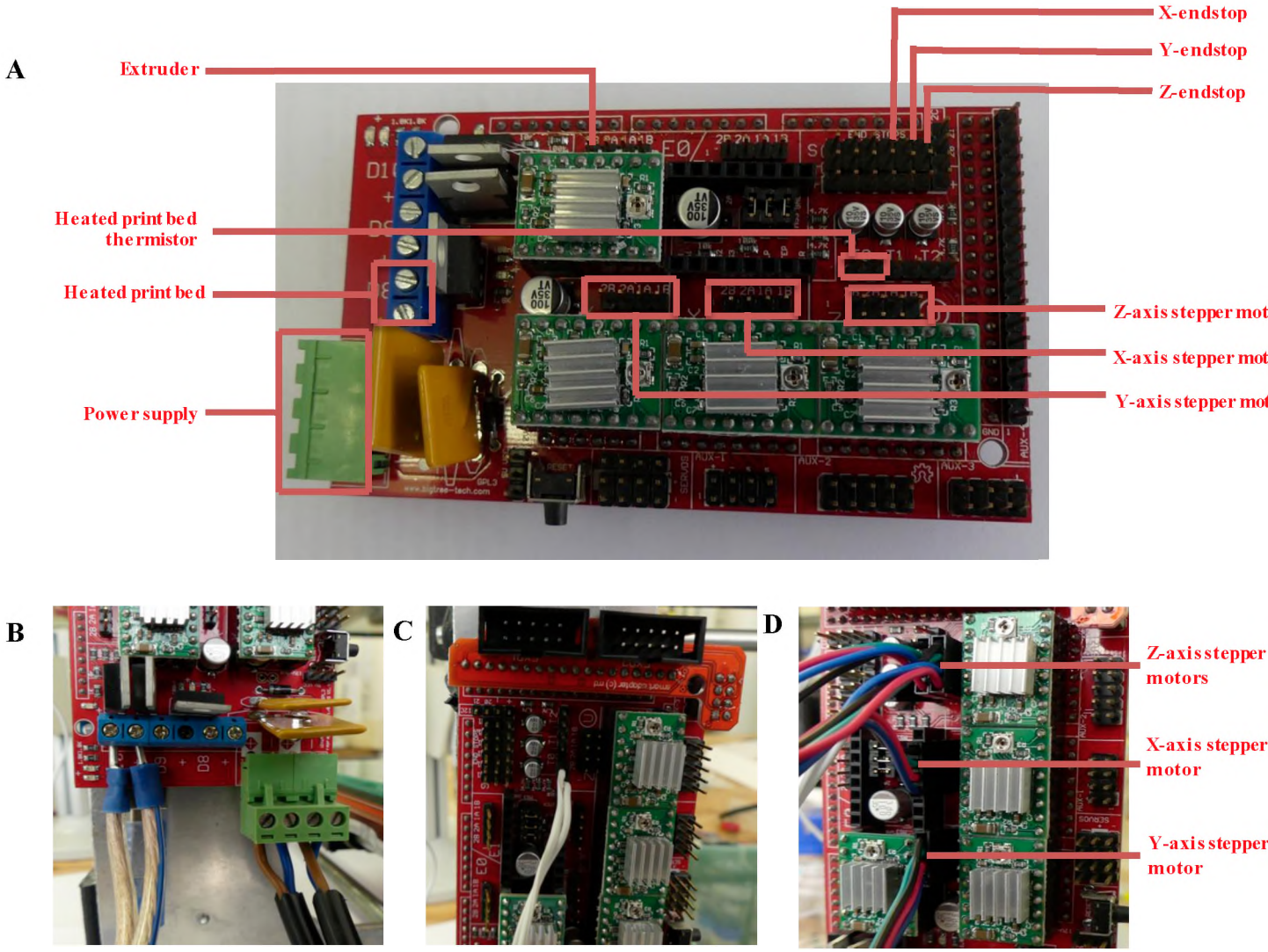

Figure 2.9: RAMPS 1.4 wiring. A: Schematic of RAMPS 1.4 board wiring. B: Power supply and heated print bed wiring. C: Thermistor wiring. D: Stepper motor wiring

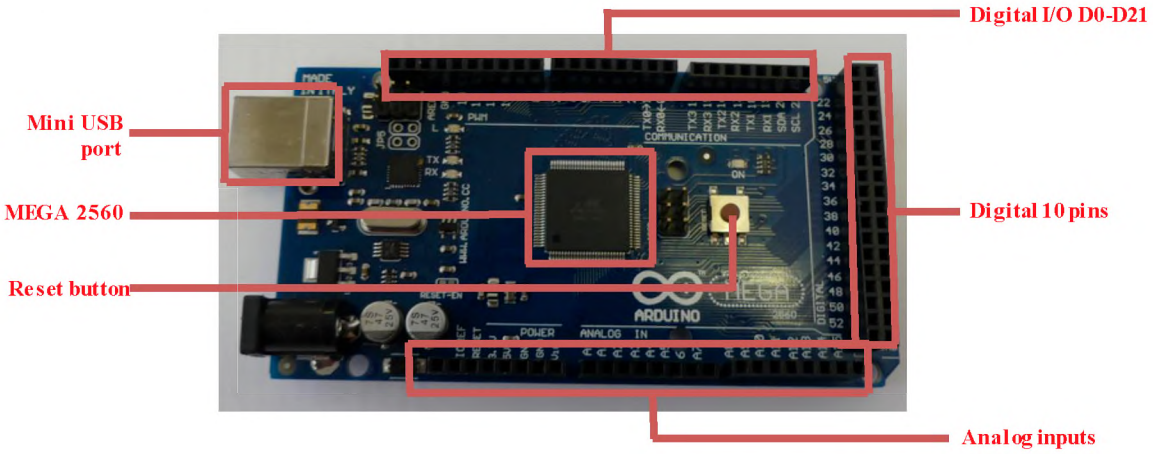

Figure 2.10: Schematic of Arduino MEGA 2560 board.

A

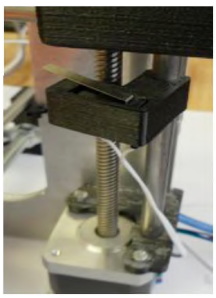

B

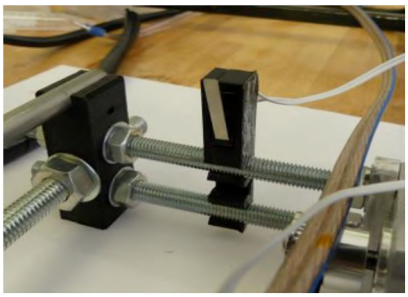

C

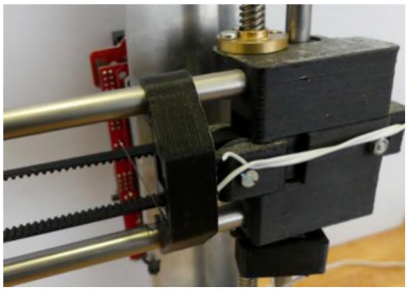

Figure 2.11: Mechanical switch endstop positions. A: Z-endstop. B: Y-endstop. C: X-endstop.

2.3.7 Liquid Crystal Display (LCD) Smart Controller

The LCD Smart Controller was mounted to the top of the 6 mm aluminium frame (via two printed LCD Smart Controller holders) and allowed for monitoring print progress and printer status (temperatures and extruder position). Furthermore, axes movements could be controlled with the rotary encoder on the Smart Controller. The LCD Smart Controller contained a SD card port to allow for directly printing files without the need for a computer connection.

1) Two LCD Smart Controller holders were 3D printed in red PLA (Figure 2.12 A)
2) An LCD smart adapter was plugged in to the top of the RAMPS 1.4 board (Figure 2.12 B).
3) The EXP1 port on the LCD was pinned to the EXP1 port on the LCD smart adapter. The same was done for the EXP2 ports.
4) The LCD Smart Controller was mounted to the top of the aluminium frame by securing the screen to the printed screen holders using four M3 x 10 mm screws and nuts (Figure2.12 C).

A

B

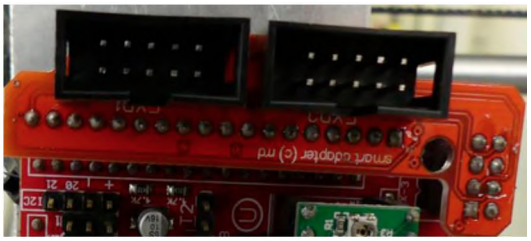

C

Figure 2.12: Liquid Crystal Display (LCD) screen. A: Printed LCD screen holder. B: LCD screen adapter. C: Mounted LCD screen.

2.3.8 Firmware

An Arduino board (Figure 2.10) is an integrate micro-computer and requires installing software (firmware) specifically written for controlling and monitoring the RepRap Prusa i3. Open-source Marlin firmware was used for installing (i.e. flashing) the Arduino MEGA board.

2.3.8.1 Arduino flashing

1) The RAMPS/Arduino board was connected to a PC using a USB cable.
2) Firmware installation was done through the Arduino desktop software environment. The Arduino software environment can be downloaded from: http://arduino.cc/en/Main/Software. The firmware used for flashing the Arduino board is called Marlin and can be downloaded from: https://github.com/MarlinFirmware/Marlin.
3) In the Arduino environment, the marlin.ino file was opened.
4) In the Arduino environment, Tools > Board > Arduino MEGA 2560 was selected.
5) In the Arduino environment, "Upload to flash" was clicked to flash the RAMPS/Arduino board.
6) In the Arduino environment, the Configuration.h tab was where most user editable settings were configured for programming the Arduino board and running the printer.

2.3.8.1.1 Basic settings

1) Baud rate: Defined the speed of the serial link. The baud rate was set to "115200".
2) Motherboard: Defined the electronics being used. "33" was selected for RAMPS 1.4 board.
3) Extruders: Defined the amount of print heads. This was set to "1".

2.3.8.1.2 Thermal settings

1) "TEMP_SENSOR_0" was set to "0", as no extruder thermistor was used.
2) "TEMP_SENSOR_BED" was set to "1", as a 100k thermistor was used for the heated print bed.
3) "EXTRUDER_MINTEMP" was set to "0", as no extruder thermistor was used.

2.3.8.1.3 Mechanical settings

1) Endstop "INVERTING" was set to "false" for all three the X,Y and Z endstops.
2) "HOME_DIR" was set to "-1" to set the endstops in their minimum position.
3) "MIN_POS" was set to "0" and "MAX_POS" was set to "200" to define the printer limits.

2.3.8.1.4 Movement settings

1) "NUM_AXIS" was set to "4" such that all of the X, Y and Z-axis, as well as an extruder motor could be controlled.
2) "HOMING_FEEDRATE" was set to "(50*60. 50*60, 4*60, 0)" for the X, Y, Z, E-axis, respectively. This defined the speed (mm/min) the printer traveled to its home position.
3) "DEFAULT_AXIS_STEPS_PER_UNIT" was set to "(80,80,4000,465)".
4) "DEFAULT_MAX_ACCELERATION" was set to "(3000,3000,75,2000)".
5) "DEFAULT_RETRACT ACCELLERATION" was changed to "1000".
6) "DEFAULT_ACCELERATION" was changed to "1000".
7) JERCK settings were:
8) "XY 15.0" mm/s
9) "Z 0" mm/s
10) "E 7.0" mm/s
11) PLA/ABS preheat settings could be changed in the configuration.h file, or the preheat values could be assigned through controller programs such as Pronterface or Repitier host.
12) To activate the LCD screen, the line "//#define REPRAP_DISCOUNT_SMART_CONTROLLER" was changed to "#define REPRAP_DISCOUNT_SMART_CONTROLLER" in the Marlin configuration.h file.

2.3.9 Printer Control & Slicing Software

Pronterface (printrun-20150310) host interface software was used for controlling the printer X-, Y- & Z- movements, as well as the extruder motor. The software can be downloaded from: https://github.com/kliment/Printrun/releases/tag/printrun-20150310.

Default Pronterface settings were used at 250 000 baud rate. Print configurations were made using Cura Software (v15.04.4).

Preparing STereoLithography (STL) files for 3D printing (i.e. slicing) was achieved using Cura Software. Cura software can be downloaded from: https://ultimaker.com/en/products/cura-software. The standard configurations made in Cura are tabulated in Table 2.13.

Table 2.12: Standard Cura configurations used for printing

Quality	**Fill**	**Speed and Temperature**	**Support**	**Filament**	**Machine**
Layer height: 1 mm	Fill density: 0 %	Print speed: 2 mm/s	Support type: None	Diameter: 0.5 mm	Nozzle size: 0.5 mm
Shell thickness: 0.5 mm		Print/Bed temperature: 0 °C	Platform adhesion type: None	Flow: 5 %	
Retraction: enabled					

2.4 Troubleshooting & Discussion

Assembly of the RepRap Prusa i3, as well as flashing of the firmware (Marlin), was done in accordance to the build guide provided by DIYElectronics, South Africa. Overall, the system was assembled with practically no issues.

Assembly of the RepRap Prusa i3 initially included a thermoplastic Greg's Wade extruder (Supplementary Material, Figure S1). The extruder was used for testing the printability of the printer using PLA filament. Testing the thermoplastic printability of the RepRap Prusa i3 required changing thermistor firmware settings in the malin.ino configuration file. Where the line "TEMP_SENSOR_0" was set to "0", changing the value to "1" (for a 100K thermistor) enabled detection (monitoring) of the extruder temperature. Furthermore, the Greg's Wade extruder power cable could be plugged directly into the extruder port (E0) on the RAMPS 1.4 board (Figure 2.9 A) with no changes required in the firmware. Calibration of the stepper motor steps was done using a stepper motor calculator available on the Prusa website (http://www.prusaprinters.org/calculator/). For the X and Y motors, motor step angle was set to 0.9', driver micro-stepping was set to 1/8, belt pitch was set to 2 mm (for the GT2 timing belt) and pulley tooth count was set to 20 (for the aluminium GT2 pulleys). These values generated a result of 80 steps per mm which was assigned to the line: "DEFAULT_AXIS_STEPS_PER_UNIT" (X,Y) in the malin.ino configuration file, within the Arduino desktop environment. For the T8 lead-screw driven Z-axis, motor step angle was set to 1.8^{o} (200 per revolution), driver micro stepping was set to 1/16, lead screw pitch was set to 0.8 mm per revolution and pitch presets was set to M8 (metric, 1.25 mm per rotation). Gear ratio was set to 1:1. These values generated a result of 4000 which was also assigned to the line: "DEFAULT_AXIS_STEPS_PER_UNIT" (Z) in the malin.ino configuration file. Extruder motor steps calibration was manually determined for printing PLA using the following equation:

$$\boldsymbol{New\ Esteps = Old\ Esteps\ x\ \frac{100}{Distance\ travelled\ (mm)}}$$

Equation 2.1: Extruder motor steps (*Esteps*) calibration based on distance of filament extrusion.

The amount (distance) of filament extruded when assigning the printer to extrude 1 mm of PLA was measured. The value obtained was used in Equation 2.1 to determine the extruder

motor steps per mm. A value of 465 was obtained and assigned to the line "DEFAULT_AXIS_STEPS_PER_UNIT" (E) in the malin.ino configuration file.

The plastic-based printability of the entire system was tested using PLA. The STereoLithography (STL) file of a video game key ring was downloaded online under a creative commons license (Attribution-ShareAlike 3.0 Unported; Thingiverse #197209). The STL was sliced in Cura and the Gcode opened with Pronterface software. The RepRap Prusa i3 was able to successfully print the construct in PLA (Supplementary Material, Figure S2).

To conclude, the RepRap Prusa i3 assembly and Arduino firmware flashing proved successful. Modification of the printer, by replacing of the Greg's Wade thermoplastic-based print-head, could therefore be carried out.

Chapter 3: Modification of a RepRap Prusa i3 3D printer for syringe-based extrusion

3.1 Introduction

Bioprinting is defined as the automated computer-aided design (CAD) deposition of living cells, extracellular matrix (ECM) components and biochemical factors at a specific position for the development of 3D tissues (Pati *et al.*, 2015). The main technologies used in bioprinting are inkjet (Campbell *et al.*, 2007; Cui *et al.*, 2009), microextrusion (Pati *et al.*, 2015; Ozbolat & Hospdiuk, 2016) and laser-assisted bioprinting (Barron *et al.*, 2004). Different features of each technology should be considered in light of the requirements for bioprinting. Surface resolution, cell viability and selection of appropriate biological material all factor in to which bioprinting technology should be selected.

The present study aims to achieve low-cost bioprinting through modification of a RepRap Prusa i3 3D printer with syringe-housed microextrusion print-head units. Extrusion-based bioprinting relies on dispensing polymer or hydrogel material through a micro nozzle and positioning them through computer-controlled motion either of the printing heads or the collecting stage. Hydrogels are generally loaded in either metallic or plastic syringes and are dispensed via pneumatic or mechanical (piston-driven or screw-driven) force on a building platform (Pati *et al.*, 2015). Due to the delay in compressed gas volume associated with pneumatic-driven printing systems, mechanical dispensing systems may provide more direct control of material flow. Furthermore, screw-driven systems may provide more spatial control and allow for dispensing hydrogels of high viscosities (Murphy & Atala, 2014). Several commercially available extrusion-based bioprinters have been used for fabricating a variety of 3D tissues. The pneumatically-driven 3D Bio-plotter dispensing system, designed by EnvisionTec, has been used for bone tissue engineering (Pei *et al.*, 2016; Wang *et al.*, 2016). Mechanical microextrusion using the NovoGen MMX bioprinter, designed by Organovo, has successfully been used for bone (Golez *et al.*, 2014), liver (Bertassoni *et al.*, 2014) and breast cancer (King *et al.*, 2013) tissue engineering.

Large amounts of research outputs have been done using commercially available bioprinting systems. Due to the large costs associated with high-end commercially available bioprinters. Low-cost bioprinting via modification of RepRap systems have been investigated. Hinton *et al.* (2015) reports the modification of a RepRap MakerBot Replicator (MakerBot Industries) 3D printer by fitting a custom syringe-pump extruder in place of the thermoplastic-based print-head. Similarly, Armstrong *et al.* (2016) reports the modification of a RepRap MendelMax 2.0 (Maker's Tool Works, USA) 3D printer by fitting a gear-driven paste extruder in place of the thermoplastic-based print-head.

The following chapter describes the modification of RepRap Mendel Prusa i3 with two distinct 3D printed syringe-based extruder units. A simplified screw-driven syringe extruder, designed by Almus Yang and available online under a creative commons license (Attribution-NonCommercial 3.0 Unported; Thingiverse #536373), was modified based on designs commonly used for 3D printing of hydrogels. The extruder's printed parts were designed to be mounted to a standard NEMA 17 stepper motor and to house an insulin syringe (1 mL). Furthermore, the printed syringe holder was designed to fit to the standard X-carriage of a RepRap Prusa i3 such that the traditional thermoplastic-based extruder may simply be removed and replaced with the screw-driven extruder. Further to this, the well established and widely used universal paste extruder was 3D printed and subsequently assembled. The universal paste extruder is a popular gear-driven syringe-housed extruder, designed by Richard Horne (RichRap; http://richrap.blogspot.co.za), for RepRap and other 3D printers. The extruder is available online under a creative commons license (Attribution 3.0 Unported; Thingiverse #20733). The universal paste extruder has been used for the 3D printing of hydrogels, such as pastes and food materials, as well as ceramic materials. Furthermore, successful bioprinting was achieved using the universal paste extruder in Armstrong *et al.* (2016). Similar to the screw-driven extruder, the universal paste extruder required a standard NEMA 17 stepper motor for driving the rotation of the three printed gears. The extruder housed a Luer-lock syringe (10 mL) for extruding hydrogel material.

The assembly instructions for both the screw-driven extruder as well as the universal paste extruder is described. Furthermore, a critique of the initial experiments to determine hydrogel printability using both extruders is presented.

3.2 Methods & Materials

3.2.1 Screw-driven Extruder

Three-dimensional (3D) printing of the printed parts required for assembling the screw-driven extruder was performed using a RepRapPro Ormerod 3D printer, using 1.75 mm PLA filament with an 80 % infill. Table 3.1 highlights all the printed and non-printed parts, as well as the electronic components required for assembling the screw-driven extruder. Printed parts required for assembling the screw-driven extruder included a NEMA 17 stepper motor mount (Figure 3.1 A), a pneumatic drive piece (Figure 3.1 B) and an insulin syringe holder (Figure 3.1 C). A photograph of all of the components required for assembling the screw-driven extruder is presented in Figure 3.2. Initial experiments using extruder was conducted using agarose (Sigma; Cat. No. A9539). Agarose (0.6 % w/v) was dissolved in sterile double deionised water (ddH_2O) by heating to 90 ^{o}C. Dissolved agarose was promptly inserted into an insulin syringe (1 mL), housed within the screw-driven extruder. The printing process was initiated at room temperature.

Table 3.1: Bill of Materials required for screw-driven extruder assembly

Printed parts	Non-printed parts	Electronic components
1 x NEMA 17 stepper motor mount	2 x LM8UU linear bearing	1 x NEMA 17 stepper motor (with extended wires)
1 x pneumatic drive piece	1 x 8 mm lead screw with nut	
1 x syringe holder	1 x 8 mm aluminium stepper motor shaft coupler	
	2 x M8 (8 mm) x 300 mm smooth rod	
	4 x 5 mm grub screw	
	8 x M3 (3 mm) x 20 mm screw	
	2 x M3 (3 mm) x 500 mm screws	
	2 x M3 (3 mm) nut	

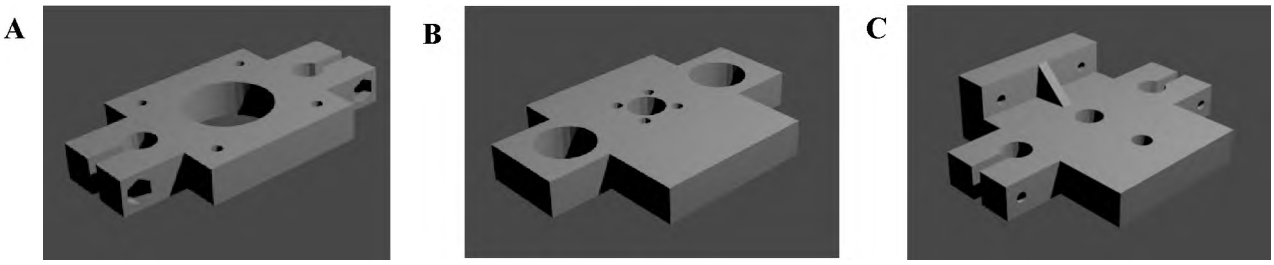

Figure 3.1: Three-dimensional (3D) printed parts required for screw-driven extruder assembly. A: NEMA 17 stepper motor mount. B: Pneumatic drive piece. C: Syringe holder. Stereolithography files were designed using SketchUp Make (v16.0.1). Images were rendered in Blender (v2.78).

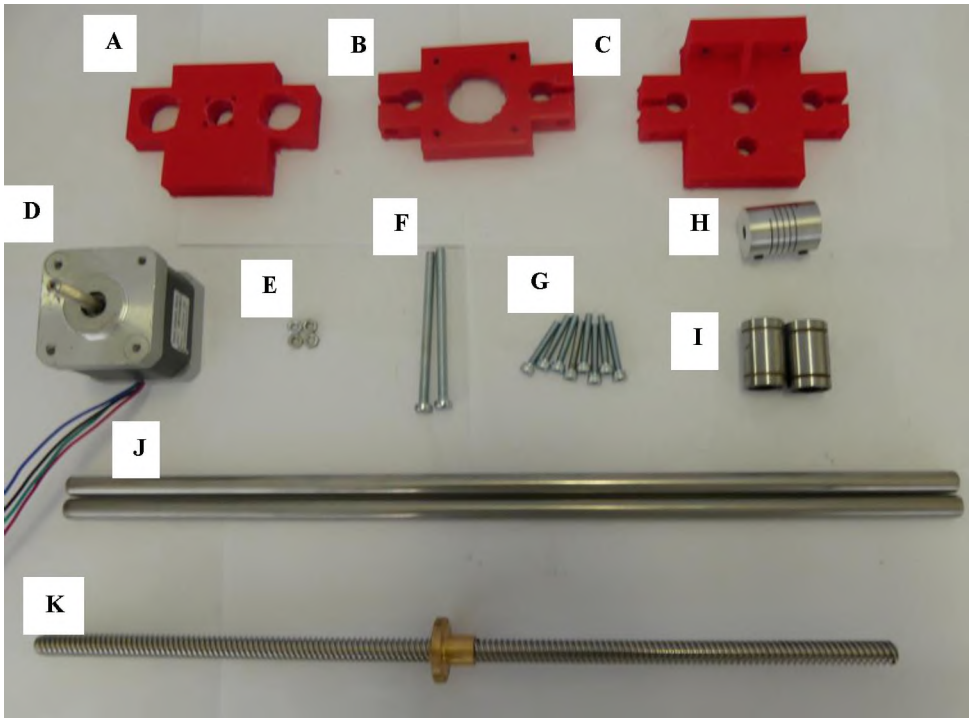

Figure 3.2: Required conmponents for screw-driven extruder assembly. A: Printed pneumatic drive piece. B: Printed NEMA 17 stepper motor mount. C: Printed syringe holder. D) NEMA 17 stepper motor (with extended wires). E: 4 x M3 nuts. F: 2 x M3 x 500 mm screws. G: 8 x M3 x 20 mm screws. H: 8 mm aluminium stepper motor shaft coupler (with 4 x grub screws). I: 2 x LM8UU linear bearings. J: 2 x M8 x 300 mm smooth rod. K: 8 mm lead screw with nut.

3.2.2 Universal Paste Extruder

The universal paste extruder used in the present study was originally designed to fit on the Quick-Fit X carriage (Thingiverse #19590). As the RepRap Prusa i3 originally made use of an X-carriage designed to fit a Greg's Wade extruder, modification of the universal paste extruder body was carried out. The body of the universal paste extruder was modified in SketchUp Make (v16.1.1449) software such that screw holes for mounting the extruder to the standard X-carriage of a RepRap Prusa i3 was made possible. Furthermore, the universal paste extruder traditionally makes use of a 3D printed GT2 belt pulley. In the present study, an aluminium GT2 pulley (with grub screws) was used instead of the printed belt pulley. Table 3.2 highlights all of the printed and non-printed parts, as well as the electronic components, required for assembling the universal paste extruder. Printing of the printed parts (Figure 3.3) was performed using a Wanhao Duplicator i3 3D printer, using 1.75 mm PLA filament with an 80 % infill. A photograph of all of the components required for assembling the universal paste extruder is presented in Figure 3.4. Printing experiments using the universal paste extruder was done using sodium alginate sodium salt (Sigma; Cat. No. 180947) dissolved in sterile ddH_2O at either 1 or 2 % (w/v).

Table 3.2: Bill of Materials required for universal paste extruder assembly

Printed parts	Non-printed parts	Electronic components
1 x double gear	4 x 624 bearing	1 x NEMA 17 stepper motor (with extended wires)
1 x large gear	1 x 608 bearing	
1 x drive gear	1 x M8 (8 mm) x 20 mm smooth rod	
1 x syringe cap	1 x GT2 pulley (with grub screw)	
1 x extruder body	1 x 30 cm GT2 rubber belt	
1 x idler	5 x M3 (3 mm) x 10 mm screw	
	1 x M3 (3 mm) x 20 mm screw	
	2 x M3 (3 mm) x 40 mm screws	
	1 x M3 (3 mm) x 45 mm screw	
	3 x M3 (3 mm) nut	
	1 x M4 (3 mm) a 60 mm screw	
	1 x M4 (4 mm) x 75 mm screw	
	1 x M4 (4 mm)x 35 mm screw	
	32 x M4 (4 mm) washers	
	2 x M4 (4 mm) nutlock	
	1 x 15 mm spring	

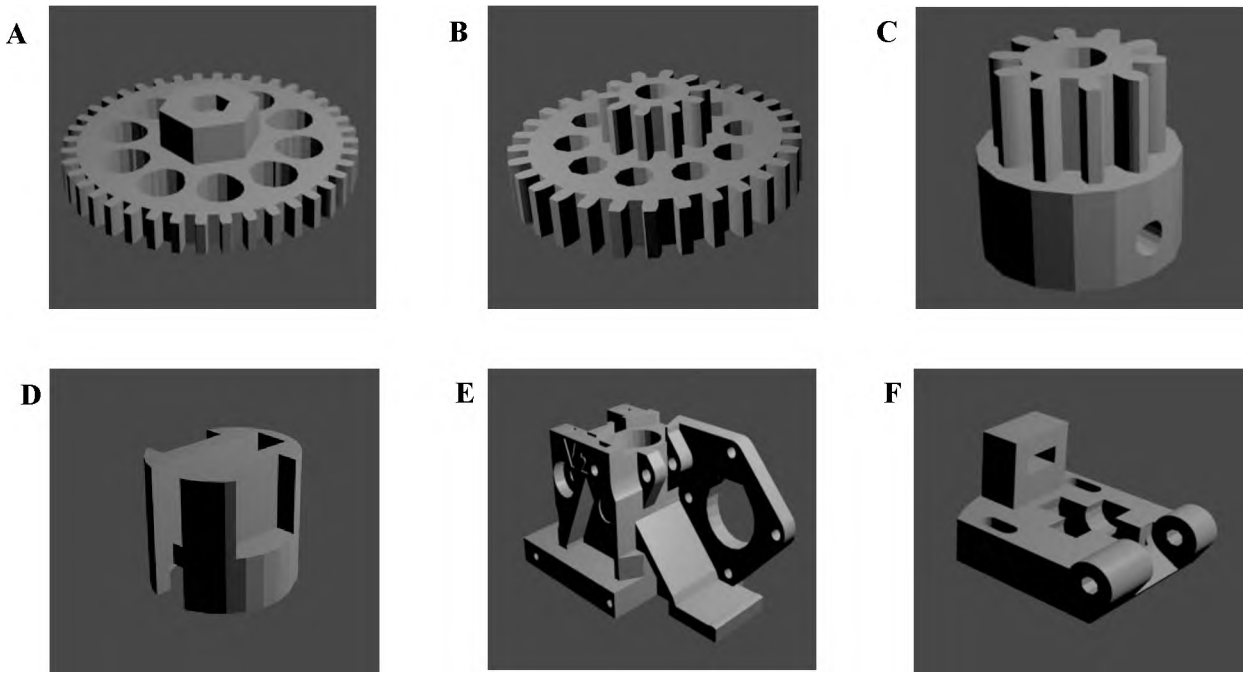

Figure 3.3: Three-dimensional (3D) printed parts required for univeral paste extruder assembly. A: Large gear. B: Double gear. C: Drive gear. D: Syringe cap. E: Extruder body. F: Idler. Images were rendered in Blender (v2.78).

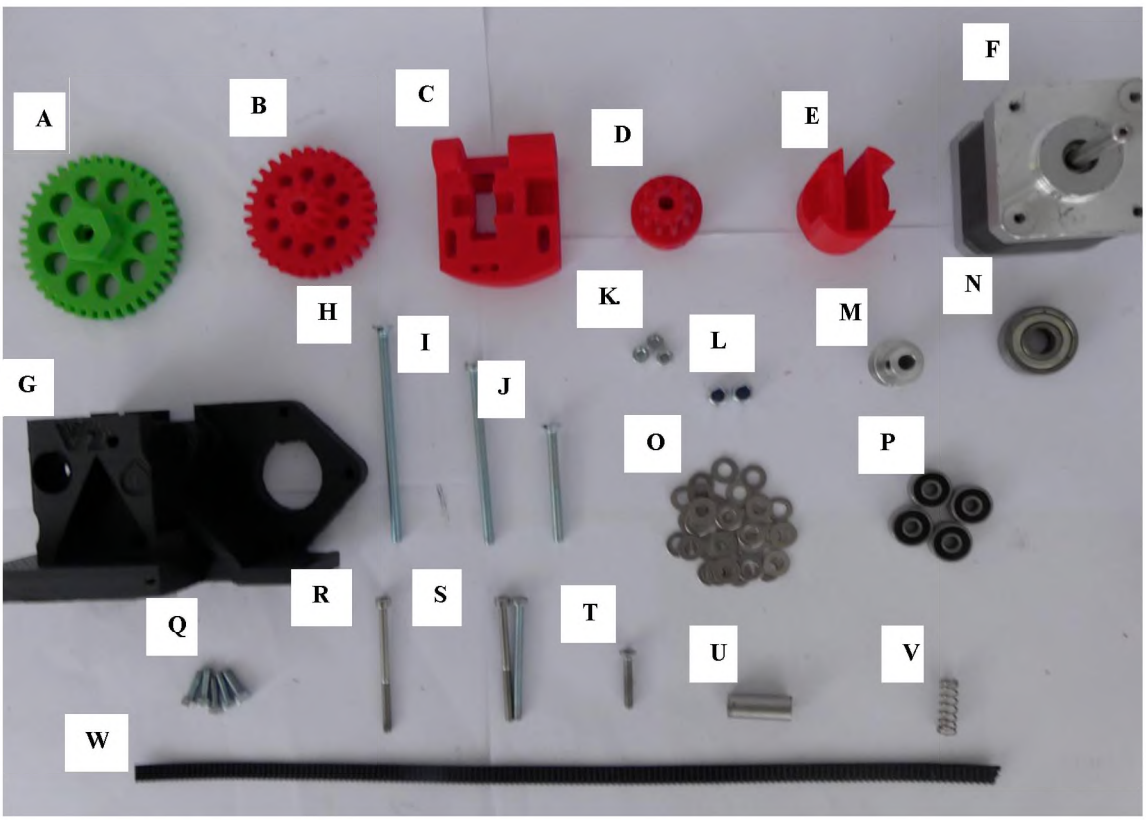

Figure 3.4: Required conmponents for universal paste extruder assembly. A: Printed large gear. B: Printed double gear. C: Printed idler. D: Printed drive gear. E) Printed syringe cap. F: NEMA 17 stepper motor (with extended wires). G: Printed extruder body. H: M4 x 75 mm screw. I: M4 x 60 mm screw. J: M4 x 35 mm screw. K: M3 nuts. L: M4 nutlocks. M: GT2 pulley (with grub screws). N: 608 bearing. O: M4 washers. P: 623 bearings. Q: M3 x 10 mm screws. R: M3 x 45 screw. S: M3 x 40 mm screws. T: M3 x 20 mm screw. U: M8 x 20 mm smooth rod. V: 15 mm spring. W: 30 cm GT2 rubber timing belt.

3.3 Results

3.3.1 Screw-driven Extruder Assembly

1. A NEMA 17 stepper motor (with extended wires) was attached to the printed stepper motor mount by screwing with four M3 x 20 mm screws (Figure 3.5 A).
2. An 8 mm lead screw was secured to the stepper motor by attaching the motor and the lead screw to the 8 mm aluminium stepper motor shaft coupler by screwing both ends with two grub screws per side (Figure 3.5 B).
3. Two LM8UU linear bearings were inserted into the bearing holders in the printed pneumatic drive piece (Figure 3.5 C).
4. Two M8 x 300 mm smooth rods were slid through the linear bearings (Figure 3.5 D).
5. The printed stepper motor mount as well as the printed syringe holder was attached along either side of the printed pneumatic drive piece by sliding them along both smooth rods (Figure 3.5. E).
6. An 8 mm lead screw was secured to the printed pneumatic drive piece by tightly inserting the lead screw nut into the drive piece.
7. The printed stepper motor mount and the printed syringe holder was tightly secured to the smooth rods by screwing both printed parts to the rods with two M3 x 20 mm screws and two M3 nuts per part (Figure 3.5. F).
8. The entire screw-driven extruder was mounted to the Prusa i3 by screwing the printed syringe holder to the X-carriage of the Prusa i3 using two M3 x 500 mm screws (Figure 3.5 G).
9. The NEMA 17 stepper motor cables were connected to the E0 plug on the RAMPS 1.4 board.

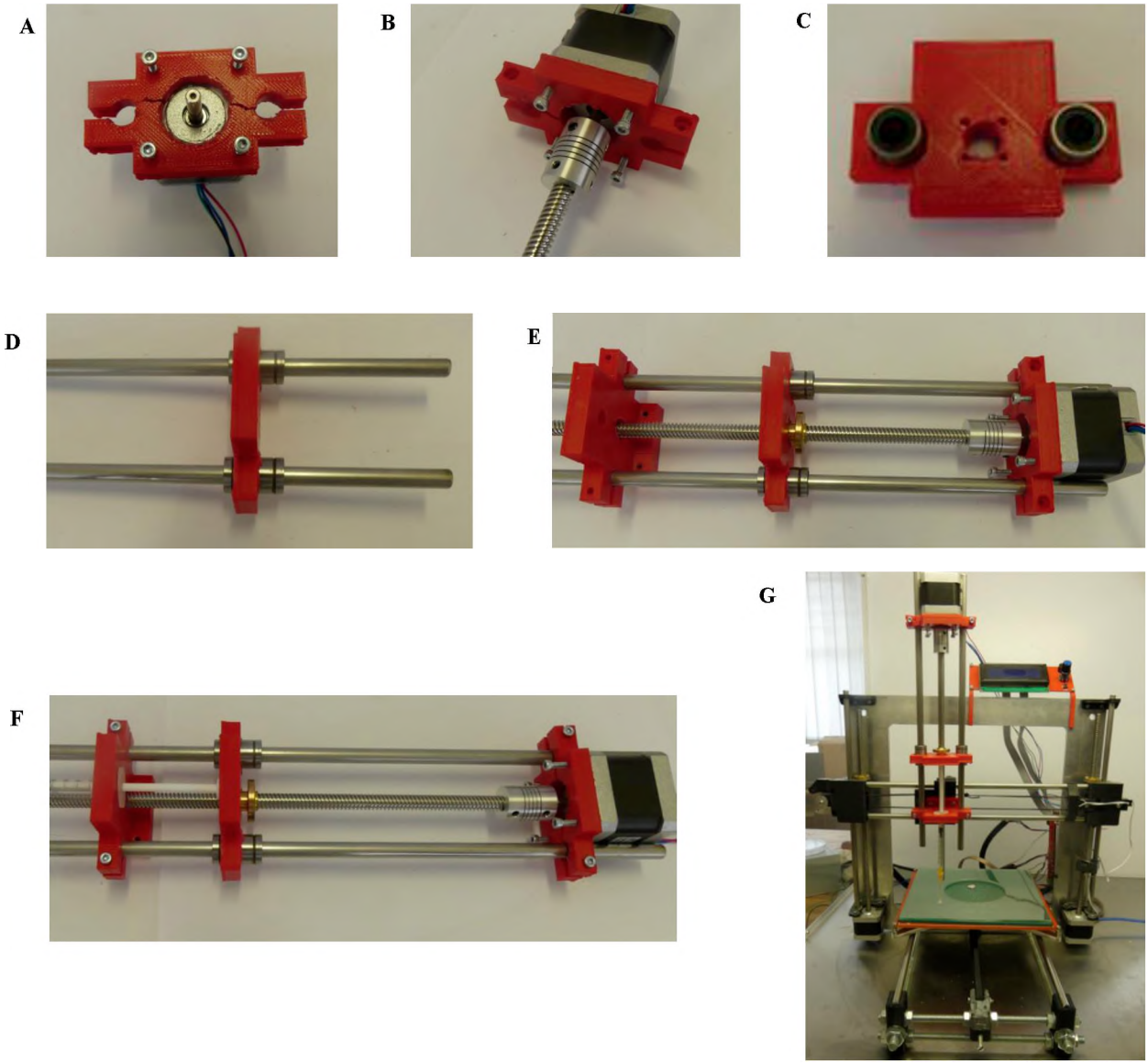

Figure 3.5: Screw-driven extruder assembly process. A: Stepper motor mounting. B: Lead screw attachment. C: LM8UU linear bearing insertion. D: Smooth rod incorporation. E: Stepper motor mount and syringe holder attachment. F: Smooth rod attachment. G: Prusa i3 mounting.

3.3.2 Universal Paste Extruder Assembly

1. A NEMA 17 stepper motor was attached to the printed extruder body using four M3 x 10 mm screws (Figure 3.6 A).
2. The printed motor drive gear (small gear) was attached to the NEMA 17 stepper motor. An M3 nut was first inserted into the nut holder in the motor drive gear. The motor drive gear was then secured to the stepper motor by screwing with an M3 x 10 mm screw, through the previously inserted M3 nut (Figure 3.6. B).
3. The printed large gear was mounted to the extruder body by sliding an M4 x 75 mm screw through the gear, followed by eight M4 washers and a 624 bearing. The M4 x 75 mm screw (with washers and bearing) was inserted through the extruder body by sliding the screw through the GT2 pulley (positioned between two M4 washers) in the middle of the extruder body. The screw was secured to the extruder body by sliding an additional 624 bearing, followed by seven M4 washers and an M4 nutlock to the end of the screw (Figure 3.6 C).
4. A 624 bearing was inserted into the printed syringe cap by sliding an M3 x 20 mm screw through the bearing and syringe cap and securing with an M3 nut (Figure 3.6 D).
5. A GT2 rubber timing belt was fed through the syringe cap bearing and secured to the extruder body by passing the belt through the GT2 aluminium pulley (using tweezers) and inserting the belt in the space between the NEMA 17 stepper motor and the printed extruder body.
6. The printed double gear was secured to the extruder body by sliding an M4 x 60 mm screw through the gear, followed by five M4 washers and a 624 bearing. When inserting the screw through the extruder body, the GT2 belt was tightly secured to the extruder. The screw was secured to the extruder body by sliding an additional ten M4 washers, followed by an M4 nutlock (Figure 3.6 E).
7. A 608 bearing was attached to the printed idler by inserting an M8 x 20 mm smooth rod through the 608 bearing and inserting into the idler (Figure 3.6 F).
8. The base of the idler was secured to the extruder body using an M4 x 35 mm screw (Figure 3.6 G). Two M3 nuts were inserted into the spaces provided at the top of the

extruder body. The top of the idler was secured to the extruder body using an M3 x 45 mm screw (with a 15 mm spring) (Figure 3.6 H).

9. The entire universal paste extruder was mounted to the Prusa i3 by screwing the printed extruder body to the X-carriage of the Prusa i3 using two M3 x 40 mm screws (Figure 3.6 I).
10. The NEMA 17 stepper motor cables were connected to the E0 plug on the RAMPS 1.4 board.

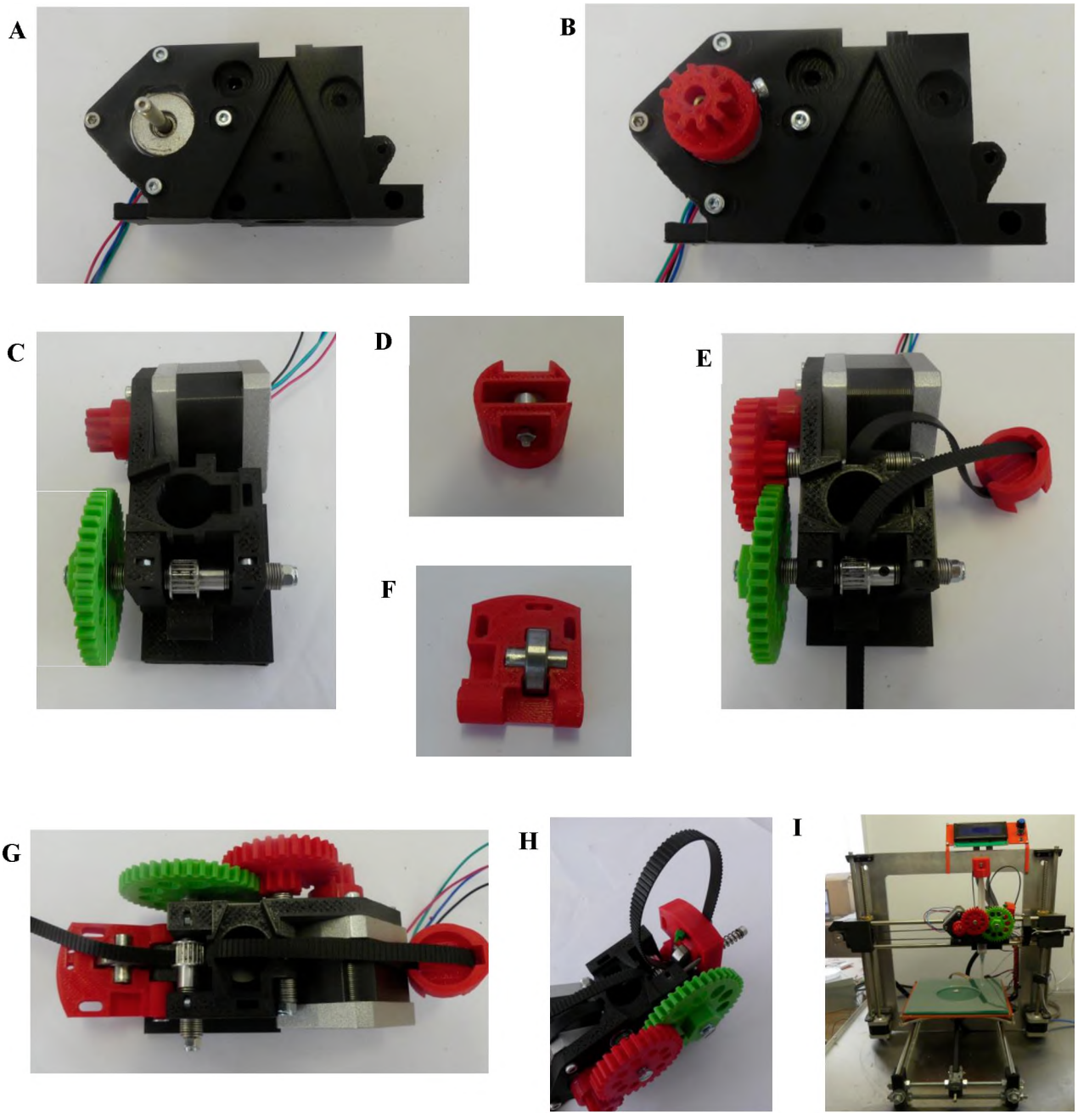

Figure 3.6: Universal paste extruder assembly process. A: Stepper motor mounting. B: Drive gear attachment. C: Large gear attachment. D: Syringe cap bearing attachment. E: Double gear attachment. F: Idler bearing attachment. G: Idler attachment.

3.4 Troubleshooting & Discussion

3.4.1 Screw-driven Extruder

The simplistic mechanical design of the screw-driven extruder made it an ideal cadidate for conducting initial experiments with. The extruder design was based on designs commonly used for 3D printing of a variety of hydrogels with varying viscosities. Screw-driven extrusion mechanisms are ideal for hydrogel printing as a wide-range of material properties are compatibile with the process (Murphy & Atala, 2014). Testing the printability of hydrogels using the screw-driven extruder was intially conducting using the algal polysaccharide agarose. Agarose is a linear polysaccharide consisting of β-1,3 linked D-galactose and α-1,4linked 3,6-anhydro-α-L-galactose residues (Figure 1.3 A) (Normand *et al.*, 2010). Agarose (0.6 % w/v) was heated to around 90 ^{o}C before being inserted into an insulin syringe (1 mL). The print was promptly initiated at room temperature. A simple design of a video game keychain was downloaded online and is available under a creative common license (Creative Commons – Attribution, Thingiverse #197209). A video clip of the agarose printing process can be found in the Supplementary Material (Video S2). The inability to fully control gelation temperatures following agarose extrusion resulted in spreading of the gel on the print surface. The general shape of the construct was however produced to a certain degree when printing agarose in a single layer. While the initial experiments using the screw-driven extruder showed potential for refinement and printability of a wide range of hydrogels, the length of the extruder resulted in it being rather unstable about the X-carriage. The low maximum loading volume of 1 mL was also considered a disadvantage as several larger, multi-layer constructs require greater material deposition volumes. Refinements to the design might involve increasing the circle diameter in the printed syringe holder (Figure 3.1 C) such that larger syringes may be housed. Additionally, increased stability about the X-carriage may be achieved if the overall length of the extruder were shortened. This could simply be accomplished by shortening the length of the M8 smooth rods (Figure 3.2 J) and the 8 mm lead screw (Figure 3.2 K). Due to the aforementioned disadvantages associated with using the screw-driven extruder, interest into developing other extruder units were carried out. As a result, the popular gear and belt-driven universal paste extruder was constructed and primarily used for future experiments.

3.4.2 Universal Paste Extruder

The universal paste extruder is a widely used extruder which makes use of a belt-driven system consisting of three gears. The drive gear (Figure 3.3 C) is secured to a NEMA 17 stepper motor (Figure 3.6 B) and drives the rotation of the double gear (Figure 3.3 B). The double gear rotates the large gear (Figure 3.3 A), which controls the movement of a GT2 rubber timing belt, resulting in the downward/upward movement of a syringe plunger. The gear and belt-driven mechanism enabled sufficient control of material deposition from the syringe tip. Moreover, syringe needles of varying gauges could be fit to the syringe, allowing materials of different viscosities to be extruded. The needle gauge size selected ought to depend on the properties of the material to be extruded. Materials of relatively high viscosities often required large amounts of applied pressure for material deposition. This would result in a pressure build up within the syringe and often times would result in dripping of material following applying direct pressure to the syringe. In the present study, sodium alginate (1 & 2 % w/v) was used for testing the effect various needles had on controlling the deposition of the hydrogel following removal of an applied pressure to the syringe. A comparison of needle gauge ability for controlled deposition of sodium alginate hydrogels is presented in Table 3.3.

Table 3.3: Comparison of needle gauge efficiency for controlled sodium alginate deposition. Sodium alginate (1 and 2 % w/v) solutions were loaded in 10 mL syringes and extruded using the universal paste extruder. Pronterface controller software was used (100 mm/min; 100 % print speed).

	Needle gauge inner diameter (mm)			
	1.37	**0.84**	**0.34**	**0.26**
1 % (w/v) alginate	Controlled deposition	Slight dripping	Dripping	Excessive dripping
2 % (w/v) alginate	Controlled deposition	Controlled deposition	Dripping	Excessive dripping

It was noted that when extruding sodium alginate (1 % & 2 % w/v) solutions using low diameter needles (0.26 mm, 0.34 mm), large amounts of applied pressure would result in dripping of

alginate after the motor had stopped. Extrusion of alginate solutions using syringe needles of larger (< 0.84 mm) inner diameters required comparatively lower amounts of applied pressure and thus would allow for controlled deposition of alginate. However, larger needle gauges often resulted in excessive spreading of alginate solutions when compared to lower diameter needles. Ultimately, selecting the ideal needle gauge depends on the required resolution of the printed construct as well as the properties of the material to be extruded. Furthermore, determining the particular printing parameters such as width, height and speed of path deposition is all required for printing of materials which do not leave gaps or result in material overprinting in the printed structure (Liberski, 2016). In terms of 3D alginate printing, alginate solutions of low concentration often results in wide constructs being deposited. Contrastingly, high alginate concentrations produce narrow constructs. The effect to which various needle gauge sizes had on sodium alginate (2 % w/v) rate of extrusion was later determined (Table 3.4).

Table 3.4: Comparison of sodium alginate flow-rate deposition. Sodium alginate (2 % w/v) was loaded in 10 mL Luer-lock syringes and extruded using the universal paste extruder. Sodium alginate was extruded for 20 seconds. Pronterface controller software was used with the following configurations: 100 mm/min dispensing rate; 100 % print speed) (n=2).

Needle gauge inner diameter (mm)				
	1.37	**0.84**	**0.34**	**0.26**
Flow rate (mL/min)	6.3±(0.42)	4.08± (0.17)	3.57±(0.04)	3.48±(0.08)

As predicted, the rate of alginate deposition uniformly increased with needle gauge diameter when the print speed was set at a constant value (100 %). Printing complete and accurate constructs which do not leave gaps or overprinted paths requires experimental determination dependant on the physical properties (such as viscosities) of the material being printed, the printing parameters, as well as the needle gauge sizes such that the optimal rate of material deposition may be achieved.

The universal paste extruder is most commonly used for printing pastes, such as ceramics or food materials, but has also been used for bioprinting applications. Recently, Armstrong *et al.* (2016) reported a two-step 3D bioprinting process to engineer bone and cartilage architectures using the

universal paste extruder. The group used a 5 mL syringe, whereas the extruder used in the present study housed a 10 mL Luer-lock syringe which provided ample volume for printing large multi-layered constructs. Compared to the screw-driven extruder, the universal paste-extruder provided far greater stability about the Prusa i3 X-carriage. As a result, deposition of hydrogel material from the syringe was more spatially controlled. As such, the universal paste extruder was used as the primary extruder for the remainder for the study.

`

Chapter 4: Mammalian cell culture and sodium alginate encapsulation

4.1 Introduction

Adipose tissue is a rich source of multipotent and unipotent stem cells capable of, but not limited to, commitment into mature adipocytes. Mesenchymal stem cells (MSC) are of the several stem and precursor cell types present within adipose tissue (Baer and Geiger, 2012). Frequently used *in vitro* adipose tissue models make use of monolayered preadipocytes induced for adipogenic differentiation (Kang *et al.*, 2009). Commonly used end-point assays used for detecting adipogenic differentiation includes Oil Red O staining of intracytoplasmic lipids (Kinkel *et al.*, 2005). Additionally, Nile red staining may be used as an intracytoplasmic lipid detection method by fluorescence microscopy (Greenspan *et al.*, 1985; Alonzo & Mayzaud, 1999). While cell staining, proteomic analysis and gene profiling have all been successfully used for detecting cellular differentiation, these methods all fail to monitor cells in a continuous manner due to the invasive nature they impose. There have therefore been increased efforts in achieving detection of cellular differentiation in real-time. Electric Cell-Substrate Impedance Sensing systems have successfully been used for monitoring cellular differentiation based on changes in cell morphologies and proliferation associated when cells undergo commitment toward a differentiation lineage (Angstmann *et al.*, 2011; Bagnaninchi & Drummond, 2011; Reitinger *et al.*, 2012; Kramer *et al.*, 2014).

A major downside to conventional 2D monolayered *in vitro* adipose tissue models lies in that they fail to mimic the complex vascularised network present in native adipose tissues. Future physiologically relevant adipose tissue models will rely largely on the proper incorporation of vasculature within tissue constructs. Incorporation of vasculature may improve tissue viability (due to enhanced nutrient and waste transport) as well as induce structural organisation both *in vitro* and *in vivo* (Sodian *et al.*, 2002). Blood vessels, lined with endothelial cells (EC), belong to the largest organs of our body (Bouïs *et al.*, 2001). The formation of blood vessels is dependent upon a process called angiogenesis, which is defined as the growth of new blood vessels from pre-existing vessels. Through angiogenesis, cellular tissues are able to attain an adequate blood

supply (Nakatsu *et al.*, 2003). The process is tightly regulated by angiogenic factors, such as basic fibroblast growth factor (bFGF) and VEGF, which stimulate EC migration, differentiation and proliferation to form new lumen vessels (Favot *et al.*, 2003). Various physiological and pathophysiological processes make use of EC for *in vitro* models, especially in angiogenesis (Bouïs *et al.*, 2001). Human-derived endothelial cells are routinely harvested from the human umbilical vein and are the most commonly used cell line for the *in vitro* study of angiogenesis (Cheung, 2007). Termed human umbilical vein endothelial cells (HUVEC), HUVEC cultures grown within hydrogels, such as collagen or fibrin, form defined lumens surrounded by multiple polarised EC that closely resemble those observed *in vivo* (Nakatsu *et al.*, 2003). Endothelial cells play a pivotal role in tissue engineering applications where the engineered tissue requires vascularisation for achieving nutrient, waste and growth/signalling transport (Kolesky *et al.*, 2014). In terms of adipose tissue engineering, vascularisation is of utmost importance as native adipose tissues are generally highly vascularised (Hausman & Richardson, 2004). *In vitro* adipose tissue models which incorporate vasculature would therefore provide more relevance and would contribute to viability during tissue growth. Vascularised adipose tissue models have been created through the use of adipogenic differentiated adipose-derived stem cells (ad-SC), co-cultured with HUVEC, using silk fibroin scaffolds (Kang *et al.,* 2009), fibrin constructs (Kachgal & Putnam, 2011) as well as collagen/alginate microspheres (Yao *et al.*, 2013).

Sodium alginate is a water soluble biomaterial commonly extracted from the cell walls of brown seaweed. Sodium alginates are widely using in tissue engineering as natural polymer scaffold materials for immobilising cells. Alginate hydrogels have also been used as drug delivery vehicles (Lee & Mooney, 2001; Tønnesen & Karlsen, 2002). Due to the ability to form gels of varying elastic properties at physiological conditions which preserve cell viability and function, sodium alginate gels have been widely used for various means of cell encapsulation (Andersen *et al.*, 2015). Furthermore, the low toxicity, mild gelation and relatively low cost of alginate have all aided in the investigation of alginate for biomedical applications (Lee & Mooney, 2001). Structurally, sodium alginate consist of linear 1,4 linked β-D-mannuronic acid (M) and its C5-epimer α-L-guluronic acid (G) (Figure 1.3 B.) (Andersen *et al.*, 2015). When dissolved, sodium alginate forms a concentration-dependant viscous solution (Song *et al.*, 2011). Cross-linking of alginate polymers takes place when in the presence of daivalent cations (calcium chloride being the most commonly used means for inducing alginate gelation). Gel properties such as elasticity,

porosity and stability are all influenced by the type and concentration of alginate. Additionally, selecting the type and amount of gel forming ions may also influence the resulting properties of alginate hydrogels, allowing for further optimisation of elasticity, swelling and stability (Andersen *et al.*, 2015). A major benefit to the use of alginate hydrogels in tissue engineering lies in the ability alginate gels have for structural modification, allowing for controlled degradation rates and increased cell attachment and spreading. Unmodified alginate hydrogels have unpredictable degradation rates due to the release of high and low molecular weight alginate strands post alginate gelation (Shoichet *et al.*, 1996). A method for developing partially oxidised alginate was first presented in Bouhadir *et al.* (2001), whereby the ability to control alginate degradation was achieved. The methods for partially oxidising alginates were then further refined by Mooney and co-workers (Wang *et al.*, 2012). Partial oxidation of alginate, using sodium periodate, alters the uronate residues to an open-chain adduct, resulting in the adduct behaving as an acetal group susceptible to hydrolysis (Bouhadir *et al.*, 2001). Oxidised alginates may be further conjugated to cell attachment peptide sequences. Peptide-coupling alginate hydrogels have shown to significantly promote cell attachment and spreading (Dennis *et al.*, 2015). Cell attachment peptides, especially arginine-glycine-aspartic acid (RGD) sequences, have been widely used for modifying the chemical and physical properties of alginate hydrogels (Andersen *et al.*, 2015). Kang *et al.* (2011) found that culturing human adipose-derived stromal cells in RGD-conjugated alginate significantly stimulated focal adhesion kinase (FAK), integrin α1 and vinculin gene expression, as well as enhanced adipogenic differentiation. These findings are supported by Jia *et al.* (2014), where coupling RGD-sequences to alginate hydrogels was shown to aid in human ad-SC cell adhesion, spreading and proliferation, as well as promote integrin expression (Jia *et al.*, 2014). Other structural modifications made to alginate hydrogels include that of methacrylated alginate. Photocrosslinked alginates may be synthesised by functionalising alginate with methacrylate linkages, allowing gelation to be induced via exposure to ultraviolet (UV) light, in the presence of a photoinitiator (Jeon *et al.*, 2009).

The following chapter describes the culturing of ad-HMSC and validation of ad-HMSC multilineage differentiation potential. Oil Red O and Alizarin Red S staining was performed to detect the adipogenic and osteogenic differentiation potential of ad-HMSC, respectively. Furthermore, real-time analysis of cellular impedance changes taking place when ad-HMSC were induced for adipogenic and osteogenic differentiation was investigated. A description of the

protocols employed for HUVEC cell culture is also described. Cell viability of HUVEC and ad-HMSC seeded alginate hydrogels was investigated by WST-1 cell proliferation assays, as well as by live/dead cell staining.

4.2 Methods and materials

4.2.1 Human Umbilical Vein Endothelial Cell (HUVEC) culture

Human Umbilical Vein Endothelial Cells (HUVEC) (Cat No. 8000) were purchased from ScienCell (CA, USA) and received at passage 1. Expansion of cell cultures was achieved using complete endothelial cell medium (ECM) (Cat No. 1001) purchased from ScienCell and prepared as per manufacturers instructions. Complete ECM consisted of basal endothelial medium (Cat. No. 1001-b), 5 % (v/v) foetal bovine serum (FBS, Cat. No. 0025), 1 % (v/v) of endothelial cell growth supplement (ECGS, Cat. No. 1052) and 1 % (v/v) penicillin/streptomycin solution (P/S, Cat. No. 0503). For sodium alginate cell encapsulation experiments (described later), HUVEC was cultured in all-in-one endothelial cell growth medium (ECGM, Sigma, Cat. No. 211-500).

A fibronectin coated 75 cm^2 culture flask was prepared by incubating the flask with a solution of fibronectin (2 $\mu g/cm^2$), (fibronectin from bovine plasma, Sigma Cat. No. F4759) which was incubated overnight in a humidified incubator at 37 ^oC, in a 5 % (v/v) CO_2 atmosphere. Following 12 hours of incubation, fibronectin was aspirated and 15 mL complete ECM was added to the flask. Primary HUVEC cells were thawed in a 37 ^oC water bath and promptly transferred to the 75 cm^2 culture vessel within a sterile field. Cells were plated at a seeding density of 5000 cells/cm^2. The culture flask was left undisturbed for 16 hours in a humidified incubator at 37^oC, in a 5 % (v/v) CO_2 atmosphere. A complete media change to remove unattached cells and residual dimethyl sulfoxide (DMSO, Sigma) was performed the morning after establishing a culture. Culture medium was refreshed every three days thereafter, until the culture reached approximately 70% confluency. Thereafter, culture medium was refreshed every other day until the culture reached approximately 90% confluency.

Fibronectin-coated culture vessels (2 $\mu g/cm^2$) were prepared one day before subculturing. The culture was subcultured upon reaching 90% confluency or above. Prior to trypsinisation, all

required components were warmed to room temperature. Culture medium was removed and cells were rinsed with Ca^{2+}/Mg^{2+}-free Dulbecco's phosphate buffered saline (DPBS, Sigma). Next, 4 mL Ca^{2+}/Mg^{2+}-free DPBS (pH 7.4) was added to the flask followed by 2 mL trypsin/EDTA solution (Lonza, Cat. No. 5012). The flask was incubated at 37 ^{o}C for approximately 2 minutes until the cells had completely rounded up. The trypsin solution was then transferred to a 15 mL centrifuge tube containing 5 mL complete ECM. The flask was placed back at 37 ^{o}C for a further 2 minutes. Complete ECM (4mL) was added to the flask to resuspend trypsinsed cells, which was then added to the same 15 mL centrifuge tube which was subjected to centrifugation at 1000 rpm for 5 minutes. Following centrifugation the supernatant was removed and pelleted cells were resuspended in 1 mL complete ECM. A cell count was performed using a haemocytometer and trypan blue staining. Cells were seeded at 5000 cells/cm^2 onto fibronectin-coated culture vessels as required. Cells were used at passages 2-3.

4.2.2 Adipose-derived Human Mesenchymal Stromal Stem Cell (ad-HMSC) culture

Adipose-derived Human Mesenchymal Stromal Stem Cells (ad-HMSC) were received as a gift from Prof. M.S. Pepper (University of Pretoria) at passage 4. Similarly to HUVEC cell culture, ad-HMSC expansion was achieved by culturing cells with complete mesenchymal stem cell medium (MSCM) purchased from ScienCell (CA, USA) (Cat No. 7501). Complete MSCM consisted of basal mesenchymal medium (Cat No. 7501-b), 5 % (v/v) FBS, 1 % (v/v) mesenchymal stem cells growth supplement (MSCGS, Cat. No. 7552) and 1 % (v/v) P/S solution. For sodium alginate hydrogel encapsulation (described later), ad-HMSC were cultured in complete minimum essential medium eagle (MEM) alpha modification (α-MEM, Sigma, Cat. No. M2414) containing 1 % (v/v) penicillin/streptomycin/amphotericin B (P/S/A, Sigma, Cat. No. A5955), 10 % (v/v) FBS (Sigma) and 4 mM L-glutamine (Sigma, Cat. No. G7513).

Poly-L-lysine coated culture vessels were prepared by incubating flasks with a solution of poly-L-lysine (1 mg/mL), (poly-L-lysine stock solution, 10 mg/ml, ScienCell cat. no. 0413) one day prior to subculturing. Prior to cell seeding, poly-L-lysine was aspirated and the flask rinsed twice with Ca^{2+}/Mg^{2+}-free DPBS (pH 7.4). Subculturing of ad-HMSC was performed as described previously for HUVEC subculturing. Cells were seeded at 5000 cells/cm^2 and incubated at 37 ^{o}C, in a humidified 5 % (v/v) CO_2 atmosphere. Cells were used at passages 4-6.

`

4.2.3 Adipose-derived Human Mesenchymal Stromal Stem Cell (ad-HMSC) differentiation

4.2.3.1 Osteogenic differentiation

Osteogenic differentiation of ad-HMSC was based on the protocol described in Wang *et al.* (2016). Cells were grown to confluence and maintained in complete MSCM for an additional 24 hours. One day post confluence, cells were washed with PBS and fed using osteogenic differentiation media (ODM). Osteogenic differentiation media was made up of Dulbecco's Modified Eagle Medium (DMEM, Sigma), 10 % FBS (Sigma), 1 % penicillin/streptomycin/amphotericin B (PSA, Sigma), 100 nM dexamethasone (Sigma, Cat. No. D4902), 50 µM L-ascorbic acid (Sigma, Cat. No. A0278) and 10 mM β-glycerophosphate (Sigma, Cat. No. G9422). Dexamethasone was dissolved in methanol. Ascorbic acid and β-glycerophosphate were dissolved in sterile ddH_2O. Osteogenic differentiation media was replaced every 3 days for 21 days.

4.2.3.2 Adipogenic differentiation

Adipogenic differentiation of ad-HMSC was based on the protocol described in Chen *et al.* (2009) with slight modifications. Cells were grown to confluence and maintained in complete MSCM for an additional 24 hours. One day post confluence, cells were washed with PBS and fed using adipogenic induction media (AIM) for 3 days. AIM was made up of DMEM, 10 % FBS, 1 % PSA, 1 µM dexamethasone, 10 µg/mL human insulin (Sigma, Cat. No I3536), 0.5 mM 3-isobutyl-1-methylxanthin (Sigma, Cat No. I5879) and 2 µM rosiglitazone (Sigma, Cat. No. R2408). Dexamethasone was dissolved in methanol. Human insulin was dissolved in sterile ddH_2O. IBMX was dissolved in ethanol. Rosiglitazone was dissolved in DMSO. Three days after induction, media was replaced and cells were fed with adipogenic maintenance media (AMM) consisting of DMEM, 10 % FBS, 1 % PSA and 10 µg/mL human insulin only for 3 days. Induction/maintenance cycles involved growing cells for 3 days in AIM followed by 3 days in AMM. Cycles would repeat for differentiation periods longer than 6 days.

4.2.4 Cryopreservation of mammalian cell

Following trypsinisation, HUVEC and ad-HMSC cells from confluent 75 cm^2 flasks were resuspended in complete ECM and complete MSCM, respectively. Cells were then centrifuged at

`

1000 rpm for 5 minutes. Pelleted cells were resuspended in 1 mL cryopreservation media (10 % (v/v) DMSO in complete ECM (for HUVEC) or complete MSCM (for ad-HMSC)). Solutions were transferred to cryopreservation vials and kept on ice for one hour before storage at -80 °C. For long term storage, cryopreserved cells were transferred to liquid nitrogen 24 hours after storage at -80 °C.

4.2.5 Oil Red O staining

Adipogenic differentiation was detected using Oil Red O (Sigma, Cat. No. O0625) staining on 9 days differentiation ad-HMSC cultured on 24-well plates. An Oil Red O stock solution was prepared at a concentration of 3.5 % (w/v) by dissolving in 100 % isopropanol and filtering (0.2 µm). The Oil Red O stock solution was later used to prepare an Oil Red O working solution which consisted of 60 % (v/v) Oil Red O stock solution and 40 % (v/v) sterile ddH_2O. The working solution was left at room temperature for 30 minutes followed by filtering (0.2 µm). Media (AIM) was discarded and cells were briefly washed with Ca^{2+}/Mg^{2+}-free DPBS (pH 7.4) for 5 minutes. Cells were then incubated for 5 minutes in 10 % (w/v) formalin at room temperature after which fresh formalin was added and cells incubated at room temperature for a further one hour. The 24-well plate was wrapped in parafilm to prevent drying. Formalin was removed and wells were washed with 60 % (v/v) isopropanol. Wells were allowed to dry completely before the addition of Oil Red O working solution. The plate was incubated at room temperature for 10 minutes after which Oil Red O was removed and wells washed four times with sterile ddH_2O. Cells were viewed using a Zeiss AxioVert.A1 FL-LED Fluorescence Microscope at 200X magnification with a Ph 2 phase contrasting filter. Full colour images were captured using a Samsung Galaxy S4 smartphone at 218X magnification.

4.2.6 Nile Red staining

Intracytoplasmic neutral lipids were detected using Nile red (Sigma, Cat. No. 19123) staining on 9 days differentiation ad-HMSC induced for adipogenic differentiation grown on 24-well plates. A 1 mM Nile red stock solution was made by dissolving Nile red in DMSO. From the Nile red stock solution, a 200 nM working solution was made by diluting with Ca^{2+}/Mg^{2+}-free DPBS (pH 7.4). Adipogenic induction media was discarded and cells were rinsed with Ca^{2+}/Mg^{2+}-free DPBS (pH 7.4). Nile red working solution (300 µL) was added to each of the wells at room

temperature for 30 minutes. Nile red working solution was removed and cells were rinsed with Ca^{2+}/Mg^{2+}-free DPBS (pH 7.4). A Hoechst 33342 (Sigma, Cat. No. B2261) stain was performed by incubating cells in a 1:1000 (Hoescht:DPBS) solution for 90 seconds. Hoescht was removed and cells were rinsed with Ca^{2+}/Mg^{2+}-free DPBS (pH 7.4). Cells were viewed using a Zeiss AxioVert.A1 FL-LED Fluorescence Microscope at 200X magnification with a Ph 2 phase contrasting filter. Neutral lipids were detected using the fluorescein isothiocyanate (FITC) filter (495 nm/519 nm), polar lipids were detected using the red fluorescent protein (dsRed) filter (563 nm/581 nm) and nuclei were detected using the 4',6-diamidino-2-phenylindole (DAPI) filter (358 nm/463 nm).

4.2.7 Alizarin Red S staining

Osteogenic differentiation was detected using Alizarin Red S (Sigma, Cat. No. A5533) staining on 21 days differentiation ad-HMSC cultured on 24-well plates. Osteogenic differentiation media was removed and cells washed using Ca^{2+}/Mg^{2+}-free DPBS (pH 7.4). DPBS was removed and cells were fixed by incubating for 30 minutes in 10 % (w/v) formalin. Formalin was removed and wells were washed using sterile ddH_2O after which fresh sterile ddH_2O was added and the plate incubated at room temperature for 5 minutes. Sterile ddH_2O was removed and Alizarin Red S solution (40 mM; pH 4.2) was added at room temperature for 20 minutes with gentle shaking. Alizarin Red S solution was removed and the wells were washed twice with sterile ddH_2O. Cells were viewed using a Zeiss AxioVert.A1 FL-LED Fluorescence Microscope at 200X magnification with a Ph 2 phase contrasting filter. Full colour images were captured using a Samsung Galaxy S4 smartphone at 218X magnification.

4.2.8 Protocol for Real Time Analysis using the xCELLigence system

The ACEA xCELLigence Real Time Cell Analyser (RTCA) Single Plate (SP) system was initialised, as per manufacturer's instructions, prior to commencement of the experiment. Complete MSCM (100 µL) was added to all 96 wells of the E-plate View 96. The plate was allowed to equilibrate at room temperature in a sterile field for 30 minutes. The plate was then placed into the single plate (SP) station cradle (housed in a humidified incubator at 37 ^{o}C, in a 5 % (v/v) CO_2 atmosphere) for a background reading to be established. Cells (ad-HMSC, P_6) were seeded at 5 000 cells/well in 25 µL aliquots. Cells were allowed to settle for 30 minutes outside

the incubator prior to returning the E-plate to the SP station. Growth was monitored by electrical impedance measurements using the xCELLigence RTCA SP system as arbitrary cell index (*CI*) units. The formula used for calculating *CI* is described in Equation 4.1 below.

$$\textbf{Cell Index } (\boldsymbol{CI}) = \frac{\boldsymbol{Zi - Zo}}{\mathbf{15}}$$

Equation 4.1: Arbitrary cell index (*CI*) calculated from changes in electrical impedance. Z_i: electrical impedance at given time points. Z_O: background reading.

Differentiation was induced by performing a full media change using 200 µL of the desired differentiation media 71 hours after cell seeding. Undifferentiated cells cultured in complete MSCM were used as controls. Plots represent the average change in *CI* for 12 identically treated culture wells. A graph was generated from a single experiment using GraphPad Prism (v7.02).

4.2.9 Sodium alginate hydrogel preparation and cell encapsulation

Alginic acid sodium salt (1 & 2 % w/v) was dissolved in sterile ddH_2O under constant stirring at 70 °C. For cell encapsulation experiments, ad-HMSC was cultured in complete α-MEM in 75 cm^2 cell culture flasks. Culturing of HUVEC was achieved using all-in-one ECGM, in 75 cm^2 cell culture flasks. Upon reaching confluency, cells were trypsinised using the standard subculturing protocol. Cell pellets were resuspended in separate gel solutions at densities of 1 x 10^6 cells/mL and transferred to 96-well plates. Resulting alginate gels were ionically crosslinked using sterile (autoclaved, 120 °C) calcium chloride solution ($CaCl_2$, 50 mM) for 2 minutes. Calcium chloride was removed and replaced with complete α-MEM for ad-HMSC encapsulated gels and ECGM for HUVEC encapsulated gels. Respective cell culture media was replaced every 3 days. Encapsulated alginate hydrogels were incubated in a humidified incubator at 37 °C, 5 % (v/v) CO_2 atmosphere. Cells were grown for 1 & 7 days, followed by live/dead cell staining and microscopy.

`

4.2.10 Live/dead cell staining

Encapsulated cell viability was determined by live/dead cell staining of cell-laden alginate gels. Cell culture media was removed and replaced with live/dead staining solution consisting of DMEM, 1 % (v/v) PSA, 19.2 μM fluorescein diacetate (FDA, Sigma Cat. No. F7378) and 30 μM propidium iodide (PI, Sigma Cat. No. P4170). Cells were incubated for 4 minutes in the dark, following removal of the staining solution. Gels were then rinsed with Ca^{2+}/Mg^{2+}-free DPBS (pH 7.4). Alginate gel discs were transferred to glass bottom culture dishes where Ca^{2+}/Mg^{2+}-free DPBS (pH 7.4) was added to prevent drying of the gels. Samples were analysed using a Zeiss LSM780 Laser Scanning Confocal Microscope at 100X magnification. Dead (red) cells were detected using the dsRed filter (563 nm/581 nm), whereas live (green) cells were detected using the FITC filter (495 nm/519 nm). On average, Z-stacked fluorescence micrographs consisted of 32 slices of which slices were captured at 30 μm intervals (960 μm Z-stack depth). Cell viability (%) was quantified (calculated) from 28 of the bottom-most live/dead staining images using Equation 4.2 below. Experiments were run in duplicate (n=2) wherein three images were captured at a time.

$$\boldsymbol{Cell\ Viability}\ (\%) = \frac{\boldsymbol{Total\ live\ (green)}}{\boldsymbol{Total\ live\ (green) + Total\ dead\ (red)}}\ \boldsymbol{x\ 100}$$

Equation 4.2: Cell viability (%) calculated from live/dead confocal images. Total live cells (green) was divided by the total live (green) & dead (red) cells, multiplied by 100.

4.2.11 WST-1 assay

Encapsulated cell viability was also determined through WST-1 cell proliferation assays. Cell cultures (ad-HMSC and HUVEC) were seeded separately in either 1 % or 2 % (w/v) sodium alginate gels at densities of 1 x 10^6 cells/mL, in 96-well plates. Cells were cultured in either complete α-MEM (for ad-HMSC cultures) or complete ECGM (for HUVEC cultures) (150 μL) for 48 hours in a humidified incubator at 37 ^{o}C, 5 % (v/v) CO_2 atmosphere. Media was replaced with complete α-MEM/ECGM and 10 μL/well Roche WST-1 cell proliferation reagent (Sigma,

`

Cat. No: 11644807001). Cells were then incubated for 4 hours at 37 ^{o}C, in a humidified 5 % (v/v) CO_2 atmosphere, following transferring WST-1 containing culture media to new 96-well plates. Absorbance readings were read using a SpectraMax M5 Microplate Reader at 450 nm. SoftMax Pro (v6) software was used for recording absorbance readings. Experiments were run in duplicate wherein eight identically treated wells were used for obtaining absorbance readings per experiment. Data sets were normalised about their respective means in GraphPad Prism (v7.02) software. Cell-free control samples containing alginate and culture media only were used as blank readings (cell-free absorbance readings were subtracted from values from cell-seeded absorbance readings).

4.3 Results & Discussion

4.3.1 Confirmation of adipose-derived Human Mesenchymal Stromal Stem Cell (ad-HMSC) differentiation potential

Multi-lineage differentiation potential of ad-HMSC was validated by analysing the osteogenic and adipogenic differentiation potential of ad-HMSC. Progressive lipid droplet accumulation was imaged when adipogenic-induced ad-HMSC (P_5) were viewed daily under bright field light microscopy for 6 days (Figure 4.1 A-F). Furthermore, intracytoplasmic lipid accumulation of ad-HMSC (P_5) was detected through Oil red O (Figure 4.2 B) and Nile red (Figure 4.2 D) staining of ad-HMSC induced for adipogenic differentiation for 9 days. Visualisation of osteogenic-induced ad-HMSC ECM mineral composition was achieved through Alizarin Red S staining (Figure 4.2 C). Cells were induced for osteogenic differentiation for 21 days. In addition to end-point staining, real-time analysis of cellular impedance changes were monitored using the xCELLigence RTCA SP system when ad-HMSC cultures were induced for adipogenic and osteogenic differentiation (Figure 4.3).

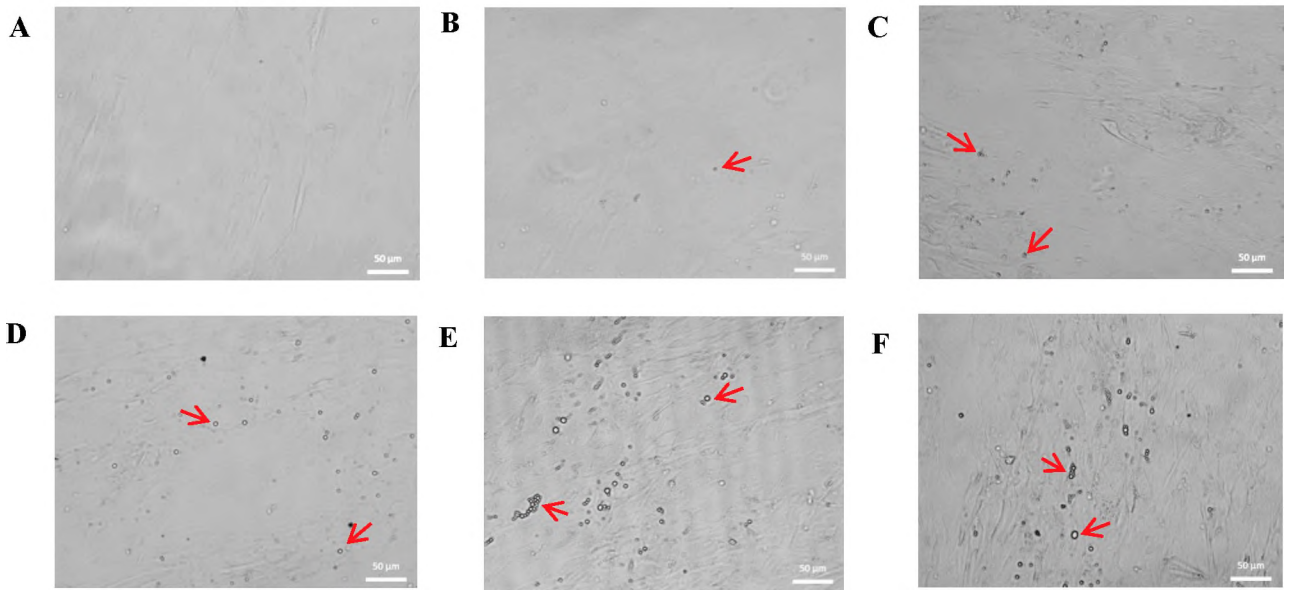

Figure 4.1: Morphological changes during adipogenesis. Confluent ad-HMSC (P_5) were induced for adipogenic differentiation for 5 days. A: Day 0. B: Day 1. C: Day 2. D: Day 3. E: Day 4. F: Day 5. Red arrows highlight areas of lipid accumulation. Scale bars represent 50 µm. Images were captured using a Zeiss Axio.Vert.A1 FL-LED Fluorescence Microscope at 200X magnification with a Ph 2 filter. Images representative of multiple images (n=3).

Adipogenic differentiation of ad-HMSC (P_5) revealed progressive lipid accumulation within the cytosol when adipogenic-induced ad-HMSC cultures were viewed daily under bright field light microscopy for 6 days (Figure 4.1 A-F). No lipid droplets appeared present prior to induction of differentiation (Figure 4.1. A), indicating that the culture was absent of adipocyte precursors and most likely consisted entirely of ad-HMSC in their self-renewing, multipotent state. Cells started showing clear lipid accumulation after 2 days of differentiation (Figure 4.1 C). Days 3, 4, and 5 show lipid accumulation uniformly increasing with the progression of adipogenic differentiation. Interestingly, lipid accumulation significantly increased at day 4 (Figure 4.3 D), one day following replacing adipogenic induction media with adipogenic maintenance media (insulin supplemented).

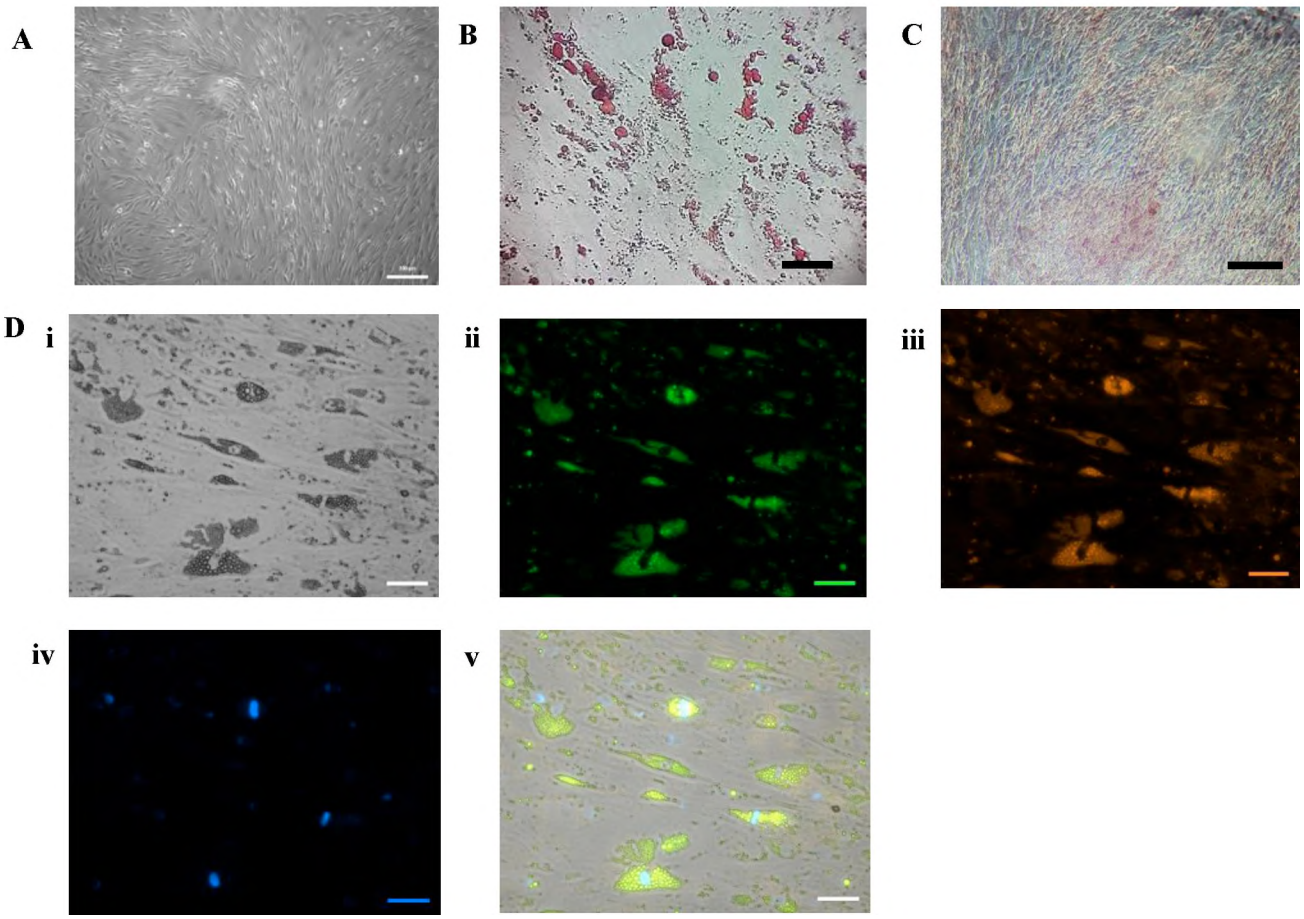

Figure 4.2: ad-HMSC differentiation potential. A: Self-renewing ad-HMSC (P_4) (scale bar represents 200 µm). B: Oil Red O staining of ad-HMSC (P_5) treated with adipogenic differentiation media for 9 days (scale bar represents 50 µm). C: Alizarin Red S staining of ad-HMSC (P_4) treated with osteogenic differentiation media for 21 days (scale bar represents 200 µm). D: Nile red staining of ad-HMSC (P_5) induced for adipogenic differentiation for 9 days. i) Bright field, ii) Neutral lipids, iii) Polar lipids, iv) Hoescht nuclear stain, v) Merge. Scale bars represent 50 µm. Cells were viewed using a Zeiss Axio.Vert.A1 FL-LED Fluorescence Microscope with a Ph 2 filter.

`

Oil Red O staining (Figure 4.2 B) allowed for clear visualisation of intracytoplasmic lipids due to the retention of the dye. Nile red staining further confirmed the presence of intracytoplasmic lipids when analysing cells with fluorescence microscopy (Figure 4.2 D). Large amounts of both neutral (Figure 4.2 D i) and polar (Figure 4.2 D ii) lipids were present. Osteogenic differentiation was detected through Alizarin Red S staining (Figure 4.2 C). Calcium deposits within the ECM retained the Alizarin Red S stain and allowed for clear visualisation of the ECM through bright field microscopy. Control (non-differentiating) samples were unfortunately not stained using Oil Red O, Nile Red, nor Alizarin Red S in the present study. While differentiated cell cultures produced staining results in-line with that of literature (Barry & Murphy, 2003; Angstmann *et al.*, 2011; Bagnaninchi & Drummond, 2011), control samples would have further confirmed lineage specific differentiation by confirming that non-induced cultures comprised solely of ad-HMSC in their multipotent, undifferentiated state.

Real-time analysis of cellular impedance changes was monitored using the ACEA xCELLigence RTCA SP system when ad-HMSC (P_6) were seeded for 71 hours and subsequently induced for either adipogenic (Figure 4.3 green curve) or osteogenic (Figure 4.3 orange curve) differentiation. Impedance curves revealed clear differences in *CI* profiles between differentiating cultures as well as non-induced MSCM (Figure 4.3 red curve) or DMEM (Figure 4.3 blue curve) controls. Both adipogenic and osteogenic differentiation media was made up in DMEM, resulting in the drop in *CI* observed when the full media change was performed (Figure 4.3 purple arrow). Compared to untreated control samples (MSCM only), osteogenic-induced cultures produced relatively high *CI* values soon after the induction of differentiation. A clear increase in *CI* is observed throughout the progression of osteogenic differentiation. Contrastingly, adipogenic-induced cultures produced *CI* values below that of MSCM controls up until the 140 hour mark (Figure 4.3 black arrow), when the average *CI* values for adipogenic-induced ad-HMSC cultures was roughly the same as that of MSCM control cultures.

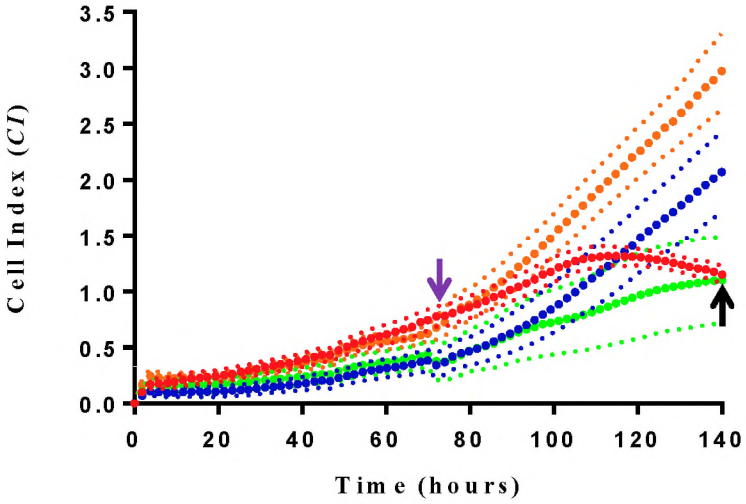

Figure 4.3: Cell Index curves of ad-HMSC (P_6) differentiation. Cells were treated with MSCM for 71 hours prior to treating cells at the same time with MSCM (red), DMEM (blue), AIM (green) and ODM (orange). Cell Index curves were plotted as an average of 12 identically treated culture wells. Dotted lines represent standard deviation. Data was plotted using GraphPad Prism (v7.02). (n=1)

When grown in monolayer, self-renewing (non-differentiating) ad-HMSC display fusiform (spindle-shaped) morphologies (Figure 4.2 A). Their shape and size similarly represent those of fibroblasts. Hence their morphology is commonly referred to as "fibroblastic" (Barry and Murphy, 2004). Differentiation of ad-HMSC induces several phenotypical changes associated with the commitment to a differentiation lineage. Adipogenic differentiation involves the progressive biosynthesis and accumulation of intracytoplasmic lipid droplets (termed lipogenesis), inducing a drastic change in cellular morphology. The accumulation of several lipid vacuoles changes the cells from the self-renewing, spindle-shaped, morphology to that of a rounder, sphere-like shape (Reitinger *et al.*, 2012). Intracytoplasmic lipid content is commonly detected through cell staining techniques such as Oil red O staining or fluorescence Nile red staining. Detection of lipid accumulation in adipogenic-induced ad-HMSC cultures allowed for the conformation that ad-HMSC were indeed able to differentiate along the adipogenic lineage as expected. In terms of osteogenic differentiation, commitment toward the osteogenic lineage involves the rapid production of mineralised ECM components including the deposition of calcified precipitates within the ECM (Reitinger *et al.*, 2012). The mineralised calcified matrix is accurately assessed through direct visualisation of the ECM using Alizarin Red S staining

`

solution (Bunnell *et al.*, 2008). End-point cell staining revealed that the ad-HMSC culture used in the study were able to differentiate along both adipogenic and osteogenic lineages. This was further confirmed when ad-HMSC were subject to differentiation and cellular impedance sensing using the ACEA xCELLigence RTCA SP system. Similar trends in impedance profiles were observed in Angstmann *et al.* (2011) and Bagnaninchi & Drummond (2011), where bone-marrow derived mesenchymal stromal cells (bm-MSC) and ad-SC, respectively, were differentiated along the adipogenic and osteogenic differentiation lineages. When induced for osteogenic differentiation, cells produced impedance profiles significantly higher than that of adipogenic-induced cells cultures, similar to that observed in the present study. While adipogenic differentiation involves the accumulation of intracytoplasmic lipids, affecting overall cellular morphologies. The adipogenic-induced change in cell morphologies from spindle-shaped cells to a more sphere-like phenotype results in loosening of cell–substrate attachments (Reitinger *et al.*, 2012). The increase in space between cells may account for the decrease in resistance to impedance-measuring sensing electrodes when ad-HMSC were induced for adipogenic differentiation (Figure 4.3 green curve). Contrastingly, due to the formation of a highly calcified ECM, osteogenic-differentiating cells grow buried within matrix deposits, forming tight junctions between cells (Angstmann *et al.*, 2011). Furthermore, osteogenic differentiation induces cells to proliferate rapidly as well as grow in colonies (Bunnell *et al.*, 2008). This may explain the observed increase in *CI* (Figure 4.3 orange curve), as *CI* readings reflect cellular proliferation and adhesion. It has also been reported in Reitinger *et al.* (2012) that sharp increases in cellular impedance may be due to sensing electrodes being affected by newly deposited matrix materials. Electrodes are believed to absorb the matrix to a greater extent compared to the glass between individual electrodes.

4.3.2 Adipose-derived Human Mesenchymal Stromal Stem Cell (ad-HMSC) and Human Umbilical Vein Endothelial Cell (HUVEC) encapsulation within sodium alginate hydrogels

Cell viability of ad-HMSC (P_5) and HUVEC (P_3) encapsulated within 1 & 2 % (w/v) sodium alginate gels were analysed through live/dead staining on both Day 1 & Day 7 cultures (Figure 4.4 – Figure 4.13). Live/dead staining was performed using FDA (green) live stain and PI (red) dead stain. Three-dimensional images of gel slices roughly 960 μm in thickness (30 μm slice intervals) were taken using a Zeiss LSM780 Laser Scanning Confocal Microscope.

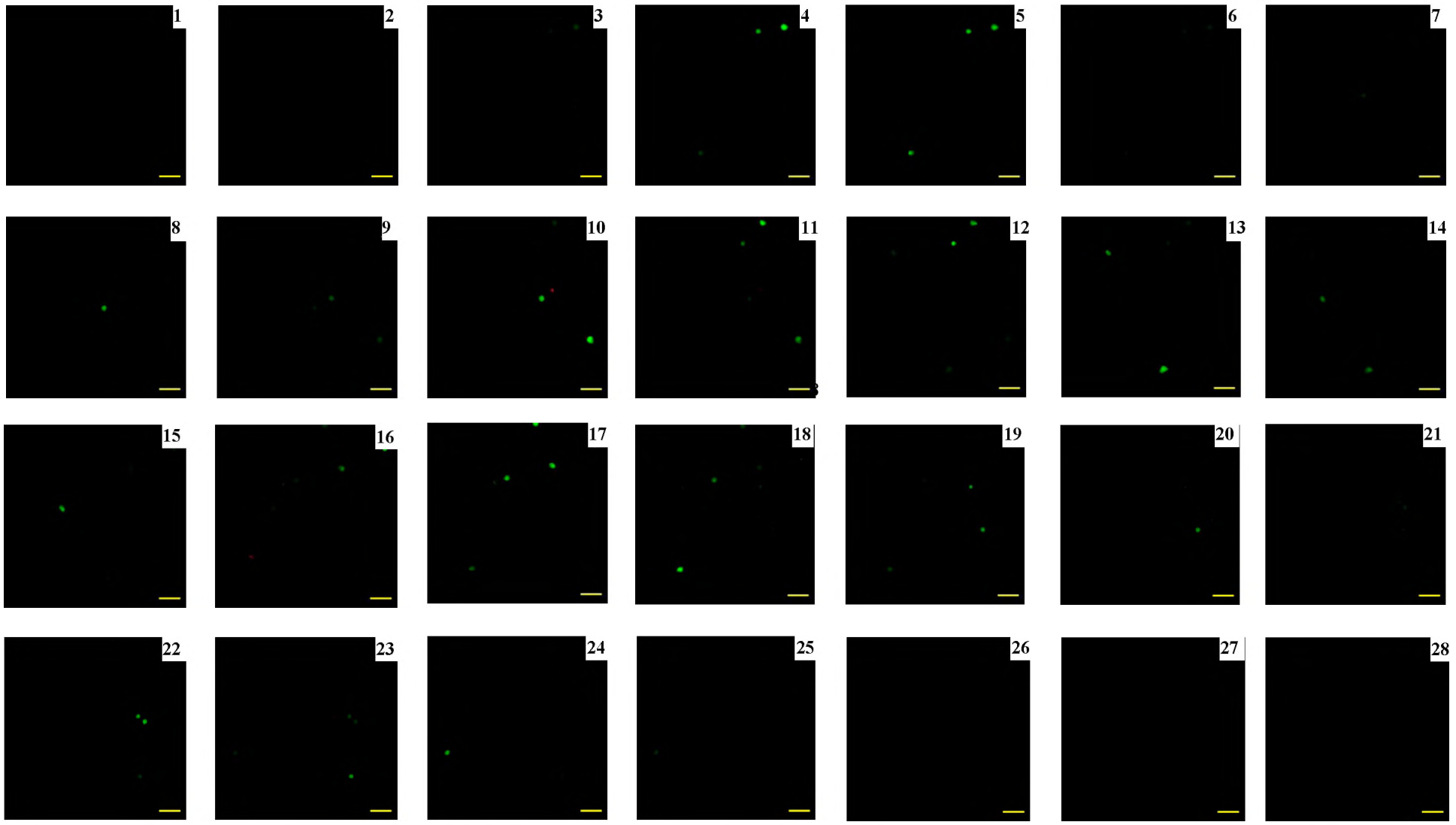

Figure 4.4: Day 1 live/dead staining of ad-HMSC (P_5) encapsulated in sodium alginate (1 % w/v). Images were captured using a Zeiss LSM780 Laser Scanning Confocal Microscope at 100X magnification. Images represent fluorescence micrographs from the bottom of the gel (1) to the top of the gel (28) at 30 μm intervals. Scale bars represent 100 μm. Images representative of multiple images (n=2).

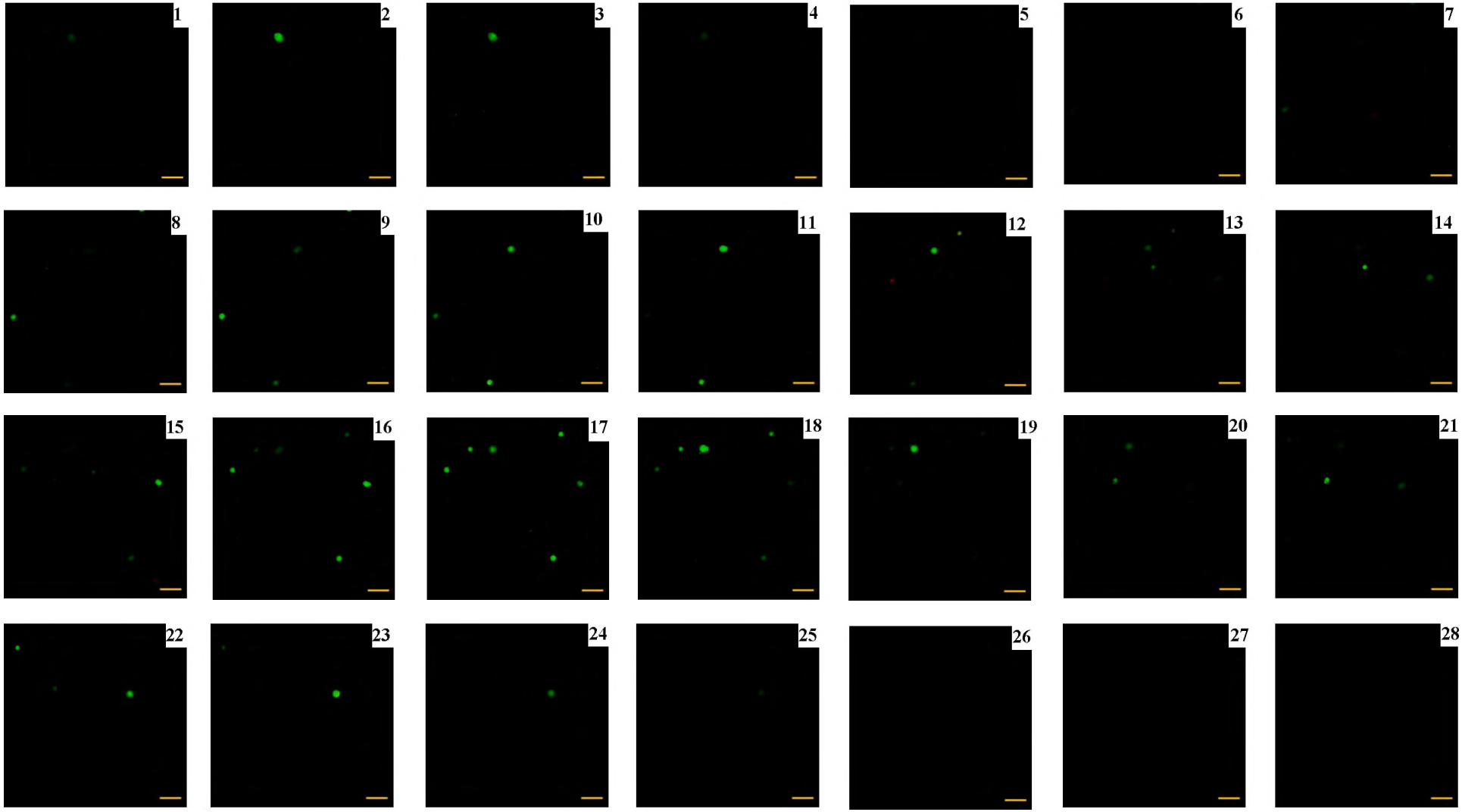

Figure 4.5: Day 7 live/dead staining of ad-HMSC (P_5) encapsulated in sodium alginate (1 % w/v). Images were captured using a Zeiss LSM780 Laser Scanning Confocal Microscope at 100X magnification. Images represent fluorescence micrographs from the bottom of the gel (1) to the top of the gel (28) at 30 µm intervals. Scale bars represent 100 µm. Images representative of multiple images (n=2).

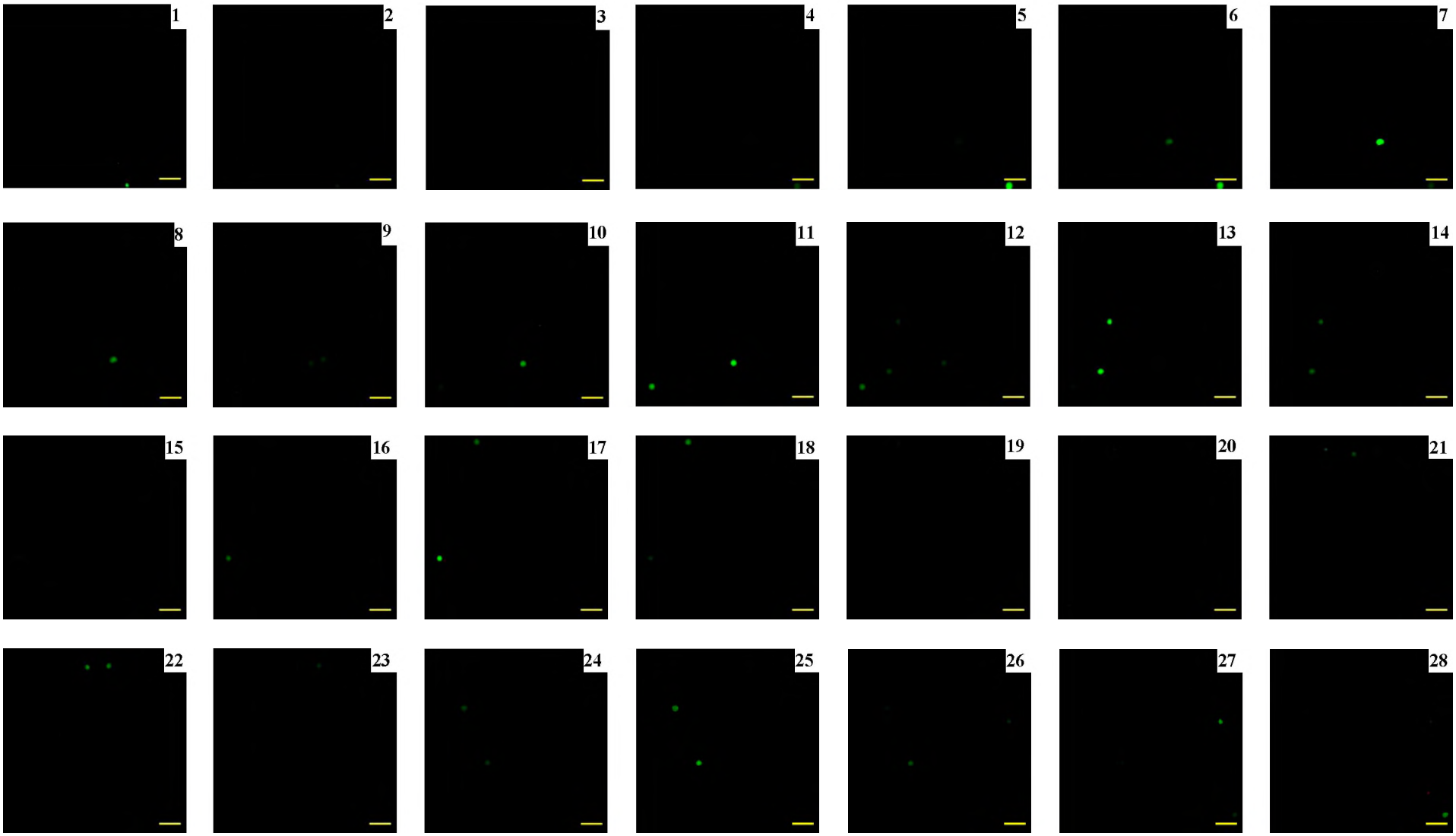

Figure 4.6: Day 1 live/dead staining of ad-HMSC (P_5) encapsulated in sodium alginate (2 % w/v). Images were captured using a Zeiss LSM780 Laser Scanning Confocal Microscope at 100X magnification. Images represent fluorescence micrographs from the bottom of the gel (1) to the top of the gel (28) at 30 µm intervals. Scale bars represent 100 µm. Images representative of multiple images (n=2).

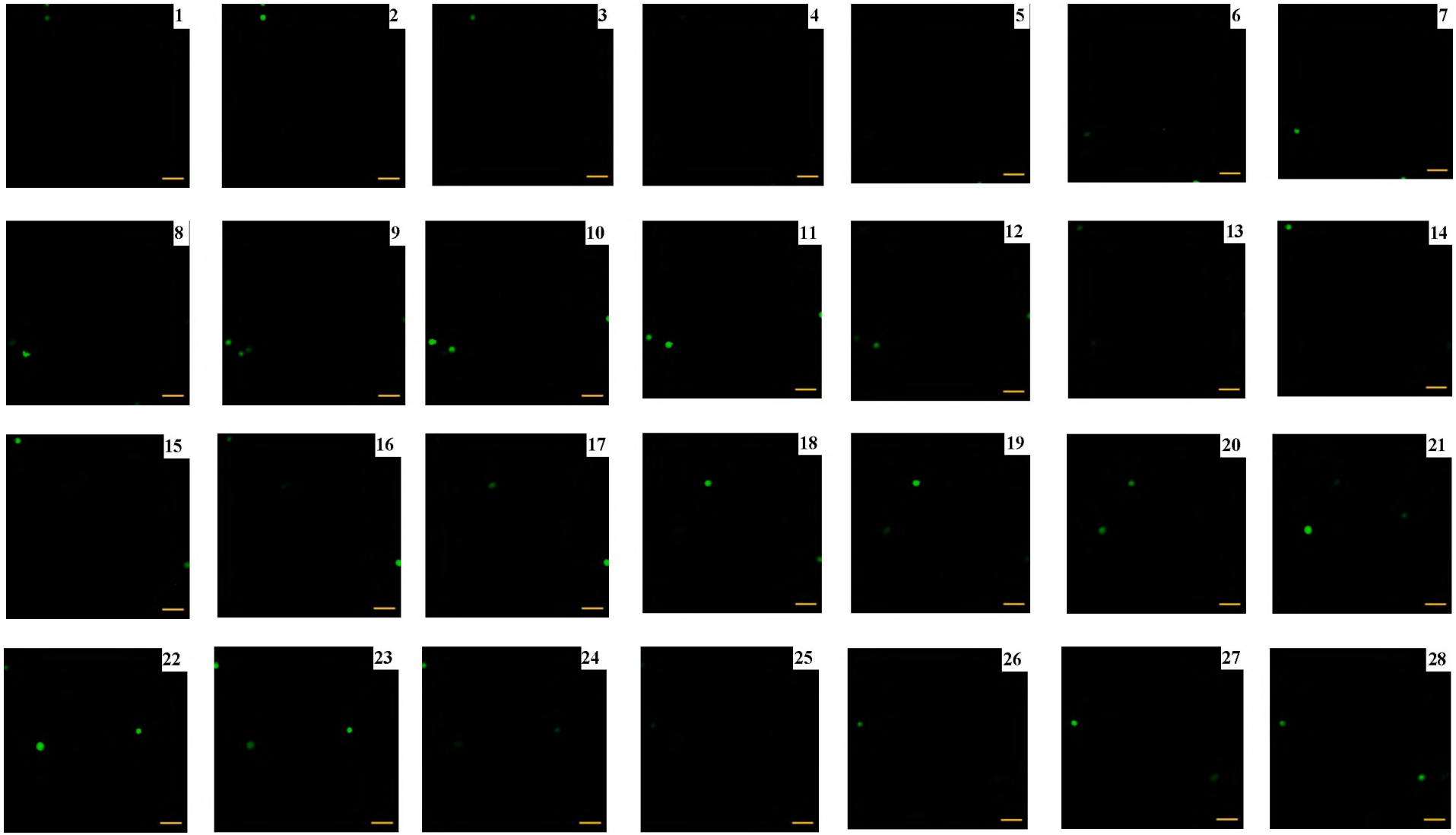

Figure 4.7: Day 7 live/dead staining of ad-HMSC (P_5) encapsulated in sodium alginate (2 % w/v). Images were captured using a Zeiss LSM780 Laser Scanning Confocal Microscope at 100X magnification. Images represent fluorescence micrographs from the bottom of the gel (1) to the top of the gel (28) at 30 µm intervals. Scale bars represent 100 µm. Images representative of multiple images (n=2).

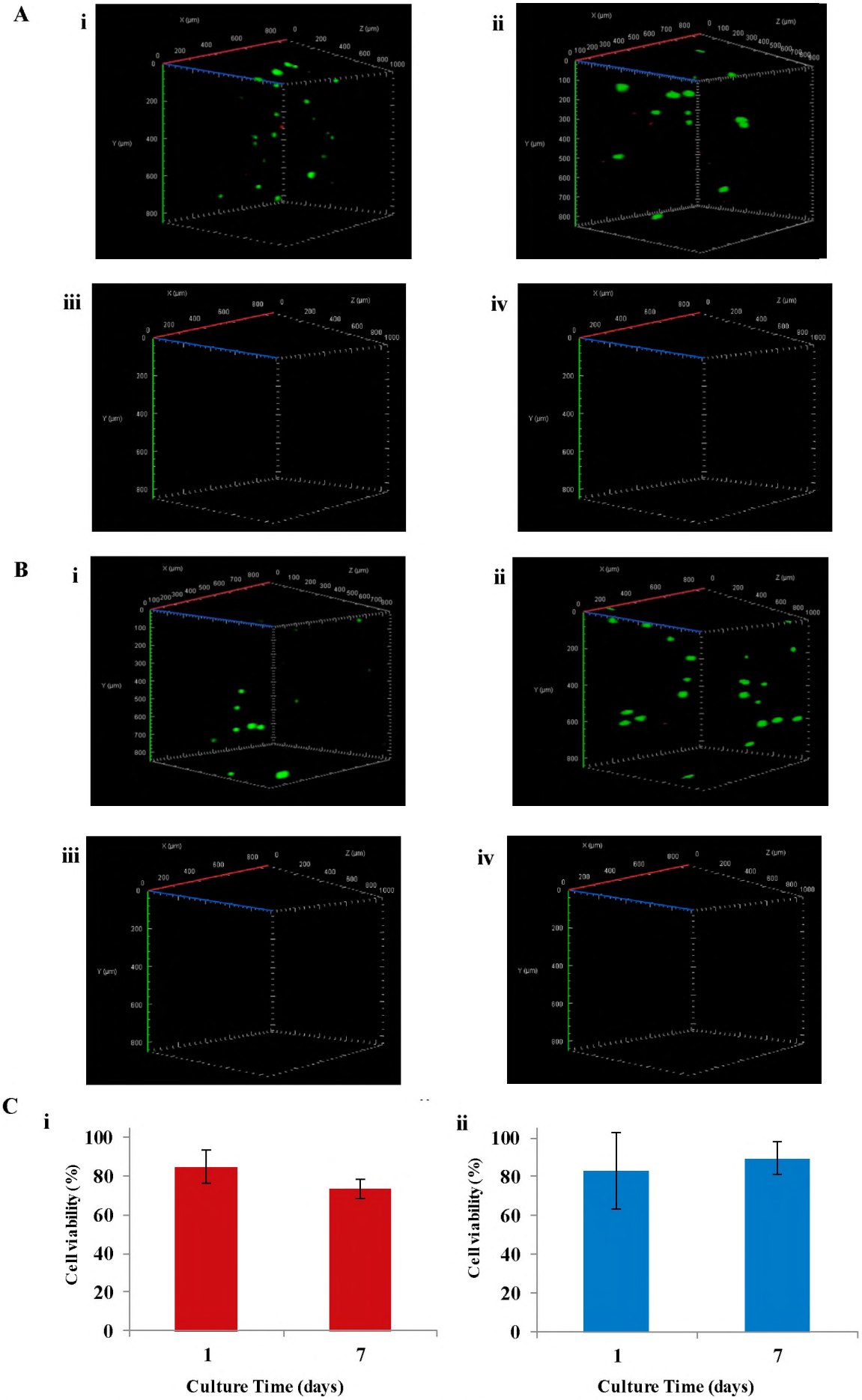

Figure 4.8: Live/dead assay for encapsulated ad-HMSC (P_5) within sodium alginate hydrogels. A: 1 % (w/v) alginate. i) Day 1, ii) Day 7, iii) Day 1 cell-free control, iv) Day 7 cell-free control. B: 2 % (w/v) alginate. i) Day 1, ii) Day 7, iii) Day 1 cell-free control, iv) Day 7 cell-free control. Cartesian axes represented by the red (X), green (Y) and blue (Z) lines. Images were captured using a Zeiss LSM780 Laser Scanning Confocal Microscope at 100X magnification. Images representative of multiple (3) images. C: Cell viability calculated from three live/dead images. i) 1 % (w/v) alginate, ii) 2 % (w/v) alginate. Error bars represent standard deviation. Results are representative of 2 independent experiments (n=2).

Live/dead staining revealed ad-HMSC to be viable at both Day 1 (Figure 4.4) & Day 7 (Figure 4.5), when encapsulated in 1 % (w/v) sodium alginate gels. Day 1 live/dead staining revealed large amounts of viable cells present in the middle of the gel (Figure 4.4 (4-24)). A similar result was observed at Day 7 (Figure 4.5 (2-24). When encapsulated in 2 % (w/v) sodium alginate, ad-HMSC was revealed to be viable at both Day 1 (Figure 4.6) as well as Day 7 (Figure 4.7). Interestingly, unlike the images obtained from 1 % (w/v) alginate encapsulation, 2 % (w/v) alginate encapsulation revealed cell distribution throughout the entirety of gels at both Day 1 and Day 7. Most likely as a result of increased gel elasticity (stiffness) in 2 % (w/v) alginate compared to that 1 % (w/v) alginate, ad-HMSC were encapsulated to a greater degree within 2 % (w/v) gels. Three-dimensional images of the entire Z-stacks are presented in Figure 4.8 (A i-iv, B i-iv). Encapsulated ad-HMSC in 2 % (w/v) alginate gels were relatively grouped at Day 1 (Figure 4.8 B i). However, at Day 7 (Figure 4.8 B ii) cells were more evenly distributed throughout the entirety of the gel. Encapsulating ad-HMSC in 1 and 2 % (w/v) alginate resulted in cells retaining spherical morphologies. As a result of limited cell attachment and integrin binding, a low amount of cell spreading was observed even after 7 days of culture. Cell-free (control) samples, containing 1 or 2 % (w/v) alginate only, revealed no live or dead cells at either Day 1 (Figure 4.8 A iii, Figure 4.8 B iii) or Day 7 (Figure 4.8 A iv, Figure 4.8 B iv). Cell viability (%) was calculated from three live/dead staining images per experiment (experiments were run in duplicate) using Equation 4.2 (Figure 4.8 C i-ii). Encapsulated ad-HMSC cell viability was calculated as 84.5 % at Day 1 and 73.4 % at Day 7 when cells were encapsulated in 1 % (w/v) alginate hydrogels (Figure 4.8 C i). Whereas cell viability of ad-HMSC encapsulated in 2 % (w/v) alginate was calculated as 82.9 % at Day 1 and 89.4 % at Day 7 (Figure 4.8 C ii).

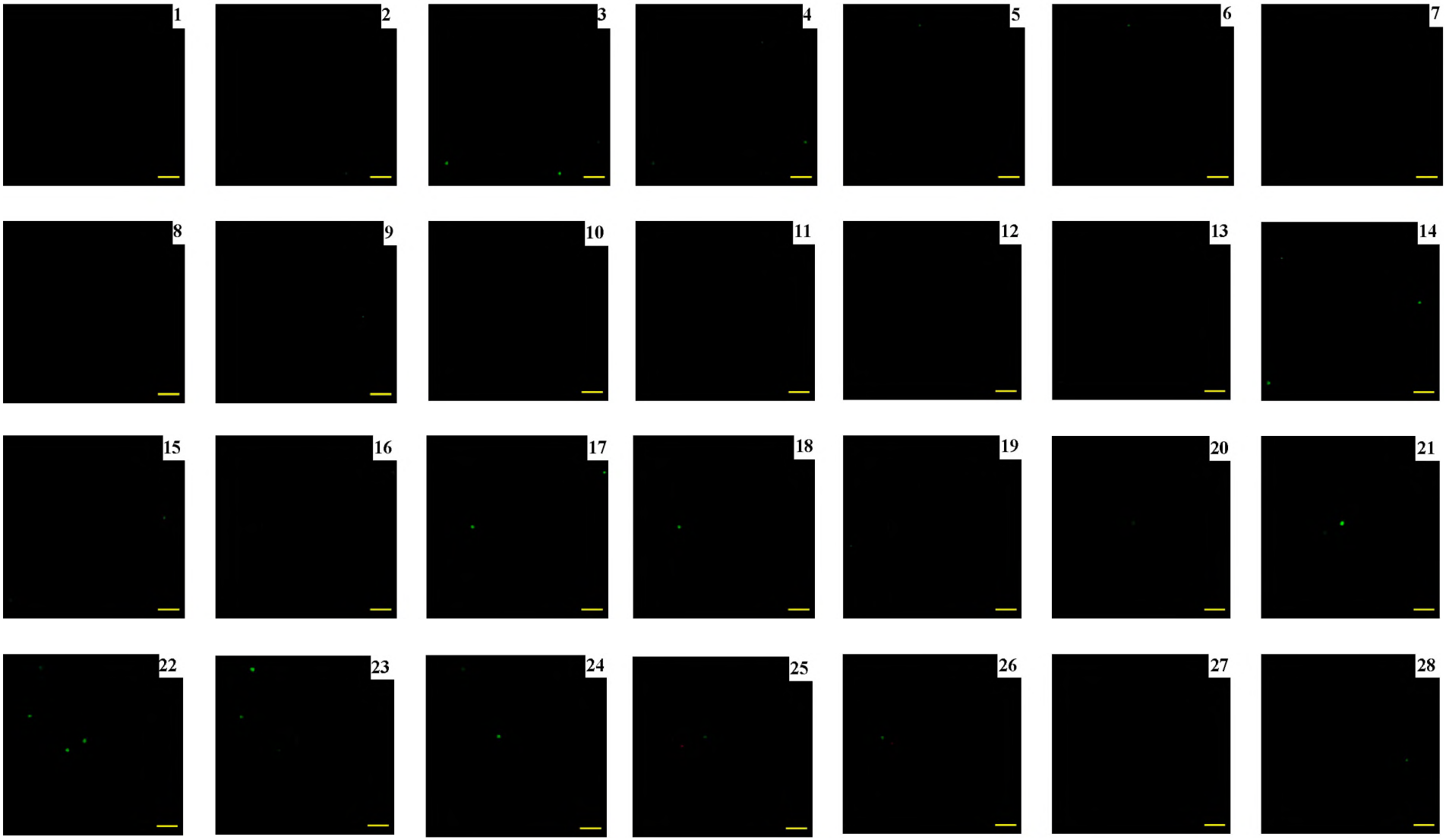

Figure 4.9: Day 1 live/dead staining of HUVEC (P_3) encapsulated in sodium alginate (1 % w/v). Images were captured using a Zeiss LSM780 Laser Scanning Confocal Microscope at 100X magnification. Scale bars represent 100 µm. Images represent fluorescence micrographs from the bottom of the gel (1) to the top of the gel (28) at 30 µm intervals. Images representative of multiple images (n=2).

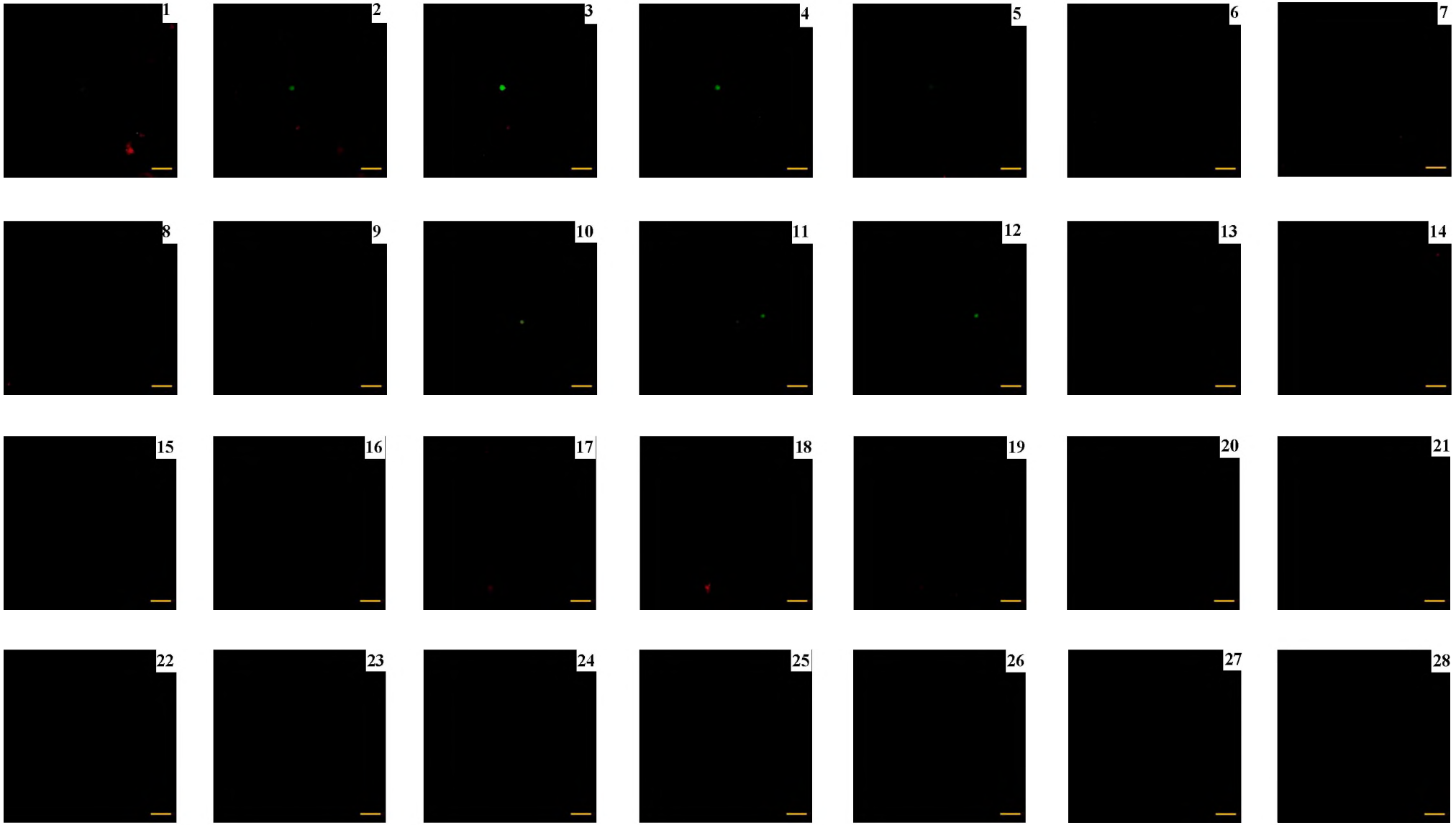

Figure 4.10: Day 7 live/dead staining of HUVEC (P_3) encapsulated in sodium alginate (1 % w/v). Images were captured using a Zeiss LSM780 Laser Scanning Confocal Microscope at 100X magnification. Scale bars represent 100 μm. Images represent fluorescence micrographs from the bottom of the gel (1) to the top of the gel (28) at 30 μm intervals. Images representative of multiple images (n=2).

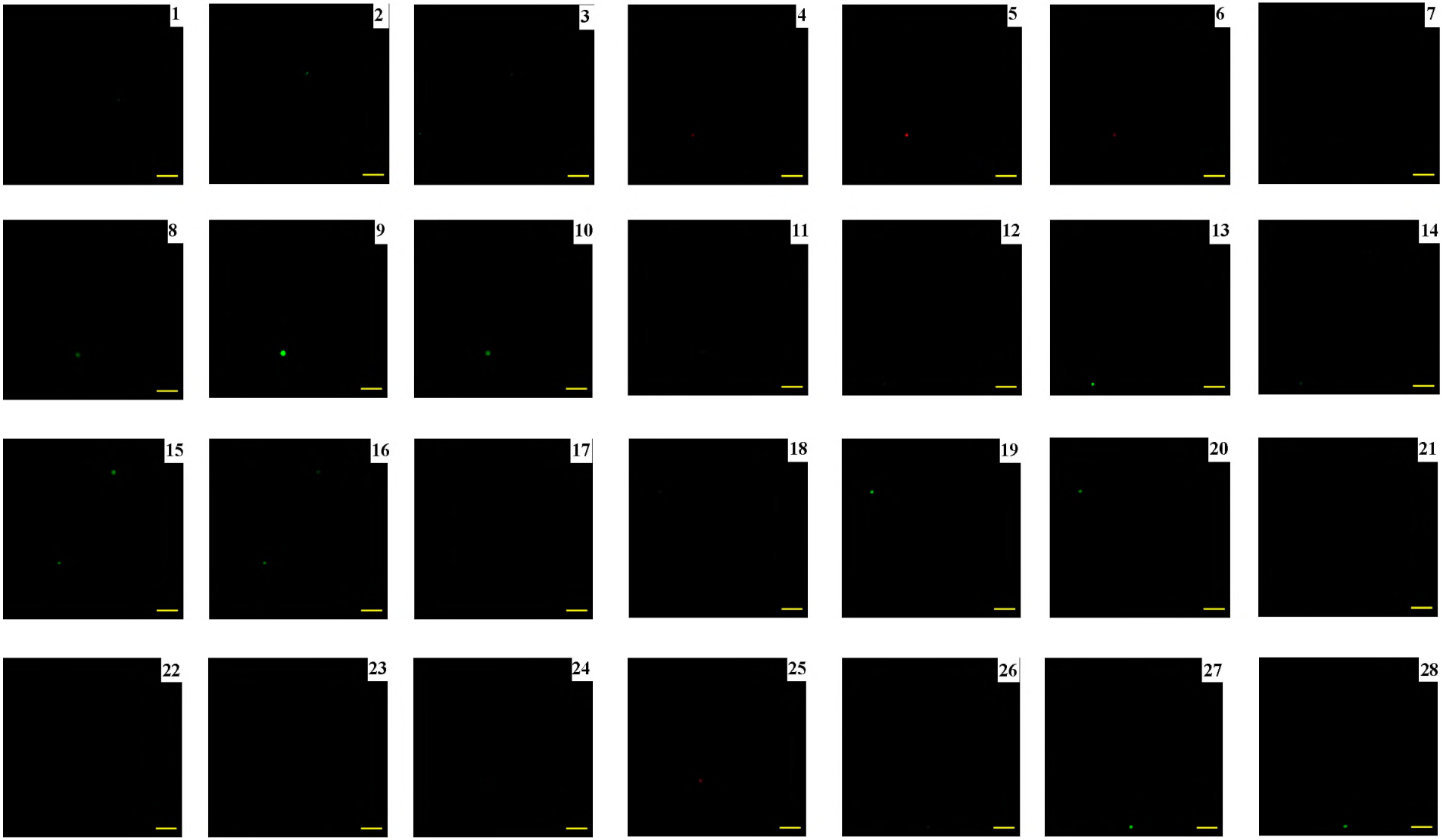

Figure 4.11: Day 1 live/dead staining of HUVEC (P_3) encapsulated in sodium alginate (2 % w/v). Images were captured using a Zeiss LSM780 Laser Scanning Confocal Microscope at 100X magnification. Scale bars represent 100 µm. Images represent fluorescence micrographs from the bottom of the gel (1) to the top of the gel (28) at 30 µm intervals. Images representative of multiple images (n=2).

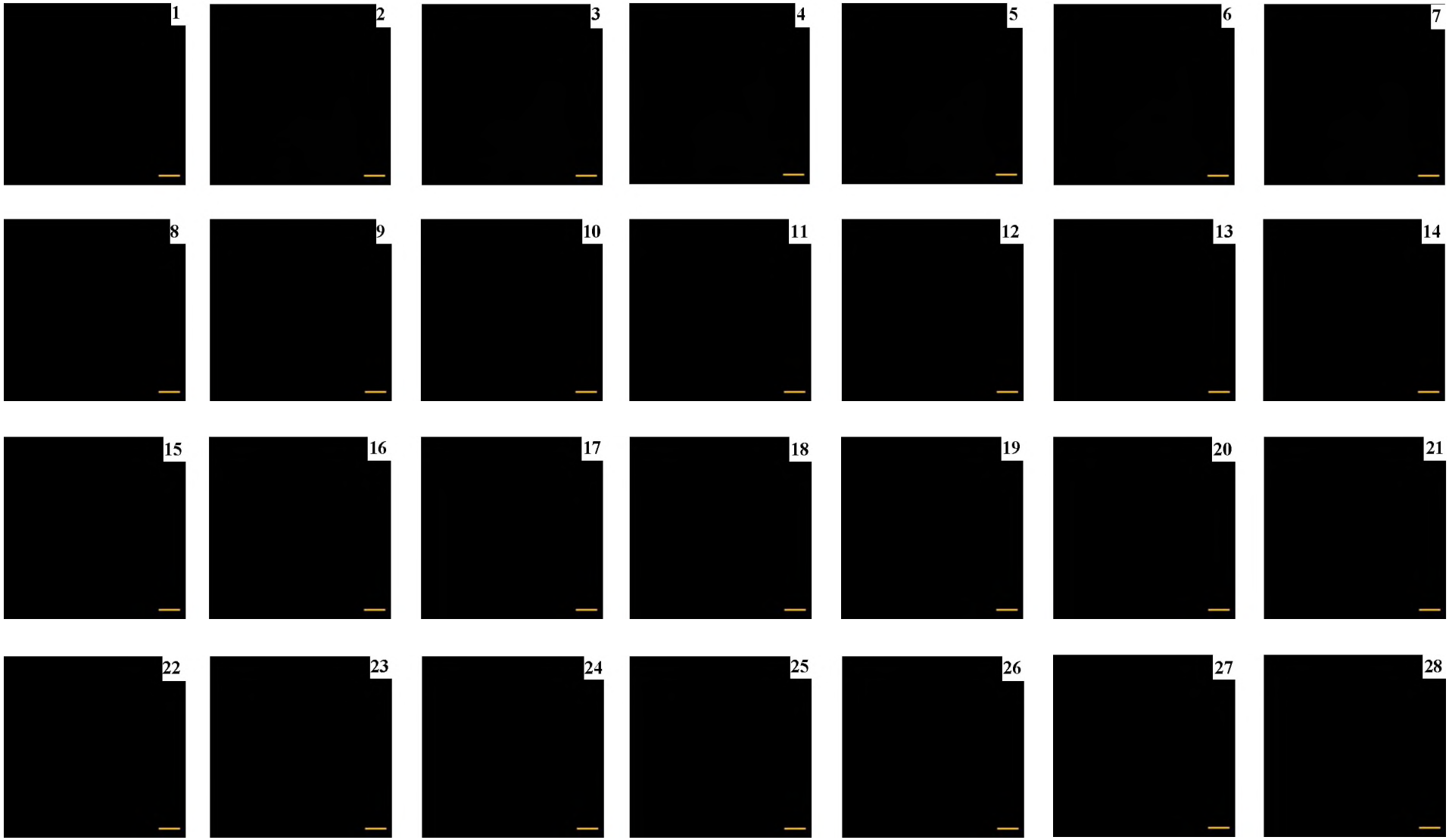

Figure 4.12: Day 7 live/dead staining of HUVEC (P_3) encapsulated in sodium alginate (2 % w/v). Images were captured using a Zeiss LSM780 Laser Scanning Confocal Microscope at 100X magnification. Scale bars represent 100 μm. Images represent fluorescence micrographs from the bottom of the gel (1) to the top of the gel (28) at 30 μm intervals. Images representative of multiple images (n=2).

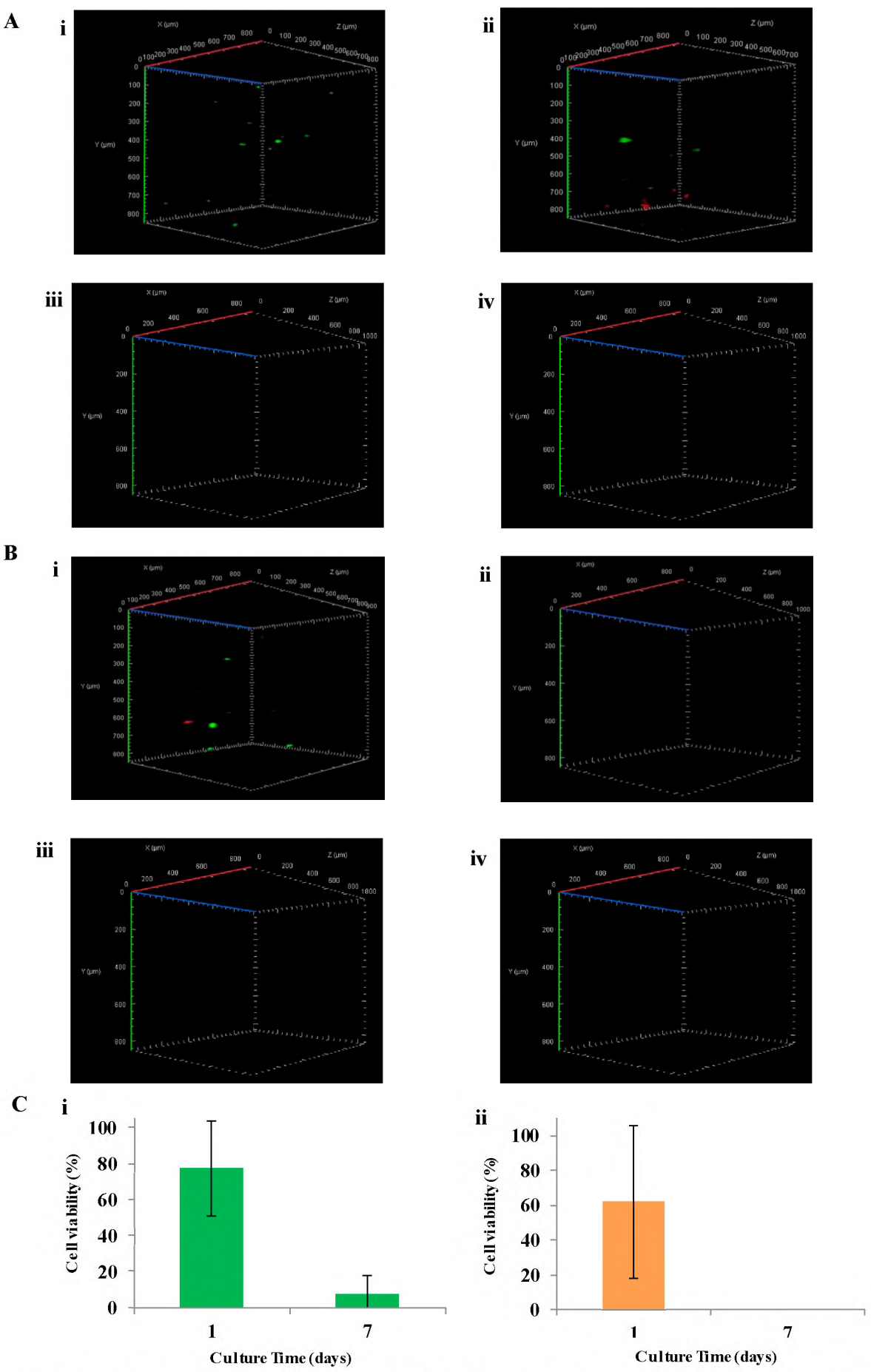

Figure 4.13: Live/dead assay for encapsulated HUVEC (P_3) within sodium alginate hydrogels. A: 1 % (w/v) alginate. i) Day 1, ii) Day 7, iii) Day 1 cell-free control, iv) Day 7 cell-free control. B: 2 % (w/v) alginate. i) Day 1, ii) Day 7, iii) Day 1 cell-free control, iv) Day 7 cell-free control. Cartesian axes represented by the red (X), green (Y) and blue (Z) lines. Images were captured using a Zeiss LSM780 Laser Scanning Confocal Microscope at 100X magnification. Images representative of multiple (3) images. C: Cell viability calculated from three live/dead images per experiment. i) 1 % (w/v) alginate, ii) 2 % (w/v) alginate. Error bars represent standard deviation. Results are representative of two independent experiments (n=2).

`

Live/dead staining revealed HUVEC encapsulation in 1 % (w/v) sodium alginate to be viable at Day 1 (Figure 4.9) and Day 7 (Figure 4.10). Similar to 1 % (w/v) ad-HMSC encapsulation at Day 1 (Figure 4.4), HUVEC encapsulated in 1 % (w/v) alginate at Day 1 revealed far more viable cells present in the middle of the gel section when compared to the top or bottom of the gel (Figure 4.9 (14-24)). However, at Day 7, viable cells were present only toward the bottom the gel (Figure 4.10 (2-12)), although overall cell viability was relatively low. No live cells were revealed to be present above slice number 12 (Figure 4.10). When encapsulated in 2 % (w/v) alginate, HUVEC was revealed to only be viable at Day 1 (Figure 4.11). Similar to that of 1 % (w/v) encapsulation, encapsulated HUVEC in 2 % (w/v) alginate at Day 1 also revealed large amounts of viable cells within the middle of the gel section when compared to the top or bottom of the gel (Figure 4.11 (8-20)). Dead (red) cells were only present near the bottom (Figure 4.11 (5)) and top (Figure 4.11 (25)) of the gel. Encapsulated HUVEC in 2 % (w/v) alginate at Day 7 consistently revealed no viable cells (Figure 4.12). Most likely as a result of a complete lack of cell attachment to the unmodified alginate hydrogels, neither live nor dead cells were detected. Three-dimensional images of entire Z-stacks are presented in Figure 4.13 (A i-iv, B i-iv). Similar to ad-HMSC encapsulation, encapsulated HUVEC cultures maintained spherical morphologies. Cell viability (%) was calculated from three live/dead staining images per experiment (experiments were run in duplicate) using Equation 4.2 (Figure 4.13 C i-ii). Encapsulated HUVEC cell viability was calculated as 77.1 % at Day 1 and 7.5 % at Day 7 when cells were encapsulated in 1 % (w/v) alginate hydrogels (Figure 4.13 C i). Whereas cell viability of HUVEC encapsulated in 2 % (w/v) alginate was calculated as 62.0 % at Day 1 and 0 % at Day 7 (Figure 4.8 C ii).

Cell viability of ad-HMSC (P_6) and HUVEC (P_3) was later assessed via WST-1 assays of ad-HMSC (P_6) and HUVEC (P_3) encapsulated 1 & 2 % (w/v) sodium alginate gels (Figure 4.14). Cell types were individually seeded at densities of 1 x 10^6 cells/mL and analysed 48 hours following cell seeding.

Average absorbance values of ad-HMSC revealed to be greater when cells were seeded in 2 % (w/v) (0.43; Figure 4.14 A green) compared to 1 % (w/v) (0.35; Figure 4.14 A blue) sodium alginate hydrogels. Contrastingly, average absorbance values of HUVEC revealed to be greater when cells were seeded in 1 % (w/v) (0.43; Figure 4.14 B red) compared to 2 % (w/v) (0.26; Figure 4.14 purple) sodium alginate hydrogels. Standard deviations were revealed to be relatively high for all treatments.

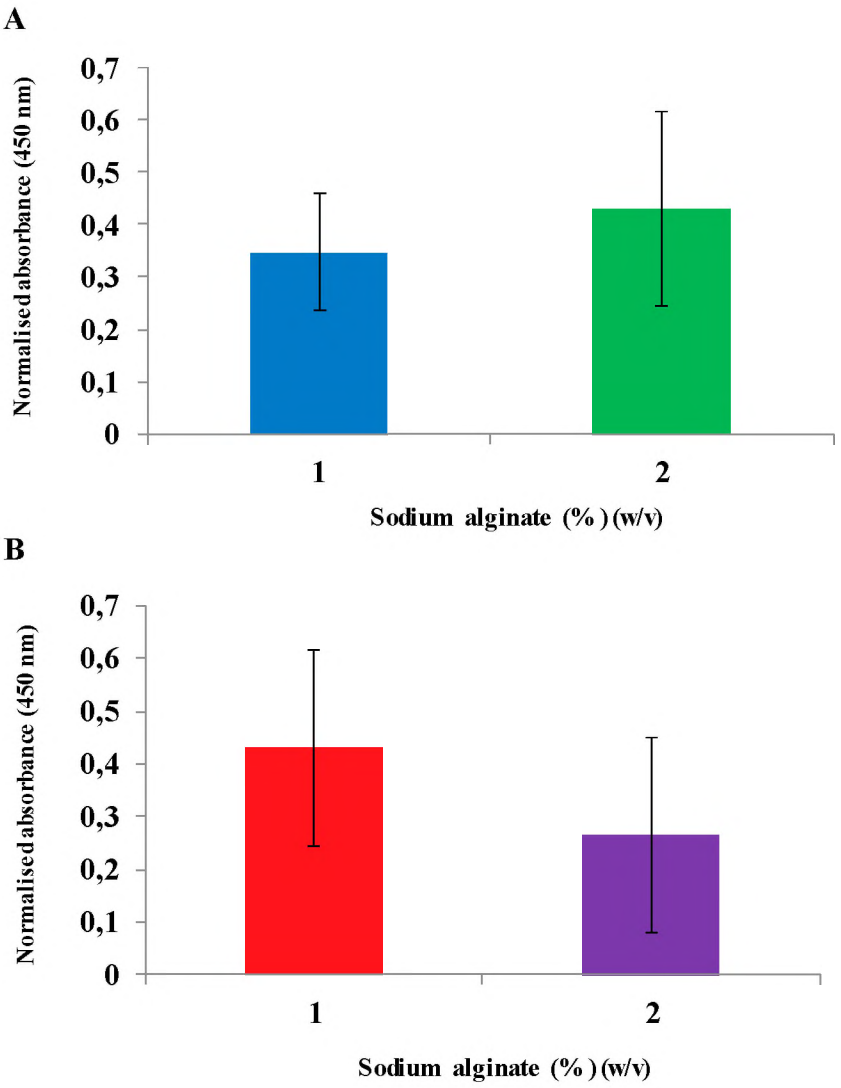

Figure 4.14: WST-1 assay of ad-HMSC (P_6) and HUVEC (P_3) encapsulated in sodium alginate hydrogels (1 & 2 % w/v). A: ad-HMSC encapsulation. B: HUVEC encapsulation. Normalised absorbance readings reflect an average of eight identically treated culture wells from duplicate experiments. Error bars represent standard deviation. (n=2)

Alginate hydrogels have been extensively used for cell encapsulation, transplantation and tissue engineering (Rowley *et al.*, 1999). In the present study, both 1 & 2 % (w/v) alginate encapsulated with ad-HMSC showed a high degree of cell viability at both Day 1 & Day 7 (Figure 4.4 – Figure 4.8). Cells encapsulated in 1 % (w/v) alginate showed a slight decrease in calculated cell viability after 6 days of culture when analysed by live/dead staining (Figure 4.8 C i). Contrastingly, encapsulated 2 % (w/v) alginate showed a slight increase in calculated cell viability (Figure 4.8 C ii). Live/dead staining also revealed that at Day 1 and at Day 7, ad-HMSC cell cultures retained spherical morphologies as opposed to the traditional "spindle-shaped", fusiform morphology observed when culturing ad-HMSC on 2D substrates such as glass or plastic (Seebach *et al.*, 2010).

`

Most likely as a result of alginate pore sizes having smaller diameters compared to ad-HMSC cellular bodies, cells were entrapped and forced to adapt to a round shape. A similar result was noted in Re'em *et al.* (2010), when chondrogenic-induced human bm-MSC were observed to grow in spherical clusters on unmodified alginate hydrogels. Furthermore, a dissertation submitted by Lourenço (2011) found that culturing of human MSC in unmodified alginate hydrogels resulted in the formation of cellular aggregates which were easily displaced and washed away due to the inability cells had for adhering to unmodified alginate. While encapsulated ad-HMSC analysed in this study were able to display viability up to Day 7, HUVEC cultures analysed were not nearly as viable when analysed after the same culture time.

Encapsulated HUVEC cells within 1 & 2 % (w/v) alginate hydrogels revealed limited cell viability at Day 1 (Figure 4.9, Figure 4.11). However, Day 7 live/dead staining revealed drastic decreases in cell viability for both alginate concentrations (Figure 4.10, Figure 4.12). Live/dead staining revealed culturing HUVEC in 1 % (w/v) alginate produced slightly higher calculated cell viability when compared to 2 % (w/v) alginate cell cultures (Figure 4.13 C i-ii). Similar to ad-HMSC encapsulation, HUVEC cultures displayed spherical morphologies at both Day 1 and Day 7. When grown on glass or plastic 2D substrates, HUVEC cultures grow in "cobblestone" morphologies (Cao & Lin, 2006). However, much like that of ad-HMSC alginate encapsulation, alginate pore sizes were most likely smaller than that of HUVEC cellular bodies. Cells were therefore forced to adapt a spherical-type of morphology. Similar HUVEC cell viability values calculated in the present study were reported in Bidarra *et al.* (2011). The group found that after 24 hours of HUVEC culture in 1 % (w/v) unmodified alginate, only 63 % of the cell population remained viable. Cell viability after 48 hours of culture decreased to a mere 40 %. Furthermore, the group found that when culturing HUVEC in unmodified alginate, cells failed to properly adhere to the alginate hydrogel. This resulted in HUVEC cultures growing as non-adherent spheres, much like those observed in the present study.

While alginate hydrogels have shown to possess several favourable properties required for biomaterial-based tissue engineering, mammalian cell types fail to properly bind to alginate due to a lack of cellular receptors which recognise alginate (Andersen *et al.*, 2015). The majority of 3D cell culture protocols involving alginate hydrogels incorporate specific peptide sequences (such as RGD-sequences) for promoting cell adhesion, spreading and

migration (Jia *et al.*, 2014). Research conducted by Lourenço (2011) showed how MSC cultures grown in unmodified alginate hydrogels result in cells having far different morphologies when compared to cells grown in RGD-coupled alginate hydrogels. When seeded onto RGD-coupled alginate hydrogels, MSC cultures attached to and spread within the hydrogel after 24 hours of culture. Contrastingly, seeded on unmodified alginate hydrogels, MSC cultures were unable to properly adhere to the hydrogel. Similar findings were reported in Dennis *et al.* (2015), where human adipose tissue stromal cells (hADSC) were found to adapt spherical cell morphologies when grown in unconjugated alginate. While culturing hADSC in RGD-coupled alginate hydrogels, cell spreading and migration was observed. In terms of HUVEC cell culture, similar findings were presented in Bidarra *et al.* (2011), where RGD-modified alginate was able to provide anchorage for HUVEC cultures, allowing for successful cellular proliferation and spreading. Unmodified alginate, however, resulted in a complete lack of cell immobilisation. Findings related to unmodified alginate encapsulation presented within this study closely supports results presented by other research groups. While viability was observed for encapsulated ad-HMSC and HUVEC cell cultures after 1 day of culture, lack of integrin binding and cell attachment resulted in practically no cell spreading and migration. Due to ad-HMSC cell viability being greater when seeding cells in 2 % (w/v) alginate compared to 1 % (w/v) alginate, observed in both live/dead staining (Figure 4.8 C i-ii) and WST-1 assays (Figure 4.14 A), 2 % (w/v) alginate was used as the primary biomaterial for printing cell-laden hydrogels in the subsequent chapter. While HUVEC viability was observed to be in favour of that of 1 % (w/v) alginate compared to 2 % (w/v) alginate, observed in both live/dead staining (Figure 4.13 C i-ii) and WST-1 (Figure 4.14 B) experiments, the present study aimed to focus primarily on achieving ad-HMSC/adipocyte viability. Further studies wherein the optimal conditions required for co-cultured ad-HMSC and HUVEC may better enable developing culture systems which preserve viability for both cell types. Analysing cell proliferation through the use of WST-1 assays over the course of several days, at a range of alginate and calcium concentrations, may provide further insight as to how cells respond to alginate encapsulation in terms of cell growth. However, that is beyond the scope of the present investigation.

Chapter 5: Three-dimensional (3D) Printing of Sodium Alginate Hydrogels

5.1 Introduction

Several challenges encountered in tissue engineering techniques may be overcome via the use of bioprinting technologies. Where decellularisation of tissues/whole organs often fails to precisely place cells or ECM components in defined locations, bioprinting allows for the precise fabrication of living cells, scaffold materials as well as biomolecules (such as growth factors) to attain complex tissue architectures (Jung *et al.*, 2016). Bioprinting stems from traditional additive manufacturing techniques whereby complex 3D structures may be fabricated by selectively adding materials in a layer-by-layer manner. Due to bioprinting being a relatively recent approach to tissue engineering, several challenges still remain. The most notable challenges associated with bioprinting include limited long-term viability of constructs post-printing as well as the central challenge of producing tissue constructs containing the required complexity in ECM organisation and micro-architecture (Tasoglu & Demirici, 2013). Furthermore, layering multiple cell types with sufficient resolution for recapitulating physiological tissues remains a challenge for researchers in the field.

The term "bioink" refers to the extruded material which gets deposited about the XYZ positioning during bioprinting techniques. Generally speaking, bioinks remain in their liquid-like states prior to 3D printing and are induced to undergo gelation once the printing process is complete or during the fabrication process. Commonly used means for inducing hydrogel gelation include photopolymerisation, temperature-induced gelation as well as chemically-induced gelation. The algal polysaccharide, sodium alginate in particular has been widely investigated for bioprinting applications due its ability to form extrudable mixtures which, when dissolved, may form high or low viscosity solutions (Jia *et al.*, 2014). Moreover, sodium alginate is able to form firm gels which are not affected by temperature. The mild aqueous calcium salt conditions required for sodium alginate gelation pose little threat to mammalian cell viability (Liberski *et al.*, 2016). Further to this, sodium alginate gels have the ability to form virtually any shape in a variety of sizes.

A challenge in 3D bioprinting of soft hydrogels such as proteins and/or polysaccharides lies in that depositing of soft materials often results in hydrogels collapsing or deforming under their own weight during the printing process. Soft hydrogels generally do not possess the mechanical strength for maintaining precise 3D geometry when printed in air. This is particularly true when hydrogels possess low elastic moduli (> 100 kPa) and require a narrow range of physical, chemical or mechanical conditions for preventing damage to both the material and the cells (Hinton *et al.*, 2015). Methods for achieving alginate printing which does not result in excessive spreading and deformation of the printed hydrogel have been to print alginate onto calcium-containing substrates. Commonly used gelatin support structures which function as calcium reservoirs have allowed for printing alginate which undergoes gelation during the actual fabrication process. Due to the diffusion of calcium ions within the printed alginate hydrogel, individual gel layers stiffen prior to additively layering additional layers above (Pataky *et al.*, 2012; Jia *et al.*, 2014). A recently developed 3D printing technique termed freeform reversible embedding of suspended hydrogels (FRESH) further aims to address the challenge of soft material deformation. FRESH printing involves depositing hydrogels within sacrificial support structures to allow for cells and hydrogel materials to embed themselves within mechanically stable environments. FRESH printing therefore allows for fabricating constructs in a layer-by-layer fashion, while maintaining spatially defined architectures (Hinton *et al.*, 2015). Use of 3D imaging data, such as MRI scans, has been used as models for FRESH printing alginate hydrogels within sacrificial gelatin support baths. Support baths consisting of gelatin micro particles allow for soft hydrogels to be fabricated in the gelatinous material acting like a Bingham plastic (i.e. material acting as a rigid body under low stress but as a viscous fluid under high stress) (Bingham, 1916). Following 3D printing, thermally-reversible gelatin support baths may be dissolved at 37 ^{o}C, resulting in the release of the printed construct.

The following chapter describes the analysis of 3D printing, co-cultured, ad-HMSC/HUVEC encapsulated sodium alginate hydrogel bioinks in air. The FRESH printing of sodium alginate bioinks was further investigated.

5.2 Methods & Materials

5.2.1 Three-dimensional (3D) Printing of Cell-laden Sodium Alginate Hydrogels

Three-dimensional printing of co-cultured ad-HMSC/HUVEC, cell-laden sodium alginate hydrogels was performed using a ReRap Prusa i3 3D printer modified with a universal paste extruder housing a 10 mL Luer-lock syringe. Preparation of the bioink involved growing ad-HMSC (P_5) and HUVEC (P_3) cell cultures to confluence in separate 75 cm^2 cell culture flasks. Day 6 adipogenic-induced ad-HMSC, co-cultured with HUVEC, were used for bioprinting. Ad-HMSC were grown to confluence using fully supplemented α-MEM. Upon achieving confluence, ad-HMSC were induced for adipogenic differentiation using the standard adipogenic differentiation protocol for 6 days (refer to section 4.1.3.2). Human umbilical vein endothelial cells were cultured in all-in-one ECGM. Upon achieving confluence, cell cultures were trypsinised using the standard subculturing protocol. Respective cells pellets were resuspended together in sterile (autoclaved, 120 ^oC) 2 % (w/v) sodium alginate gel solutions made up using Ca^{2+} and Mg^{2+}-free DPBS (pH 7.4) at densities of 1 x 10^6 cells/mL per cell type. Encapsulated alginate gels were then transferred to sterile 10 mL Luer-lock syringes. Sterile 23 G syringe needles (0.34 mm needle inner diameter) were attached to the ends of syringes prior to housing within the RepRap Prusa i3. Cell-laden sodium alginate hydrogels were printed onto sterile plastic cell culture dishes (NEST, 9.62 cm^2). The RepRap Prusa i3 was housed in a Vivid Air biosafety cabinet containing an air filter and UV sterilisation lamp (Supplementary Material, Figure S3). Sterilisation of the cabinet and 3D printer was achieved by broad-spectrum UV radiation for one hour prior to initiating the printing process. A filtered air flow of 100 Pa was maintained within the cabinet at all times during the sterilisation and printing processes.

Following the printing process, co-cultured constructs were maintained in 1:1 ratios of AMM:ECGM cell culture media. Media was replaced with fresh AMM:ECGM after 3 days. Printed cell-laden hydrogels were incubated at 37 ^oC, in a humidified 5 % (v/v) CO_2 atmosphere.

5.2.2 Live/Dead staining of Three-dimensional (3D) Printed Constructs

Live/dead cell staining of 3D printed constructs was performed 1 and 7 days post-printing. Cell culture media was removed and replaced with live/dead staining solution consisting of DMEM, 1 % (v/v) PSA, 19.2 μM FDA and 30 μM PI. Cells were incubated with live/dead staining solution

for 4 minutes in the dark following removal of the staining solution. Printed constructs were then washed with Ca^{2+} and Mg^{2+}-free DPBS (pH 7.4). Constructs were transferred to glass bottom culture dishes where Ca^{2+} and Mg^{2+}-free DPBS (pH 7.4) was added to prevent drying of the hydrogels. Samples were analysed using a Zeiss LSM780 Laser Scanning Confocal Microscope at 100X magnification. Dead (red) cells were detected using the dsRED filter (563 nm/581 nm), whereas live (green) cells were detected using the FITC filter (495 nm/519 nm). On average, Z-stacked fluorescence micrographs consisted of 32 slices of which slices were captured at 30 μm intervals (960 μm Z-stack depth). A total of three bioprinting experiments were performed as described. Two images images were captured per culture time for successful bioprinting experiments. Cell viability (%) was quantified (calculated) from 28 of the bottom-most live/dead staining images using the cell viability equation described in Equation 4.2 (refer to section 4.2.10).

5.2.3 Freeform Reversible Embedding of Suspended Hydrogels (FRESH) Printing

5.2.3.1 Gelatin Slurry

Freeform reversible embedding of suspended hydrogels printing was performed using methods similar to those described in Hinton *et al.* (2015). Gelatin slurry support baths were created by dissolving gelatin (type B) from bovine skin (Sigma, Cat. No. G9391) at 4.5 % (w/v) in 30 mM $CaCl_2$ solution in a glass Schott bottle (Figure 5.1 A). Gelatin was dissolved by heating to 80 ^{o}C with vigorous stirring for 1 hour. The gelatin solution was then placed at 4 ^{o}C overnight for complete gelling. Next, gelatin was blended at pulse speed using a Safeway consumer-grade 1.5 L jug blender (Figure 5.1. B) in 230 mL $CaCl_2$ (30 mM) at 4 ^{o}C. Blended gelatin micro particles were transferred to 50 mL centrifuge tubes (Figure 5.1 C) and centrifuged at 4 200 rpm for 2 minutes (4 ^{o}C) such that gelatin particles could be separated out of suspension (Figure 5.1 D). Supernatant was removed and gelatin particles were suspended back in $CaCl_2$ (30 mM; 4 ^{o}C) by vortexing. The gelatin slurry was then centrifuged as before. This process was repeated until no bubbles could be seen in the supernatant, indicating that the majority of soluble gelatin had been removed. Once no air bubbles were visible, supernatant was removed and the gelatin slurry could be stored at 4 ^{o}C. To determine the effect blend time had on particle size, gelatin was dissolved as before but containing 1 % (v/v) Robertson's food colouring (Red). Gelatin was blended for

periods of 60, 90, 120 and 135 seconds. Blend times longer than 135 seconds resulted in gelatin particles being fully dissolved in solution. For each blend time analysed, 500 µL gelatin slurry was diluted to 10 mL in sterile (autoclaved, 120 °C) $CaCl_2$ (30 mM; 4 °C). For each diluted sample, 140 µL was transferred to a glass coverslip. Bright field images were captured using a Zeiss Axio.Vert.A1 FL-LED Fluorescence Microscope at 50X magnification. A single experiment to determine average particle area as a function of blend time was performed. Average particle area for various blend times were determined by importing triplicate bright field images per time point into SketchAndCalc area calculator application followed by manually drawing the particle perimeters.

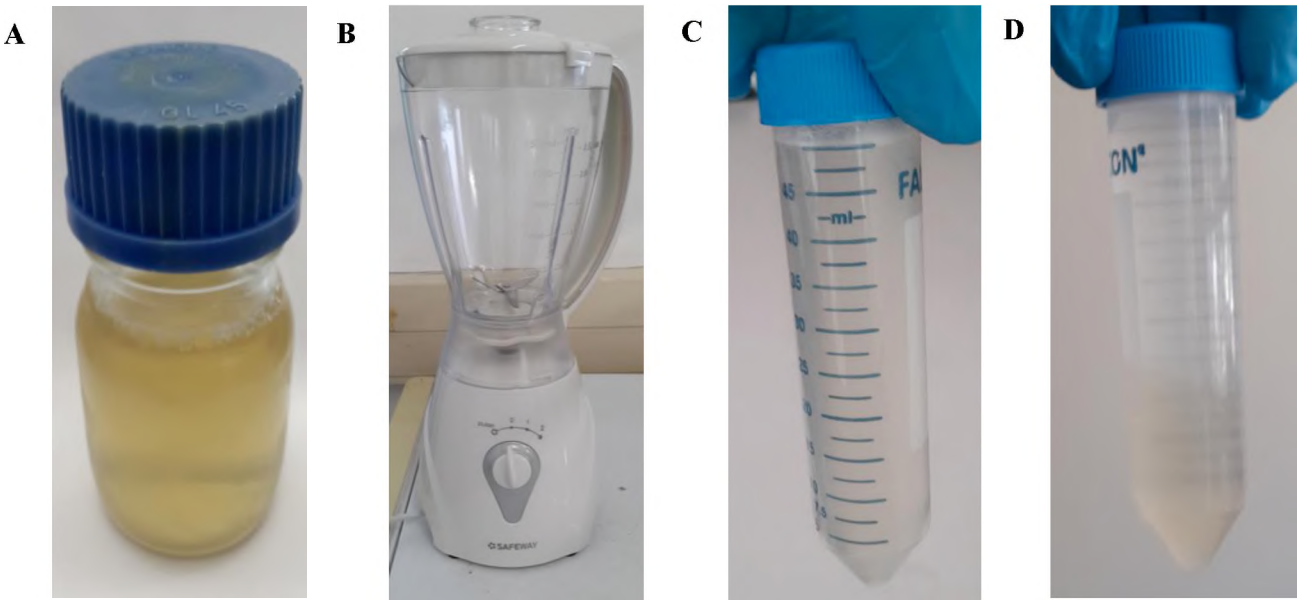

Figure 5.1: Gelatin slurry support bath. A: Bovine gelatin (type B) dissolved in $CaCl_2$ (30 mM) was gelled overnight at 4 °C prior to diluting and blending. B: Consumer-grade table-top Safeway 1.5 L jug blender used for blending the diluted gelatin block. C: Suspended gelatin micro particles prior to centrifugation. D: Gelatin micro particles separated from supernatant following centrifugation (4 200 rpm) for 2 minutes.

5.2.3.2 Freeform Reversible Embedding of Suspended Hydrogels (FRESH) Printing Process

For FRESH printing, slurries were poured in plastic cell culture dishes (9.62 cm^2). All FRESH printing was performed using gelatin blended for 135 seconds. Following FRESH printing, melting of the gelatin support bath and subsequent release of the printed alginate construct was achieved by placing plastic culture dishes on a heated plate (37 ^oC) for 5 minutes. Gelatin solution was removed by pipetting. All STL files used for FRESH printing were designed in SketchUp Make (v16.0.1), sliced in Cura (v15.04.4; 1 mm layer height) and printed using Pronterface (printrun-20150310) controller software.

5.2.3.3 Atomic Force Microscopy (AFM)

The Young's modulus of FRESH printed cell-free sodium alginate (2 % w/v) was determined using the Asylum Research MFP-3D Classic AFM unit. Following FRESH printing and release of the alginate construct, alginate gel was transferred to a Platinum Sample Pan (100 µL) such that indentation of the gel by the cantilever would not result in excessive spreading. Indentation of the gel was performed using a TR400PSA nitride probe. The spring constant for the cantilever was found to be 1.0 N/m. To perform the indentation, the tip was held stationary above the surface of the gel and moved with X and Y offsets, allowing for the test to be performed in the middle of the gel. A single indentation measurement was taken. Igor Pro v6.74 software was used to generate a force curve.

5.2.3.4 Freeform Reversible Embedding of Suspended Hydrogels (FRESH) Printing Accuracy

Two rectangular geometries were designed in SketchUp Make (v16.0.1) and sliced in Cura (v15.04.4) software at 1 mm layer height. A rectangle with dimensions of 15 mm x 1 mm x 1 mm (length x breadth x height) was used for determining the printing accuracy of a single layer construct, whereas a rectangle with dimensions of 15 mm x 1 mm x 2 mm was used for determining the printing accuracy of a dual layer construct. Experiments were performed in triplicate using sodium alginate (2 % w/v) embedded within gelatin slurries. Following release of the alginate gel and removal of the dissolved gelatin slurry, dimensions of the printed constructs were determined by measurement using a cantilever. Printing accuracy was quantified based on

the overlap of the printed construct volume to that of the designed volume. Printing accuracy (%) was calculated using equation 5.1 below.

$$\boldsymbol{Printing\ Accuracy}\ (\%) = \left(\frac{\boldsymbol{A}}{\boldsymbol{Ai}}\right)\boldsymbol{x}\ \mathbf{100}\ \%$$

Equation 5.1: Printing accuracy (%) of freeform reversible embedding of suspended hydrogels (FRESH) printed 2 % (w/v) sodium alginate hydrogels. $\boldsymbol{A}$ represents the designed volume and $\boldsymbol{A_i}$ represents the measured construct volume.

5.3 Results & Discussion

5.3.1 Live/Dead Staining of Three-dimensional (3D) Printed Cell-laden Sodium Alginate Hydrogels

Three-dimensional printing of co-cultured HMSC (P_5) and HUVEC (P_3) was performed by encapsulating both cell cultures within the same sodium alginate hydrogel preparations at relatively low cell densities (1 x 10^6 cells/mL per cell type). Printed day 6 adipogenic-induced ad-HMSC, co-cultured with HUVEC, was investigated. Prior to 3D printing, encapsulated hydrogel solutions were transferred to sterile 10 mL Luer-lock syringes fitted with sterile 23 G syringe needles (0.34 mm needle inner diameter). A simple square stereolithography (STL) geometry (0.5 mm wall thickness) was designed in SketchUp Make software (v16.0.1) and subsequently imported to Cura software (v15.04.4) for slicing. Stereolithography files were adjusted such as to produce constructs containing two layers in width (XY) and two layers in height (Z). Layer height was designed to be 1 mm. The overall geometry of the square was 10 mm x 10 mm x 2 mm (length x breadth x height) (Figure 5.2). The G-code used for printing the construct can be found in the Supplementary Material (G-code 1).

Printing of alginate hydrogels in air consistently resulted in deformation and spreading of the construct. Due to the relatively low viscosity of the 2 % (w/v) alginate solution, deformation was most likely as a result of the hydrogel lacking the mechanical integrity to support its own weight following extrusion. An attempt was made to print cell-laden alginate bioinks directly into sterile $CaCl_2$ containing culture dishes. However, rapid polymerisation of the hydrogel within the syringe needle resulted in clogging of the needle, causing a pressure buildup within the syringe.

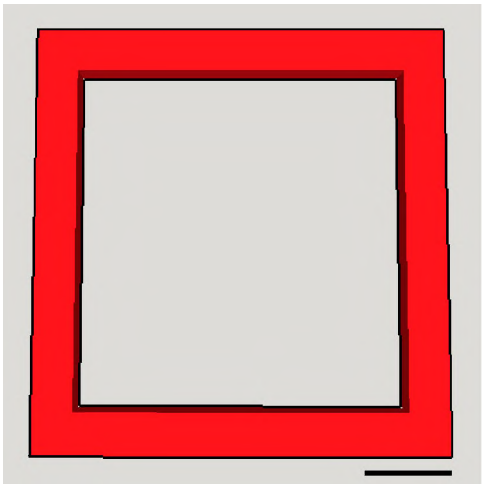

Figure 5.2: Designed square geometry. The STL file of the square was designed in SketchUp Make (v) and sliced in Cura (V) software to generate the Gcode. Dimensions of the square were 10 mm x 10 mm x 2 mm (length x breadth x height). Image rendered in SketchUp Make. Scale bar represents 2 mm.

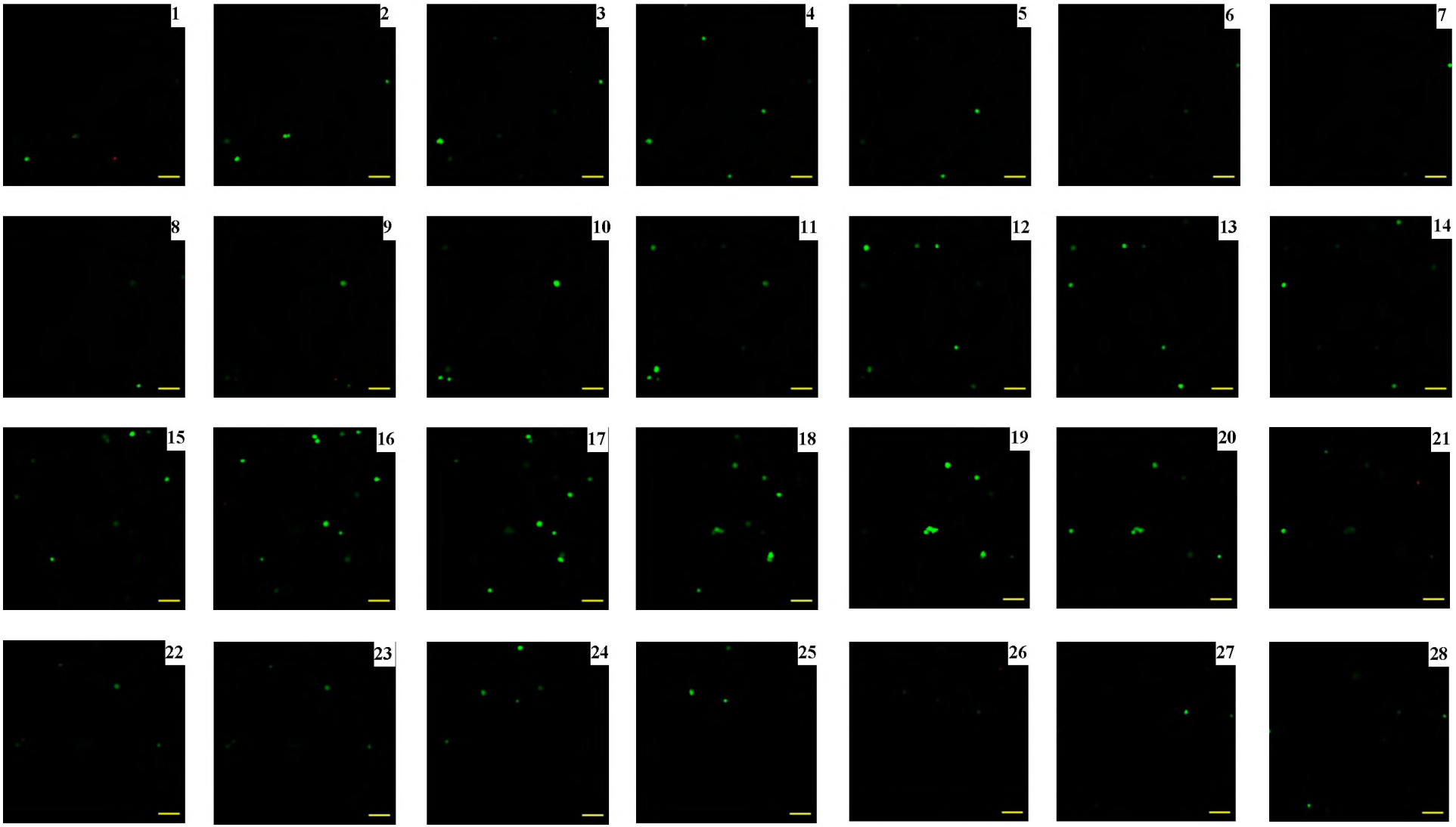

Figure 5.3: Day 1 live/dead staining of three-dimensional (3D) printed adipogenic-induced ad-HMSC/HUVEC co-culture encapsulated in sodium alginate (2 % w/v). ad-HMSC (P_5) were induced for adipogenic differentiation 6 days prior to printing. Co-cultures were maintained in AIM:ECGM at a 1:1 ratio. Images were captured using a Zeiss LSM780 Laser Scanning Confocal Microscope at 100X magnification. Scale bars represent 100 µm. Images represent fluorescence micrographs from the bottom of the gel (1) to the top of the gel (28) at 30 µm intervals. Images representative of multiple images (n=3).

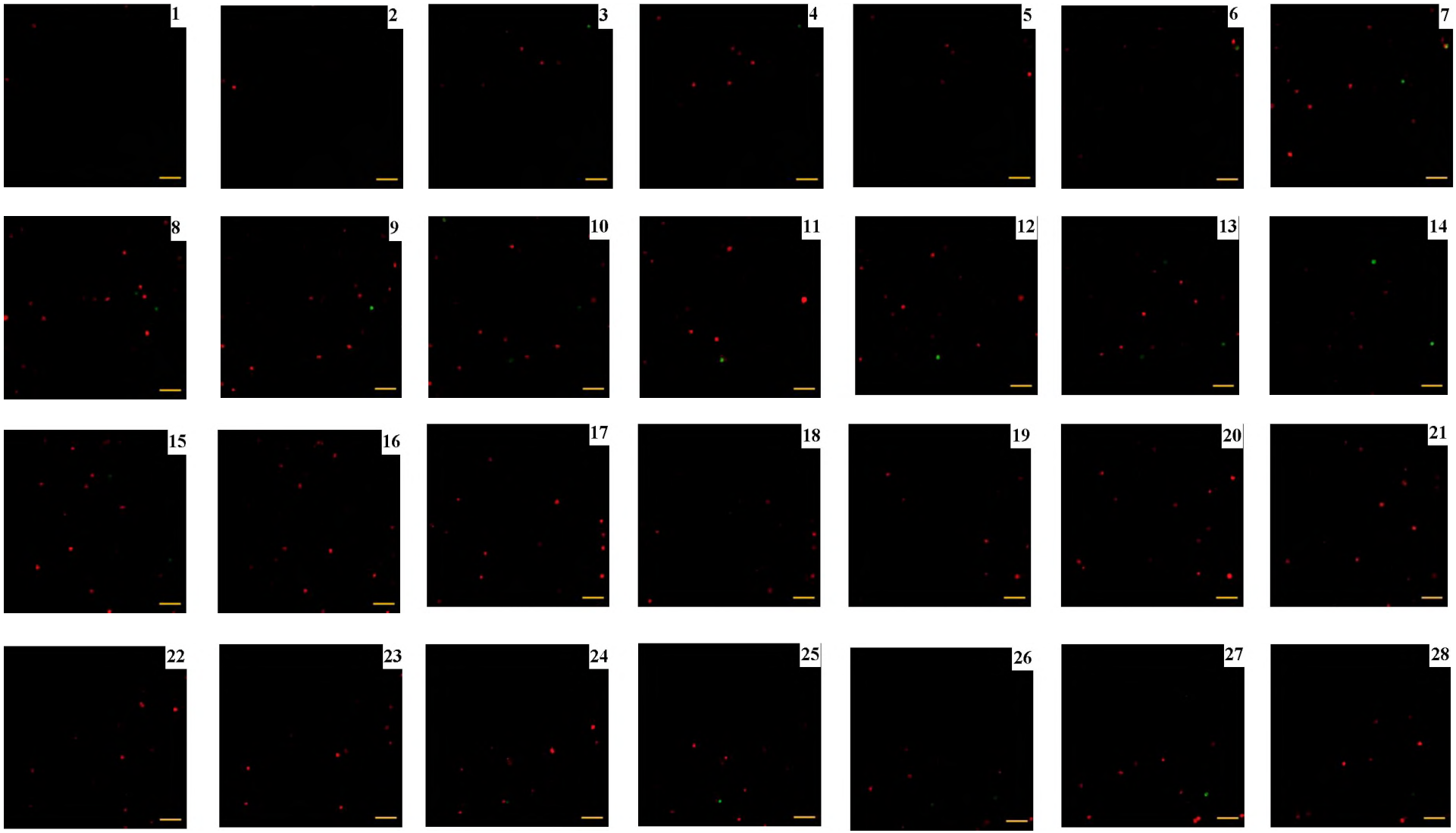

Figure 5.4: Day 7 live/dead staining of three-dimensional (3D) printed adipogenic-induced ad-HMSC/HUVEC co-culture encapsulated in sodium alginate (2 % w/v). ad-HMSC (P_5) were induced for adipogenic differentiation 6 days prior to printing. Co-cultures were maintained in AMM:ECGM at a 1:1 ratio. Images were captured using a Zeiss LSM780 Laser Scanning Confocal Microscope at 100X magnification. Scale bars represent 100 µm. Images represent fluorescence micrographs from the bottom of the gel (1) to the top of the gel (28) at 30 µm intervals. Images representative of multiple images (n=3).

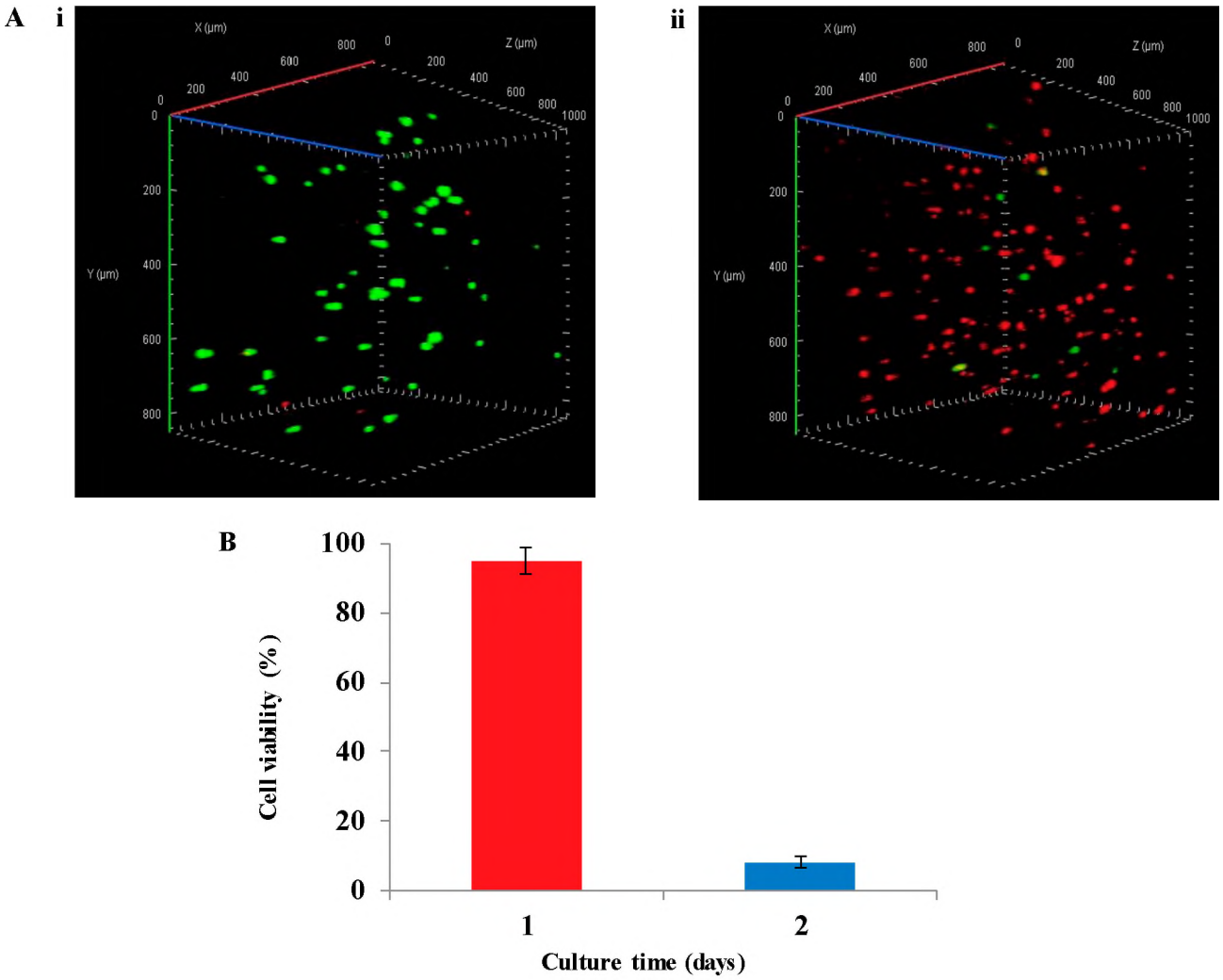

Figure 5.5: Live/dead assay of three-dimensional (3D) printed adipogenic-induced ad-HMSC/HUVEC co-culture encapsulated in sodium alginate (2 % (w/v) bioink. ad-HMSC (P_5) was induced for adipogenic differentiation 6 days prior to printing. A: Live/dead staining images. i) Day 1, ii) Day 7. Co-cultures were maintained in AMM:ECGM at a 1:1 ration. Cartesian axes represented by the red (X), green (Y) and blue (Z) lines. Images were captured using a Zeiss LSM780 Laser Scanning Confocal Microscope at 100X magnification. Images representative of multiple images (n=2). B: Cell viability calculated from duplicate live/dead images. Error bars represent standard deviation. Results are representative of a single bioprinting experiment.

Live/dead staining of 6 day adipogenic differentiating ad-HMSC (P_5) co-cultured with HUVEC (P_3) revealed high cell viability 1 day post printing (Figure 5.3, Figure 5.5 A). Live (green) cells were present throughout the entirety of the gel. However, the live cell density was far greater near the middle of the gel (Figure 5.3 (15-20)). The middle of the gel most likely contained a greater degree of elasticity compared to that of the bottom or top of the gel, which may have aided in cell entrapment. Cell clumping was also greater toward the middle regions of the gel. Dead (red) cells were most commonly found near the bottom or top regions of the gel (Figure 5.3

(1, 21, 26)). Contrastingly, live/dead staining of printed co-cultures on Day 7 revealed significantly lower cell viability compared to that of Day 1 cultures (Figure 5.4, Figure 5.5 B). Similar to Day 1 live/dead staining, Day 7 cultures showed greater cell densities in the middle of the gel, be it that of mostly dead (red) cells (Figure 5.3 (7-24).Although, nearly all live (green) cells at Day 7 were present within the middle of the gel (Figure 5.4 (7, 9, 11-14, 25-27)). Cell viability was calculated (Equation 4.2) as 95.1 % at Day 1, whereas Day 7 cell viability was calculated as 8.0 %.

The effect various co-culture media compositions have on ad-HMSC and HUVEC cellular proliferation was investigated in Kang *et al.* (2009), where it was determined that when grown in the presence of endothelial growth media (EGM) in a 1:1 ratio with AIM, ad-HMSC cellular proliferation was substantially greater than that of HUVEC cultures after 17 days. Culturing HUVEC in EGM:AIM (1:1 ratio) resulted in a significant decrease in proliferation. The group further describes how culturing ad-HMSC and HUVEC in a 1:1 ratio of EGM:AMM resulted in cell proliferation for both cell types. The present study therefor investigated co-culturing ad-HMSC and HUVEC using ECGM:AMM at a 1:1 ratio. While the present study focused on cell viability following 3D printing of ad-HMSC/HUVEC co-cultures, further investigation into the optimal culture conditions required for maintaining cell viability is required for long term cell viability of co-cultures. In the present study, calculated cell viability drastically decreased after 6 days of culture. Most likely due to lack of alginate attachment and/or inadequate culture conditions required for long term viability of co-cultures. A total of three bioprinting experiments were performed whereby only one experiment resulted in un-contaminated cultures after 7 days. Prior experiments involving seeding ad-HMSC/HUVEC cultures in alginate hydrogels that were primarily sterilised by autoclaving (120 ^{o}C), proved that autoclaving was sufficient for sterilising the polymer to allow for cellular proliferation (refer to section 4.3.2). Therefore, contamination of biorpinted constructs most likely took place during the printing process and was not as a result of contaminated bioink material. Sterilisation of the biosafety cabinet, in which the modified RepRap Prusa i3 was housed, was done by UV radiation one hour prior to initiating printing. Furthermore, the cabinet and print bed was thoroughly wiped with 70 % (v/v) ethanol solution prior to printing. A constant air-flow was maintained throughout the printing process. Additional measures to ensure sterility while printing may be to radiate the print surface with a UV radiation lamp in close proximity to the print bed, as the lamp used in the

present system was relatively far away from that of the printer. While control (cell-free) bioink samples were not printed and analysed in the present study. Cell-free controls may provide insight as to whether fungal or bacterial contamination was occurring during the printing process. Furthermore, incorporating increased antimycotic concentrations may improve long-term cell viability of printed cell cultures by reducing the occurrence of contamination.

Mammalian cell types fail to properly bind to alginate due to a lack of cellular receptors which recognise alginate (Andersen *et al.*, 2015). As a result, the majority of cells present in the bioink at the start of printing most likely failed to adhere to and be incorporated within the printed contract. The vast majority of 3D bioprinting using alginate hydrogels make use of peptide-conjugated alginates or hybrid alginate bioink formulations, such that proper cell attachment, spreading and proliferation may be achieved. Furthermore, unmodified alginate hydrogels have slow degradation rates due to the non-interactive nature of alginate (Pati *et al.*, 2014). Jia *et al.* (2014) thoroughly investigated the bioprintability of RGD-coupled sodium alginate hydrogels and found that by varying the degree of alginate oxidation, controlled degradation of alginate could be achieved whilst preserving ad-SC proliferation and spreading. Furthermore, Duan *et al.* (2013) investigated the 3D bioprinting of encapsulated alginate/gelatin hybrid hydrogels and found that remnant gelatin post-alginate gelation was able to support attachment and spreading of mammalian cells. Similar findings were reported in Wu *et al.* (2016), where bioprinted cell-laden alginate/gelatin/collagen hybrid hydrogels better mimicked tissue-specific ECM and aided in achieving higher cell viability post-printing. While the present study focused on printing unmodified cell-laden alginate hydrogels, future work could benefit greatly from investigations into potential modifications/alterations to alginate bioink compositions.

5.3.2 Freeform Reversible Embedding of Suspended Hydrogels (FRESH)

Due to the lack of spatial control associated when printing sodium alginate hydrogels in air, FRESH printing of sodium alginate in gelatin support baths was investigated. Freeform reversible embedding of suspended hydrogel printing was first described in Hinton *et al.* (2015). The technique is based upon the principal of embedding soft materials (such as proteins or polysaccharides) which typically possess low elastic moduli (<100 kPa) within mechanically stable support structures, such that complex 3D biological structures may be fabricated. The lack of mechanical integrity associated when 3D printing biologically relevant hydrogels in air may

be overcome when FRESH printing liquid-phase materials in support baths which prevent diffusion of the printed construct. Sodium alginate FRESH printing was investigated in this study due to the ability alginate hydrogels have for rapid polymerisation when exposed to calcium ions. Furthermore, inexpensive gelatin support baths containing $CaCl_2$ (0.33 % w/v) were able to act as stable, thermally-reversible environments for alginate polymerisation and subsequent release of alginate hydrogels when heating (37 ^{o}C). While rheological analysis of the gelatin support structure was not conducted in this study, other studies have shown how gelatin microparticles act like a Bingham plastic which can be used for 3D printing soft hydrogels in complex geometries (Hinton *et al.*, 2015). A similar approach has been used for printing of hydrogels in poly(acrylic acid) (Carbopol) microparticulate support baths (Bhattacharjee *et al.*, 2015, Hinton *et al.*, 2016).

5.3.2.1 Optimal Gelatin Blend Time

To determine the effect blend time had on gelatin micro particle size, gelatin was dissolved in red food colouring (Robertson's, 1 % v/v) and blended for 60, 90, 120 and 135 seconds, followed by imaging with bright field microscopy (Figure 5.6 A i-iv). Bright field images were imported into SketchAndCalc application where relative particle areas were calculated by manually drawing perimeters around gelatin particles. When blending for periods longer than 135 seconds, gelatin would dissolve back into solution.

Following blending of gelatin and subsequent calculation of average micro particle area for various blend times, results highlight that blend time has a direct effect on gelatin particle size. Increasing gelatin blend time results in a uniform decrease in particle area (Figure 5.6 B). A similar relation is reported in Hinton *et al.* (2015), when gelatin particle diameter was plotted as a function of blend time. Gelatin blended for 135 seconds was used for FRESH printing in this study, as particle areas were small (127 ± 95 μm^2) and particles did not dissolve back into solution.

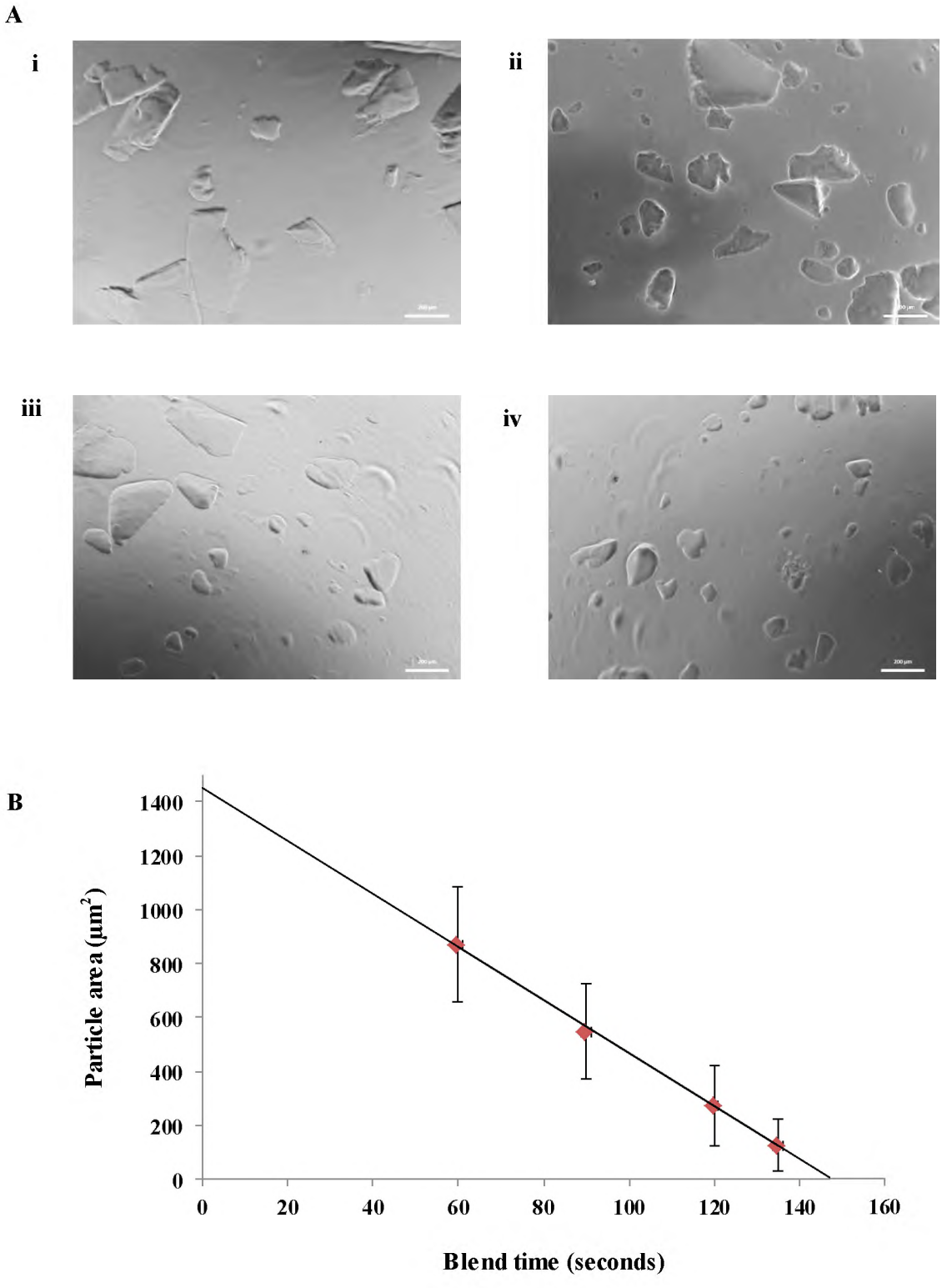

Figure 5.6: Blended gelatin particles. A: Bovine gelatin (type B) was blended for i) 60, ii) 90, iii) 120, iv) 135 seconds using a table-top Safeway blender. Bright field images were captured using a Zeiss Axio.Vert.A1 FL-LED Microscope at 50X magnification with a Ph 2 filter. Scale bars represent 200 µm. Images representative of multiple (3) images (n=1). B: Mean area of gelatin particles as a function of blend time from 60 seconds to 135 seconds (20 or more calculated particles were analysed per time point; the black line is a linear fit and error bars indicate standard deviation).

5.3.2.2 Freeform Reversible Embedding of Suspended Hydrogels (FRESH) Printing

Similar to the experiments involving 3D printing of alginate onto plastic culture dishes, FRESH printing was performed using a RepRap Prusa i3 modified with a universal past extruder, housed within a biosafety cabinet. To avoid clogging of the syringe needle with hydrogel material, a sterile 23 G needle (0.34 mm inner diameter) was attached to the end of the Luer-lock syringe prior to initiating the printing process. FRSH printing alginate constructs which retain mechanical integrity (such as to not collapse or deform under its own weight) was achieved when printing 2 % (w/v) alginate hydrogels within gelatin support baths comprising of gelatin micro particles. Initial FRESH printing experiments were performed using cell-free sodium alginate hydrogels. Constructs with simple geometries were designed in SketchUp Make software (v16.0.1). For non-biological fresh printing, alginate hydrogels were mixed with red Robertson's food colouring (1 % v/v) for visualising constructs within the gelatin support bath. A square structure identical to that described for 3D printing cell-laden alginate (10 mm x 10 mm x 2 mm; refer to section 5.3.1) (Figure 5.7 B i) consisting of two layers in height and width, of which the layer height and width was designed to be 1 mm, was initially used for testing alginate FRESH printing within a gelatin slurry (Figure 5.7 B ii). The G-code used for printing the square can be found in the Supplementary Material (G-code 1). Printing (FRESH) of the structure proved successful (Figure 5.7 B ii), however, slight diffusion of the red food colouring accounted for the observed red/pink solution on the side of the culture dish (Figure 5.7 B ii dark blue arrow). Release of the square structure was achieved by melting (37 ^{o}C) the gelatin support (Figure 5.7 B iii). Dissolved gelatin was removed by pipetting. Lack of sufficient alginate deposition experienced at the start of printing resulted in slight irregularity on the one side of the printed square (Figure 5.7 B iii purple arrow). Following FRESH printing of a square, a basic grid structure (19 mm x 10 mm x 2 mm) was designed as before (Figure 5.7 C i). Similar to the FRESH printed alginate square, the grid was designed to be printed as two layers in height and width, of which the layer height and width was designed to be 1 mm. The G-code used for printing the grid can be found in the Supplementary Material (G-code 2), along with a video clip of the printing process (Video S3). Printing (FRESH) of the grid produced a complete construct containing minimal over printing (Figure 5.7 7 ii). Slight dragging of the alginate hydrogel was experienced when the syringe needle moved over the inner section of the grid (Figure 5.7 C iii red arrow).

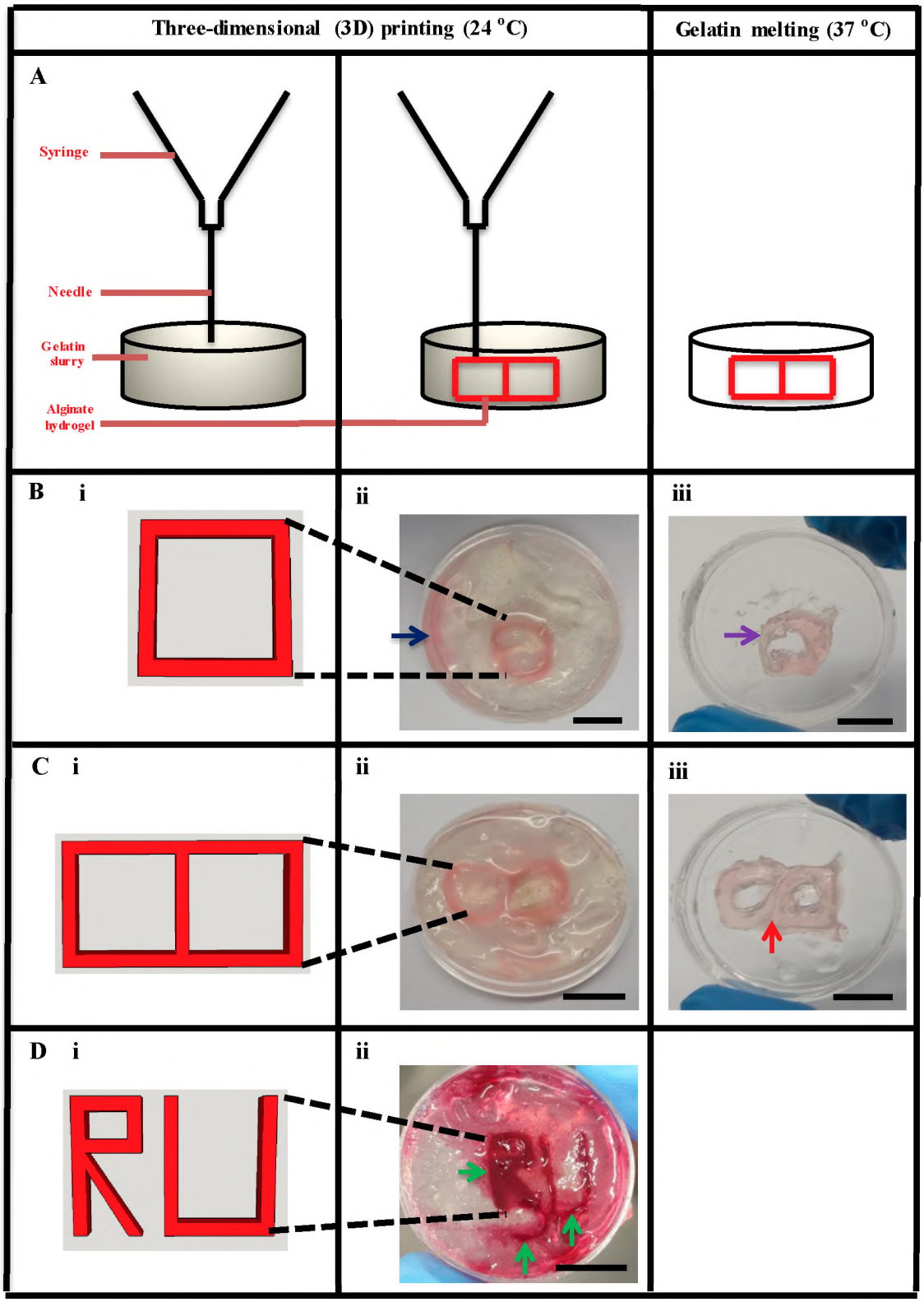

Figure 5.7: Freeform reversible embedding of suspended hydrogels (FRESH) printing through deposition of sodium alginate precursor ink within thermally reversible gelatin support bath. A: Schematic of the FRESH printing process whereby sodium alginate (red) is extruded within a gelatin slurry support bath (grey) at room temperature (24 °C). Gelatin melting (37 °C) results in release of the printed construct. B: Dual-layer square construct (10 mm x 10 mm). i) Rendered STL of square, ii) Printed construct embedded within gelatin support bath (24 °C), iii) Printed alginate construct following gelatin dissolving and release of hydrogel (37 °C). C: Dual-layer grid constructs (20 mm x 10 mm). i) Rendered STL of grid, ii) Printed construct embedded within gelatin support bath (24 °C), iii) Printed alginate construct following gelatin dissolving and release of hydrogel (37 °C). D: Dual-layer RU construct (25 mm x 18 mm). i) Rendered STL of RU, ii) Printed construct embedded within gelatin support bath (24 °C). Scale bars represent 10 mm. Stereolithography images were rendered in SketchUp Make (v16.0.1).

Dragging of alginate was most likely as a result of premature polymerisation of the hydrogel within the syringe needle. Printing (FRESH) of alginate (2 % w/v) constructs with relatively large, simple geometries, such as the square and the grid, was achieved using the modified RepRap Prusa i3. Thus, following the initial FRESH printing experiments, printing of more complex geometries was attempted. Specifically, a RU symbol (representing Rhodes University) was designed (Figure 5.7 D i) and FRESH printed as previously described (Figure 5.7 D ii). The G-code used for printing the RU construct can be found in the Supplementary Material (G-code 3). Printing (FRSH) of an RU symbol was done using alginate (2 % w/v) containing significantly higher food colouring concentrations (3 % v/v) such that the printed construct could easily be distinguished from over

-printed areas or areas of diffused food colouring. Lack of sufficient syringe retention when moving across the gelatin slurry, as well as polymerisation of hydrogel material within the syringe needle, continuously resulted in dragging of the polymerising hydrogel. As a result, printing resolution was negatively affected and overprinted areas were evident in several areas within the gelatin support (Figure 5.7 D ii green arrows). This resulted in overall deformation of the printed construct when gelatin was dissolved and the alginate was released.

5.3.2.3 Atomic Force Microscopy (AFM)

Sodium alginate (2 % w/v) was FRESH printed in a gelatin support bath. Following melting (37 ^{o}C) of the gelatin support bath and release of the alginate construct, alginate was subjected to rheological analysis using an Asylum Research MFP-3D Classic AFM unit. The Young's Modulus (E) was determined using the Hertz method due to the sample being unable to reform after contact with the cantilever. Determining the elastic properties (such as the elastic modulus) of biological samples may be achieved using the Hertzian model (i.e. linear elastic and noninteractive probe-sample pairing) (Lin *et al.*, 2007). The Hertz model describes the case of elastic deformation of two perfectly homogenous smooth bodies touching under load (Hertz, 1882; Kuznetsova *et al.*, 2007).

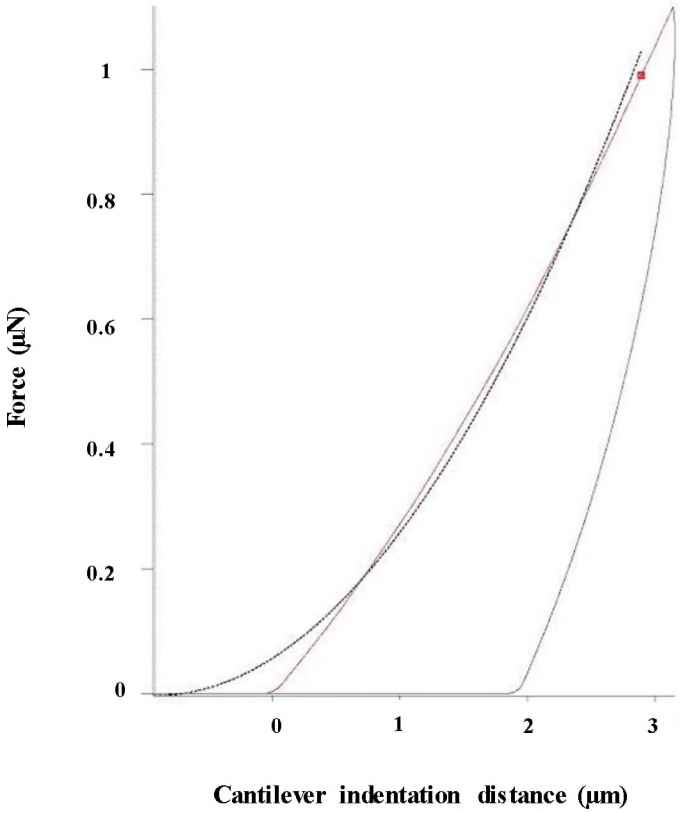

Figure 5.8: Force curve generated from Atomic Force Microscopy (AFM) of freeform reversible embedding of suspended hydrogels (FRESH) printed sodium alginate. Sodium alginate (2 % w/v) was FRESH printed and gelled within a $CaCl_2$ (30 mM) containing gelatin support bath for 10 minutes prior to analysis. The red line represent the contact made by the cantilever on the hydrogel (n=1).

Printing (FRESH) alginate (2 % w/v) was found to have a Young's modulus of 127.6 ± 95 kPa when force curves were generated using the Hertzian model (Figure 5.8). Similar values were obtained in Kaklamani *et al.* (2014), where the Young's modulus of sodium alginate (2.5 % w/v) was calculated as 150 kPa when gelled using a $CaCl_2$ (1 M) solution. The elastic properties of alginate hydrogels are directly affected by alginate concentration as well as gelation-inducing ion concentration (Andersen *et al.*, 2015). Thus, the Young's modulus of 2 % (w/v) alginate determined in this study (127.6 ± 95 kPa) was lower than that of the modulus determined in Kaklamani *et al.* (2014) (150 kPa), due to the decreased alginate $CaCl_2$ concentration (30 mM compared to 1 M) and alginate concentration (2 % w/v compared to 2.5 % w/v). A thorough analysis of FRESH printed alginate elastic properties using a range of alginate and calcium concentrations may provide further insight regarding the effect concentrations have on alginate elasticity.

5.3.2.4 Freeform Reversible Embedding of Suspended Hydrogels (FRESH) Printing Accuracy

A fundamental property to consider for effective 3D printing (including bioprinting) is that of printing accuracy. For the purpose of this discussion, printing accuracy is defined as the accuracy with which printed constructs have identical geometries to that of the designed constructs (i.e. printed constructs which lack over-printed or under-printed areas). Printing accuracy is quantified as the percentage overlap of the printed volume to that of the designed volume. The printing accuracy of FRESH printed sodium alginate (2 % w/v) was determined by comparing the difference in volume of printed constructs to that of designed geometries. An STL file of a rectangular shaped construct with dimensions of: 15 mm 1 mm x 1 mm (length x breadth x height) (15 mm^3 volume) was designed in SketchUp Make (v16.0.1) and sliced in Cura (v15.04.4) at 1 mm layer height (Z) for printing of a single layer construct (Figure 5.9 A). The construct was designed to consist of two layers in width (0.5 mm shell thickness). A second construct with dimensions of 15 mm 1 mm x 2 mm (30 mm^3 volume) was designed and sliced at 1 mm layer height (Z) for printing of a dual layer constructs (Figure 5.9 B). The dual layer construct also consisted of two layers in width (0.5 mm shell thickness). The G-codes used for FRESH printing both the single and dual layer rectangular constructs can be found in the Supplementary Material (G-code 4 & G-code 5, respectively). The printing accuracy (percentage overlap of printed to designed volume) was calculated using Equation 5.1. Findings are highlighted in Table 5.1.

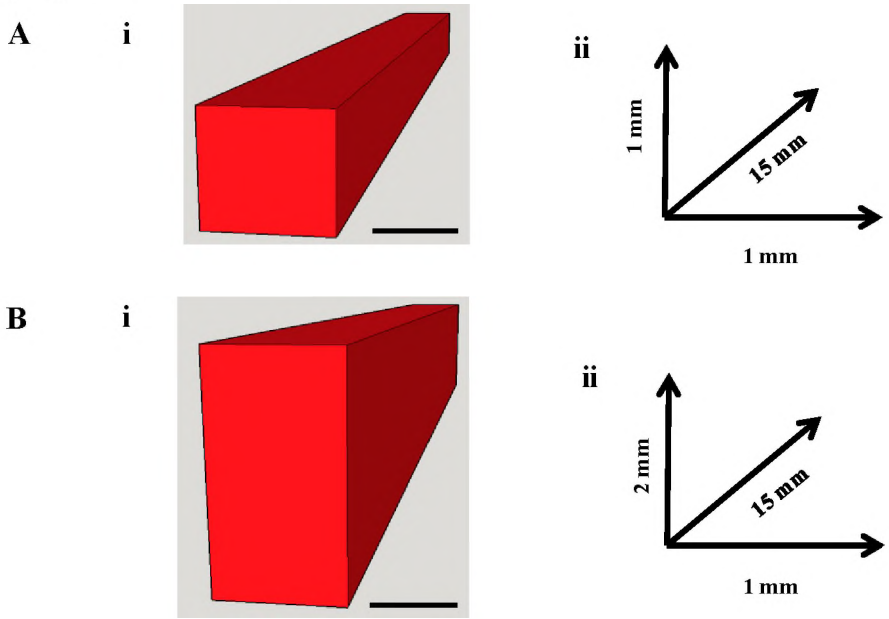

Figure 5.9: Designed rectangular constructs. A: Single layer rectangle. i) Rendered design, ii) Designed geometries (15 mm x 1 mm x 1 mm). B: Dual layer rectangle. i) Rendered design, ii) Designed geometries (15 mm x 1 mm x 2 mm). Images were rendered in SketchUp Make (v16.0.1). Constructs were printed at 1 mm layer height. Scale bars represent 500 µm.

Table 5.1: Printing accuracy of designed construct volume to that of printed alginate. Sodium alginate (2 % w/v) was FRESH printed and gelled within a $CaCl_2$ (30 mM) containing gelatin support bath. Printing accuracy (%) was calculated as the percentage overlap of printed to designed volume (n=3).

Layers	Designed construct volume (mm^3)	Average printed construct volume (mm^3)	Printing accuracy (%)
1	15	52.32 (± 4.82)	28.83 (± 2.54)
2	30	118.83 (± 26.86)	26.06 (± 5.42)

For all FRESH printed alginate (2 % w/v) constructs, overprinting of the hydrogel was noted. This was most likely as a result of swelling (hydration) of the polymerising alginate, as well as over-extrusion of the alginate solution due to excessive pressure build-up within the syringe. Printing accuracy was thus calculated as the percentage ratio of the designed construct volume relative to that of the printed construct volume (Equation 5.1) When FRESH printing single layer constructs within the gelatin support bath, printing accuracy was calculated to have an average of 28.83 (± 2.54) %, for triplicate experiments (Table 5.1). Printing dual layer constructs resulted in an average printing accuracy of 26.06 (± 5.42) %, for triplicate experiments (Table 5.1). Ideally, the optimal printing accuracy should be 100 % (i.e. no overlap of printed to designed volume) such that printing constructs containing no over-printed or under-printed areas could be achieved. While in the present study printing accuracy was noted to be significantly below the ideal level of accuracy, relatively low deviations within multiple experiments highlight the reproducibility with which the system has for printing constructs. The system was able to print constructs with near-identical geometries for triplicate experiments. These results support the FRESH printability of alginate. However, high fidelity printing, particularly of constructs with small geometries, requires optimisation with regard to alginate viscosity, crosslinking kinetics, gelatin particle size and printing parameters (printing speed and flow rate). Furthermore, an investigation into the swelling effects FRESH printing has on alginate gelation

may allow for an improved means for determining the printing accuracy of FRESH printed constructs. Improving printing fidelity may be achieved when utilising syringe needles of smaller inner diameters, which may require making changes in the parameters used for printing. For example, the present study did not set the wall thickness of the printed constructs to that of the diameters of the syringe needles. The present study maintained constant wall thicknesses of 0.5 mm while the majority of printing was conducting with 23 G needles which have inner diameters of 0.34 mm. Accuracy may well be improved when the wall thickness represents that of the diameter of the needle. Furthermore, an investigation into the effect hydrogel properties (such as alginate and calcium concentrations) have on achieving improved shape fidelity of the printed constructs may further be investigated for improving the accuracy of FRESH printed alginate hydrogels.

Printing (FRESH) cell-laden alginate hydrogels was also investigated in the study. However, consistent bacterial and fungal contamination of cell-laden constructs post-printing resulted in little success therein. Alginate hydrogels were successfully sterilised by autoclaving (120 ^{o}C) in previous experiments. Gelatin slurry sterilisation proved problematic, as slurries could not be heat sterilised due to gelatin micro particles dissolving into solution. An attempt was made to include antibiotic antimycotic (2 % (v/v) PSA) solution within gelatin slurries. However, constructs remained getting contaminated shortly after FRESH printing. UV sterilisation of the gelatin slurry was also attempted but proved unsuccessful. Gamma radiation may potentially allow for sufficient sterilisation of gelatin slurries, potentially enabling FRESH printing of cell-laden hydrogels.

Due to contamination of printed constructs, printing of ad-HMSC/HUVEC co-cultures in 2 % (w/v) alginate (in air) proved successful in one out of the three experiments conducted. Analysis of the successful bioprinting experiment revealed that cell viability at Day 1 was evident (Figure 5.3, Figure 5.5 B). Highlighting the fact that cells were able to withstand the printing process. However, viability drastically declined after 6 days of cell culture (Figure 5.4, Figure 5.5 B). In terms of FRESH printing, spatially defined deposition of sodium alginate was achieved to a certain degree. However, large amounts of over-printed areas resulted in relatively low printing accuracy.

Chapter 6: Conclusions & Future Work

6.1 Conclusions

The future of regenerative medicine will heavily rely on the advances made within the field of tissue engineering. A developing tissue engineering technique termed 3D bioprinting provides a rapid and robust approach for fabricating functional tissues *in vitro* (Jia *et al.*, 2014). However, large costs associated with commercially available, high-end bioprinters severely limit the amount of research groups with access to the technology. Recently, there have been increased efforts for achieving bioprinting at a relatively low cost. In this study, main aims were to achieve 3D bioprinting through utilising open-source designs such that a reproducible system capable of being optimised in terms of printing parameters may allow for 3D bioprinting of cell-laden sodium alginate hydrogels. In particular, fabrication of cell-laden ad-HMSC and HUVEC seeded alginate hydrogels was investigated.

Due to its open frame design and relatively low cost, the thermoplastic-based RepRap Prusa i3 3D printer was chosen as subject for modification such that bioprinting could be performed. A breakdown of the costs required for producing the system is presented in Table 6.1. Following assembly of the RepRap Prusa i3, syringe-housed extruder print-heads were developed for replacing the traditional plastic-based print-head. Utilising a standard NEMA 17 stepper motor taken from the original extruder, syringe-housed extruders could be controlled rather seamlessly when mounted to the X-carriage of the RepRap Prusa i3. Furthermore, a NEMA 17 stepper motor could be plugged directly into the extruder port of a RAMPS 1.4 board, requiring no adjustments made to the motor steps such that movement of a syringe plunger could be controlled. A syringe-housed screw-driven extruder was 3D printed in PLA using a RepRapPro Ormerod 3D printer (refer to section 3.2.1). Assembly and testing on the RepRap Prusa i3 revealed several undesirable characteristics of the extruder including instability about the X-carriage when printing agarose hydrogel, as well as insufficient syringe retraction. Developing additional extruder units was therefore investigated. The syringe-house universal paste extruder, designed by Richard Horne, was printed in PLA using a RepRap Wanhao Duplicator i3 (V2.1) 3D printer (3.2.2). Slight adjustments to the extruder body's mounting holes were made such that

the extruder could be directly mounted to the standard X-carriage of a RepRap Prusa i3. A similar approach was conducted in Armstrong *et al.* (2016), where a similar universal paste extruder was mounted to a MendelMax 2.0 3D printer and was subsequently used for bioprinting applications.

Table 6.1: Cost of materials required for producing the modified RepRap Prusa i3 3D printing system. ZAR to USD conversion based on exchange rates on January the 6th, 2017. Prices are rounded to the nearest whole number.

Material	Cost
Rep Rap Prusa i3 3D printer (including T8 lead screw upgrade)	ZAR 9 000 (655 USD)
Polylactic acid filament (single spool)	ZAR 270 (19 USD)
Non-printed components for universal paste extruder	ZAR 350 (25 USD)
Luer-lock syringes (10 mL, 100 pieces)	ZAR 140 (10 USD)
Assorted syringe needles (100 pieces)	ZAR 133 (10 USD)
Cell culture dishes (9.62 cm^2) (100 pieces)	ZAR 200 (15 USD)
Vivid Air biosafety cabinet	ZAR 35 000 (2 545 USD)
Total cost:	**ZAR 45 093 (3 279 USD)**

The inexpensive hydrogel, sodium alginate, was used as the primary material for 3D printing using the universal paste extruder in the present study. Alginate hydrogels have been largely investigated for tissue engineering applications, including those of bioprinting processes (Jia *et al.*, 2014; Duan *et al.*, 2012; Liberski, 2006). Largely due to the ability alginate gels have for structural modification, rapid polymerisation, as well as control of alginate physical properties, alginate based 3D cell culture systems demonstrate the ability for tissue/organ regeneration (Andersen *et al.*, 2015). Due to the aforementioned characteristics, the present study set out to investigate the printability of sodium alginate hydrogels using a modified RepRap Prusa i3 for both biological and non-biological 3D printing. Investigations into the effect needle gauge sizes had on the controlled deposition of alginate hydrogels revealed that the pressure required for initiating alginate extrusion would result in excessive dripping of hydrogel material when alginate was extruded using low-diameter needles. Contrastingly, larger needle diameters were able to provide sufficient pressure control within the syringe to allow for retaining hydrogel material in the absence of motor rotation (i.e. extrusion). Furthermore, it was found that material

viscosities (alginate concentration) also affect the ability for controlled material deposition. Higher viscosity solutions would require increased pressure for extrusion, resulting in slight over-extrusion of the hydrogel. Analysis of material flow-rate was later determined to also be affected by needle gauge size. Material rate of flow was found to uniformly increase with increasing needle gauge size. Results suggest that printing of complete constructs with little under or over-printing requires optimisation in several printing parameters, both software and hardware related.

Loss of large volumes of adipose tissue from tumor resection, traumatic injury or congenital defects often requires plastic or reconstructive surgery for repairing soft tissue (Gomillion & Berg, 2006). Due to autologous fat tissue damage from liposuction aspiration as well as the inability aspirates have for retaining the required level of vasculature (angiogenesis) for successful soft-tissue transplantation, adipose tissue engineering strategies have become widely investigated (Patrick, 2001). The present study investigated the ability unmodified alginate hydrogels have for allowing adipogenic-induced ad-HMSC and HUVEC encapsulation and maintaining cell viability after 7 days of culture. Live/dead staining of encapsulate alginate gels revealed that ad-HMSC viability was maintained through the 7 day culture period (refer to section 4.3.2). However, HUVEC cultures failed to fully encapsulate within alginate hydrogels, leading to a complete loss in cell viability over the 7 day culture period. Both ad-HMSC and HUVEC cultures failed to spread within unmodified alginate due to a lack of cell receptor binding, required for proper cell attachment. This resulted in cells displaying spherical morphologies. Printing of ad-HMSC/HUVEC co-cultured, cell-laden alginate bioinks, revealed cell viability after 1 day of culture. Indicating that cells were able to withstand the printing process using the modified RepRap Prusa i3, and that sterilisation of the system was sufficient. However, cell viability drastically decreased after 7 days of culture. Likely due to insufficient cell attachment to unmodified alginate, in addition to the lack of optimised cell culture media and cell densities, co-cultures failed to maintain viability after 6 additional days of culture. Printing of cell-laden alginate bioinks also resulted in deformation of the printed construct due to the lack of mechanical integrity alginate gels possess when in a liquid-state and printed in air.

To overcome the challenge of construct deformation and to achieve spatial control of printed alginate hydrogels, the newly developed printing method termed freeform reversible embedding

of suspended hydrogels (FRESH) was investigated. Freeform reversible embedding of suspended hydrogels printing was first described in Hinton *et al.* (2015), and involves embedding of a printed hydrogel within a secondary hydrogel, acting as a thermally reversible support structure which remains biocompatible. Freeform reversible embedding of suspended hydrogels printing was performed by deposition sodium alginate hydrogels within gelatin (type B) support baths comprising of blended gelatin micro particles and calcium ions which function to initiate alginate polymerisation. An investigation in to what the ideal blend time was for obtaining gelatin micro particles of low average area revealed that gelatin blended for 135 seconds produced low area particles which did not dissolve into solution. Printing of designs with simple geometries proved successful in that following FRESH printing of the alginate hydrogel, gelatin dissolving resulted in release of the printed construct. Slight dragging of alginate gel due to polymerisation within the syringe needle made printing complex designs, requiring material retraction, a lot more challenging. Printing accuracy of FRESH printed alginate hydrogels revealed large overlaps in the printed volume compared to that of the design volume. Optimisation in printing parameters as well as alginate/calcium concentrations is required for further improving printing accuracy.

6.2 Future Work

Future experiments could be carried out to investigate potential means for refining and improving the universal paste extruder. Scaling down of the extruder such as to house a smaller syringe may allow for improved control of material deposition. Additionally, use of sterilisable cone-shaped syringe-ends, similar to autopipette tips, could lower the cost of printing, improve printing accuracy and potentially aid in viability of 3D printed cell-laden hydrogels.

Depending on the material and construct to be printed, optimisation of printing parameters may greatly improve printing fidelity. Specifically, the material flow-rate, as well as printing speed, may be adjusted such as to optimise the printing process. Adjusting printing parameters accordingly will be required for accurately fabricating constructs based on the physical properties of bioink materials.

Bioink formulations may be further refined in terms of achieving optimal cell densities, culture conditions and hydrogel elastic properties, for achieving long-term cell culture and scaffold biodegradation. Partially oxidized sodium alginate hydrogels, which may be coupled to peptide

sequences, such as RGD motifs, have shown to significantly enhance cellular attachment through integrin binding, as well as aid in hydrogel degradation. Future experiments could include an investigation into the feasibility of utilising RGD-conjugated alginate hydrogels as scaffold bioink material for achieving adipose tissue engineering using the modified system.

To conclude, the present study investigated the feasibility for which modification of a RepRap Prusa i3 3D printer had for low-cost bioprinting via the use of open-source print-head designs. While the system developed proved somewhat successful in achieving the main aims of the study (fabricating cell-laden sodium alginate hydrogels for adipose tissue engineering), several steps to refine and optimise the system in terms of printing parameters, hydrogel characteristics and sterilisation techniques may pave the way for increasing printing fidelity, accuracy and long term viability of bioprinted cultures.

Chapter 7: References

1. Alavi, S. H., & Kheradvar, A. (2012). Metal mesh scaffold for tissue engineering of membranes. *Tissue Engineering. Part C, Methods*, *18*(4), 293–301. DOI: 10.1089/ten.TEC.2011.053
2. Alberts B., Johnson, A., Lewis, J., Raff, M., Roberts, K., & Walter, P. (2002). Molecular Biology of the Cell. 4th edition. New York: Garland Science. ISBN-10: 0-8153-4072-9. Retrieved from: https://www.ncbi.nlm.nih.gov/books/NBK21054
3. Alonzo, F., & Mayzaud, P. (1999). Spectrofluorometric quantification of neutral and polar lipids in zooplankton using Nile red. *Marine Chemistry*, *67*(3–4), 289–301. Retrieved from: http://www.sciencedirect.com/science/article/pii/S0304420399000754
4. Alvarez, K., & Nakajima, H. (2009). Metallic scaffolds for bone regeneration. *Materials*, *2*(3), 790–832. DOI: 10.3390/ma2030790
5. Andersen, T., Auk-Emblem, P., Dornish, M., Lornejad-Schä, M. R., & Schä, C. (2015). 3D Cell Culture in Alginate Hydrogels. *Microarrays*, *4*, 133–161. DOI: 10.3390/microarrays4020133
6. Angstmann, M., Brinkmann, I., Bieback, K., Breitkreutz, D., & Maercker, C. (2011). Monitoring human mesenchymal stromal cell differentiation by electrochemical impedance sensing. *Cytotherapy*, *13*(9), 1074–1089. DOI: 10.3109/14653249.2011.584863
7. Armstrong, J. P. K., Burke, M., Carter, B. M., Davis, S. A., & Perriman, A. W. (2016). 3D Bioprinting Using a Templated Porous Bioink. *Advanced Healthcare Materials*, *5*(14), 1724–1730. DOI: 10.1002/adhm.201600022
8. Atala, A. & Yoo, J.J. (2015). Essentials of 3D biofabrication and translation. London: Academic Press. ISBN: 978-0-12-800972-7.
9. Awad, H. A., Wickham, M. Q., Leddy, H. A., Gimble, J. M., & Guilak, F. (2004). Chondrogenic differentiation of adipose-derived adult stem cells in agarose, alginate, and gelatin scaffolds. *Biomaterials*, *25*(16), 3211-3222. DOI: 10.1016/j.biomaterials.2003.10.045

10. Badylak, S. F., Taylor, D., & Uygun, K. (2011). Whole-Organ Tissue Engineering: Decellularization and Recellularization of Three-Dimensional Matrix Scaffolds. *Annual Review of Biomedical Engineering*, *13*, 27–53. DOI: 10.1146/annurev-bioeng-071910-124743

11. Baer, P. C., & Geiger, H. (2012). Adipose-derived mesenchymal stromal/stem cells: Tissue localization, characterization, and heterogeneity. *Stem Cells International*, *11*(1), 1-11. DOI: 10.1155/2012/812693

12. Bagnaninchi, P. O., & Drummond, N. (2011). Real-time label-free monitoring of adipose-derived stem cell differentiation with electric cell-substrate impedance sensing. *Proceedings of the National Academy of Sciences of the United States of America*, *108*(16), 6462–64627. DOI: 10.1073/pnas.101826010

13. Barron, J. A., Wu, P., Ladouceur, H. D., & Ringeisen, B. R. (2004). Biological laser printing: A novel technique for creating heterogeneous 3-dimensional cell patterns. *Biomedical Microdevices*, *6*(2), 139–147. DOI: 10.1023/b:bmmd.0000031751.67267.9f

14. Barry, F. P., & Murphy, J. M. (2004). Mesenchymal stem cells: clinical applications and biological characterization. *The International Journal of Biochemistry & Cell Biology*, *36*(4), 568–84. DOI: 10.1016/j.biocel.2003.11.001

15. Bertassoni, L. E., Cardoso, J. C., Manoharan, V., Cristino, A. L., Bhise, N. S., Araujo, W. A., Zorlutuna, P., Vrana, N.E., Ghaemmaghami, A.M., Dokmeci, M.R., & Khademhosseini, A. (2014). Direct-write bioprinting of cell-laden methacrylated gelatin hydrogels. *Biofabrication*, *6*(2), e24105. DOI: 10.1088/1758-5082/6/2/024105

16. Bhattacharjee, T., Zehnder, S. M., Rowe, K. G., Jain, S., Nixon, R. M., Sawyer, W. G., & Angelini, T. E. (2015). Writing in the granular gel medium. *Science Advances*, *1*(8), e1500655. DOI: 10.1126/sciadv.1500655

17. Bidarra, S. J., Barrias, C. C., Fonseca, K. B., Barbosa, M. A., Soares, R. A., & Granja, P. L. (2011). Injectable in situ crosslinkable RGD-modified alginate matrix for endothelial cells delivery. *Biomaterials*, *32*(31), 7897–7904. DOI: 10.1016/j.biomaterials.2011.07.013

18. Bingham, E. C. (1916). An investigation of the laws of plastic flow. *Bulletin of the Bureau of Standards*, *13*, 309–353. DOI: 10.6028/bulletin.304

19. Borkenhagen, M., Clémence, J. F., Sigrist, H., & Aebischer, P. (1998). Three-dimensional extracellular matrix engineering in the nervous system. *Journal of Biomedical Materials Research*. *40*(3), 392-400. Retrieved from: https://www.ncbi.nlm.nih.gov/pubmed/9570070

20. Bouhadir, K. H., Lee, K. Y., Alsberg, E., Damm, K. L., Anderson, K. W., & Mooney, D. J. (2001). Degradation of partially oxidized alginate and its potential application for tissue engineering. *Biotechnology Progress*. DOI: 10.1021/bp010070p

21. Bouïs, D., Hospers, G. A. P., Meijer, C., Molema, G., & Mulder, N. H. (2001). Endothelium in vitro: A review of human vascular endothelial cell lines for blood vessel-related research. *Angiogenesis*, *4*(2), 91–102. DOI: 10.1023/A:1012259529167

22. Bunnell, B. A., Flaat, M., Gagliardi, C., Patel, B., & Ripoll, C. (2008). Adipose-derived stem cells: Isolation, expansion and differentiation. *Methods*, *45*(2), 115–120. DOI: 10.1016/j.ymeth.2008.03.006

23. Calderon, L., Collin, E., Velasco-Bayon, D., Murphy, M., O'Halloran, D., & Pandit, A. (2010). Type II collagen-hyaluronan hydrogel--a step towards a scaffold for intervertebral disc tissue engineering. *European Cells & Materials*, *20*, 134–48. DOI: vol020a12

24. Calvert, P. (2001). Inkjet printing for materials and devices. *Chemistry of Materials*, *13*(10), 3299-3305. DOI: 10.1021/cm0101632

25. Campbell, P. G., & Weiss, L. E. (2007). Tissue engineering with the aid of inkjet printers. *Expert Opinion in Biological therapy, 7*(8), 1123–1127. DOI: 10.1517/14712598.7.8.1123

26. Cao, Q., & Lin, Z. (2006). *Ganoderma lucidum* polysaccharides peptide inhibits the growth of vascular endothelial cell and the induction of VEGF in human lung cancer cell, *78*, 1457–1463. DOI: 10.1016/j.lfs.2005.07.017

27. Cao, Y. (2007). Angiogenesis modulates adipogenesis and obesity. *Journal of Clinical Investigation*, *117*(9), 2362-2368. DOI: 10.1172/JCI32239.2362

28. Chen, C. S. (2008). Mechanotransduction – a field pulling together? *Journal of Cell Science*, *121*(20), 3285–3292. DOI: 10.1242/jcs.023507

29. Chen, G., Ushida, T., & Tateishi, T. (2002). Scaffold design for tissue engineering. *Macromolecular Bioscience*, *2*(2), 67–77. DOI: 10.1002/1616-5195(20020201)2:2<67::aid-mabi67>3.0.co;2-f

30. Chen, T. H., Chen, W. M., Hsu, K. H., Kuo, C. D., & Hung, S. C. (2007). Sodium butyrate activates ERK to regulate differentiation of mesenchymal stem cells. *Biochemical and Biophysical Research Communications*, *355*(4), 913–918. DOI: 10.1016/j.bbrc.2007.02.057

31. Cheung, A. L. (2007). Isolation and Culture of Human Umbilical Vein Endothelial Cells (HUVEC). In *Current Protocols in Microbiology* (p. A.4B.1-A.4B.8). JohnWiley & Sons, Inc. DOI: 10.1002/9780471729259.mca04bs4

32. Chiu, Y. C., Cheng, M. H., Uriel, S., & Brey, E. M. (2011). Materials for engineering vascularized adipose tissue. *Journal of Tissue Viability*, *20*(2), 37–48. DOI: 10.1016/j.jtv.2009.11.005

33. Choi, Y. J., Park, J., & Lee, S. H. (2013). Size-controllable networked neurospheres as a 3D neuronal tissue model for Alzheimer's disease studies. *Biomaterials*, *34*(12), 2938–2946. DOI: 10.1016/j.biomaterials.2013.01.038

34. Chun, T. H., Hotary, K. B., Sabeh, F., Saltiel, A. R., Allen, E. D., & Weiss, S. J. (2006). A Pericellular Collagenase Directs the 3-Dimensional Development of White Adipose Tissue. *Cell*, *125*(3), 577–591. DOI: 10.1016/j.cell.2006.02.050

35. Cui, X., & Boland, T. (2009). Human microvasculature fabrication using thermal inkjet printing technology. *Biomaterials*, *30*(31), 6221–6227. DOI: 10.1016/j.biomaterials.2009.07.056

36. Cui, X., Breitenkamp, K., Finn, M. G., Lotz, M., & D 'Lima, D. D. (2012). Direct Human Cartilage Repair Using Three-Dimensional Bioprinting Technology. *Tissue Engineering: Part A*, *18*, 1304–1312. DOI: 10.1089/ten.tea.2011.0543

37. Cukierman, E., Pankov, R., Stevens, D. R., & Yamada, K. M. (2001). Taking cell-matrix adhesions to the third dimension. *Science*, *294*(5547), 1708–1712. DOI: 10.1126/science.1064829

38. Cummins, K (2010). "The rise of additive manufacturing". *The Engineer*. Available at: https://www.theengineer.co.uk/issues/24-may-2010/the-rise-of-additive-manufacturing/. Accessed 8 January 2017.

39. Dahl, S. L. M., Kypson, A. P., Lawson, J. H., Blum, J. L., Strader, J. T., Li, Y., Manson, R.J., Tente, W.E., Hensley, M.T., Carter, R., Williams, T.P., Prichard, H.L., Dey, M.S., Bengelman, K.G., & Niklason, L. E. (2011). Readily Available Tissue-Engineered Vascular Grafts. *Science Translational Medicine*, *3*(68), 68ra9-68ra9. DOI: 10.1126/scitranslmed.3001426

40. Dang, J. M., & Leong, K. W. (2006). Natural polymers for gene delivery and tissue engineering. *Advanced Drug Delivery Reviews*, *58*(4), 487-499. DOI: 10.1016/j.addr.2006.03.001

41. Davidenko, N., Campbell, J. J., Thian, E. S., Watson, C. J., & Cameron, R. E. (2010). Collagen-hyaluronic acid scaffolds for adipose tissue engineering. *Acta Biomaterialia*, *6*(10), 3957-3968. DOI: 10.1016/j.actbio.2010.05.005

42. Dennis, S. G., Trusk, T., Richards, D., Jia, J., Tan, Y., Mei, Y., Fann, S., Markwald, R., & Yost, M. (2015). Viability of Bioprinted Cellular Constructs Using a Three Dispenser Cartesian Printer. *Journal of Visualized Experiments*, *103*, DOI: 10.3791/53156

43. Derby, B. L. (2012). Printing and Prototyping of Tissues and Scaffolds. *Science*, *338*(November), 921–927. DOI: 10.1126/science.1226340

44. Drury, J. L., & Mooney, D. J. (2003). Hydrogels for tissue engineering: Scaffold design variables and applications. *Biomaterials*. DOI: 10.1016/S0142-9612(03)00340-5

45. Duan, B., Hockaday, L. A., Kang, K. H., & Butcher, J. T. (2013). 3D Bioprinting of heterogeneous aortic valve conduits with alginate/gelatin hydrogels. *Journal of Biomedical Materials Research - Part A*, *101 A*(5), 1255–1264. DOI: 10.1002/jbm.a.34420

46. Egorov, V., Tsyuryupa, S., Kanilo, S., Kogit, M., & Sarvazyan, A. (2008). Soft tissue elastometer. *Medical Engineering and Physics*, *30*(2), 206–212. DOI: 10.1016/j.medengphy.2007.02.007

47. Engler, A. J., Sen, S., Sweeney, H. L., & Discher, D. E. (2006). Matrix Elasticity Directs Stem Cell Lineage Specification. *Cell*, *126*(4), 677–689. DOI: 10.1016/j.cell.2006.06.044

48. Favot, L., Keravis, T., Holl, V., Le Bec, A., & Lugnier, C. (2003). VEGF-induced HUVEC migration and proliferation are decreased by PDE2 and PDE4 inhibitors. *Thrombosis and Haemostasis*, *90*(2), 334–343. DOI: 10.1160/th03-02-0084

49. Fernández, E., Lopez, D., Mijangos, C., Duskova-Smrckova, M., Ilavsky, M., & Dusek, K. (2008). Rheological and thermal properties of agarose aqueous solutions and hydrogels. *Journal of Polymer Science, Part B: Polymer Physics*, *46*, 322-328. DOI: 10.1002/polb.21370

50. Friedenstein, A.J., Piatetzky-Shapiro, I.I., & Petrakova, K.V. (1966). Osteogenesis in transplants of bone marrow cells. *Journal of Embryology and Experimental Morphology*, *16*(3), 381–390. Retrieved from: https://www.ncbi.nlm.nih.gov/pubmed/5336210

51. Ghaemmaghami Fernández, E., Lopez, D., Mijangos, C., Duskova-Smrckova, M., Ilavsky, M., & Dusek, K. (2008). Rheological and thermal properties of agarose aqueous solutions and hydrogels. *Journal of Polymer Science, Part B: Polymer Physics*. DOI: 10.1002/polb.21370

52. Ghaemmaghami, A. M., Hancock, M. J., Harrington, H., Kaji, H., & Khademhosseini, A. (2012). Biomimetic tissues on a chip for drug discovery. *Drug Discovery Today*. DOI: 10.1016/j.drudis.2011.10.029

53. Gloria, A., De Santis, R., & Ambrosio, L. (2010). Polymer-based composite scaffolds for tissue engineering. *Journal of Applied Biomaterials & Biomechanics*, *8*(2), 57–67. Retrieved from: https://www.ncbi.nlm.nih.gov/pubmed/20740467

54. Golez, E., Barruet, E., Hsiao, E., Schepers, K., Presnbell, S., Nguyen, D., & Retting, K. (2014). Three-dimensional (3D) bone tissues derived from stem cells as a novel model for mineralization, in: Stem Cell Meeting on the Mesa, La Jolla, CA. Retrieved from: http://organovo.com/three-dimensional-3d-bone-tissues-derived-from-stem-cells-as-a-novel-model-for-mineralization

55. Golez, E., Barruet, E., Hsiao, E., Schepers, K., Presnbell, S., Nguyen, D., & Retting, K. (2014). Three-dimensional (3D) bone tissues derived from stem cells as a novel model for mineralization, in: Stem Cell Meeting on the Mesa, La Jolla, CA. Retrieved from: http://organovo.com/wp-content/uploads/2015/07/SCMOM_2014_Poster-Final-copy-Web.pdf

56. Gomillion, C. T., & Burg, K. J. L. (2006). Stem cells and adipose tissue engineering. *Biomaterials*, *27*(36), 6052-6063. DOI: 10.1016/j.biomaterials.2006.07.033

57. Greenspan, P., Mayer, E. P., & Fowler, S. D. (1985). Nile red: a selective fluorescent stain for intracellular lipid droplets, *Journal of Cell Biology*, *100*(3), 965–973. *The Journal of Cell Biology*, *100*(10), 965–973. DOI: 10.1083/jcb.100.3.965

58. Gregoire, F. M., Smas, C. M., & Sul, H. S. (1998). Understanding adipocyte differentiation. *Physiological Reviews*, *78*(3), 783–809. DOI: 10.1074/jbc.272.8.5128

59. Harland, B., Walcott, S., & Sun, S. X. (2011). Adhesion dynamics and durotaxis in migrating cells. *Physical Biology*, *8*(1), 15011. DOI: 10.1088/1478-3975/8/1/015011

60. Hausman, G. J., & Richardson, R. L. (2004). Adipose tissue angiogenesis. *Journal of Animal Science*, *82*(3), 925–934. Retrieved from: https://www.ncbi.nlm.nih.gov/pubmed/15032451

61. Hildebrandt, C., Büth, H., Cho, S., Impidjati., & Thielecke, H. (2010). Detection of the osteogenic differentiation of mesenchymal stem cells in 2D and 3D cultures by electrochemical impedance spectroscopy. *Journal of Biotechnology*, *148*(1), 83–90. DOI: 10.1016/j.jbiotec.2010.01.007

62. Hinton, T. J., Hudson, A., Pusch, K., Lee, A., & Feinberg, A. W. (2016). 3D Printing PDMS Elastomer in a Hydrophilic Support Bath via Freeform Reversible Embedding. *ACS Biomaterials Science and Engineering*, *2*(10), 1781–1786. DOI: 10.1021/acsbiomaterials.6b00170

63. Hinton, T. J., Jallerat, Q., Palchesko, R. N., Park, J. H., Grodzicki, M. S., Shue, H.J., Ramadan, M.H., Hudson, A.R., & Feinberg, A. W. (2015). Three-dimensional printing of complex biological structures by freeform reversible embedding of suspended hydrogels. *Science Advances, 1* (9), e1500758. DOI: 10.1126/sciadv.1500758

64. Hoshiba, T., Chen, G., Endo, C., Maruyama, H., Wakui, M., Nemoto, E., Kawazoe, N., & Tanaka, M. (2016). Decellularized extracellular matrix as an in vitro model to study the comprehensive roles of the ECM in stem cell differentiation. *Stem Cells International*, *2016*, 6397820. DOI: 10.1155/2016/6397820

65. Huber, B., Borchers, K., Nter, G., Tovar, E., & Kluger, P. J. (2016). Methacrylated gelatin and mature adipocytes are promising components for adipose tissue engineering. *Journal of Biomaterials Applications*, *30*(6), 699-710. DOI: 10.1177/0885328215587450

66. Huh, D., Hamilton, G. A., & Ingber, D. E. (2011). From 3D cell culture to organs-on-chips. *Trends in Cell Biology*, *21*(12), 745-754. DOI: 10.1016/j.tcb.2011.09.005

67. Ikada, Y. (2006). Challenges in tissue engineering. *Journal of the Royal Society Interface*. *3*(10), 589-601. DOI:10.1098/rsif.2006.0124

68. Jakab, K., Damon, B., Neagu, A., Kachurin, A., & Forgacs, G. (2006). Three-dimensional tissue constructs built by bioprinting. *Biorheology*, *43*, 509–513. Available at: https://www.ncbi.nlm.nih.gov/pubmed/16912422

69. Jakab, K., Norotte, C., Marga, F., Murphy, K., Vunjak-Novakovic, G., & Forgacs, G. (2010). Tissue engineering by self-assembly and bio-printing of living cells. *Biofabrication*, *2*(2), 022001. DOI: 10.1088/1758-5082/2/2/022001

70. Janderova, L., McNeil, M., Murrell, a N., Mynatt, R. L., & Smith, S. R. (2003). Human mesenchymal stem cells as an in vitro model for human adipogenesis. *Obesity Research*, *11*(1), 65–74. DOI: 10.1038/oby.2003.11

71. Jeon, O., Bouhadir, K. H., Mansour, J. M., & Alsberg, E. (2009). Photocrosslinked alginate hydrogels with tunable biodegradation rates and mechanical properties. *Biomaterials*, *30*(14), 2724–2734. DOI: 10.1016/j.biomaterials.2009.01.034

72. Jia, J., Richards, D. J., Pollard, S., Tan, Y., Rodriguez, J., Visconti, R. P., Trusk, T.C., Yost, M.J., Yao, H., markwald, R.R. & Mei, Y. (2014). Engineering alginate as bioink for bioprinting. *Acta Biomaterialia*, *10*(10), 4323-4331. DOI: 10.1016/j.actbio.2014.06.034

73. Jones, R., Haufe, P., Sells, E., Iravani, P., Olliver, V., Palmer, C., & Bowyer, A. (2011). RepRap – the replicating rapid prototyper. *Robotica*, *29*, 177–191. DOI: 10.1017/S026357471000069X

74. Jung, J. P., Bhuiyan, D. B., & Ogle, B. M. (2016). Solid organ fabrication: comparison of decellularization to 3D bioprinting. *Biomaterials Research*, *20*(1), 27. DOI: 10.1186/s40824-016-0074-2

75. Kachgal, S., & Putnam, A. J. (2011). Mesenchymal stem cells from adipose and bone marrow promote angiogenesis via distinct cytokine and protease expression mechanisms. *Angiogenesis*, *14*(1), 47–59. DOI: 10.1007/s10456-010-9194-9

76. Kaklamani, G., Cheneler, D., Grover, L. M., Adams, M. J., & Bowen, J. (2014). Mechanical properties of alginate hydrogels manufactured using external gelation. *Journal of the Mechanical Behavior of Biomedical Materials*, *36*, 135–142. DOI: 10.1016/j.jmbbm.2014.04.013

77. Kang, J. H., Gimble, J. M., & Kaplan, D. L. (2009). In Vitro 3D Model for Human Vascularized Adipose Tissue. *Tissue Engineering Part A*, *15*(8), 2227-2236. DOI: 10.1089/ten.tea.2008.0469

78. Kang, S. W., Cha, B. H., Park, H., Park, K. S., Lee, K. Y., & Lee, S. H. (2011). The Effect of Conjugating RGD into 3D Alginate Hydrogels on Adipogenic Differentiation of Human Adipose-Derived Stromal Cells. *Macromolecular Bioscience*, *11*(5), 673–679. DOI: 10.1002/mabi.201000479

79. Kar, S., Slowikowski, S. P. M., Westaway, D., & Mount, H. T. J. (2004). Interactions between β -amyloid and central cholinergic neurons : implications for Alzheimer ' s disease, *29*(6), 427–442. Available at: https://www.ncbi.nlm.nih.gov/pmc/articles/PMC524960

80. Kershaw, E. E., & Flier, J. S. (2004). Adipose Tissue as an Endocrine Organ. *Cellular Endocrinology in Health and Disease*, *89*(6), 2548-2556. DOI: 10.1210/jc.2004-0395

81. Khalil, S., & Sun, W. (2009). Bioprinting Endothelial Cells With Alginate for 3D Tissue Constructs. *Journal of Biomechanical Engineering*, *131*(11), e111002. DOI: 10.1115/1.3128729.

82. Khatiwala, C., Law, R., Shepherd, B., Dorfman, S., & Csete, M. (2012). 3D Cell Bioprinting for Regenerative Medicine Research and Therapies. G*ene Therapy and Regulation*, *7*(1), e1230004. DOI: 10.1142/s1568558611000301

83. King, S.M., Gorgen, V., Presnell, S.C., Nguyen, D.G., & Shepherd, B.R. (2013). Development of 3D bioprinted human breast cancer for in vitro screening of therapeutics targeted against cancer progression. American Society of Biology, New Orleans, LA. Retrieved from: http://organovo.com/wp-content/uploads/2015/07/12-12-13_ASCB_Poster_Final_SMK-low-res.pdf

84. Kinkel, A. D., Fernyhough, M. E., Helterline, D. L., Vierck, J. L., Oberg, K. S., Vance, T. J., Hausman, G.J., Hill, R.A., & Dodson, M.V. (2005). Oil red-O stains non-adipogenic cells : a precautionary note, *Cytotechnology, 46*(1), 49–56. DOI: 10.1007/s10616-004-3903-4

85. Kohane, D. S., & Langer, R. (2008). Polymeric Biomaterials in Tissue Engineering. *Pediatric Research*, *63*(5), 487–491. DOI: 10.1203/01.pdr.0000305937.26105.e7

86. Kolesky, D. B., Truby, R. L., Gladman, A. S., Busbee, T. A., Homan, K. A., & Lewis, J. A. (2014). 3D bioprinting of vascularized, heterogeneous cell-laden tissue constructs. *Advanced Materials*, *26*(19), 3124–3130. DOI: 10.1002/adma.201305506

87. Kramer, A. H., Joos-Vandewalle, J., Edkins, A. L., Frost, C. L., & Prinsloo, E. (2014). Real-time monitoring of 3T3-L1 preadipocyte differentiation using a commercially available electric cell-substrate impedance sensor system. *Biochemical and Biophysical Research Communications*, *443*(4), 1245–50. DOI: 10.1016/j.bbrc.2013.12.123

88. Krouskop, T. A, Wheeler, T. M., Kallel, F., Garra, B. S., & Hall, T. (1998). Elastic moduli of breast and prostate tissues under compression. *Ultrasonic Imaging*, *20*(4), 260-274. Retrieved form: http://journals.sagepub.com/doi/abs/10.1177/016173469802000403

89. Kuznetsova, T. G., Starodubtseva, M. N., Yegorenkov, N. I., Chizhik, S. A., & Zhdanov, R. I. (2007). Atomic force microscopy probing of cell elasticity. *Micron*, *38*(8), 824–833. DOI: 10.1016/j.micron.2007.06.011

90. Lee, K. Y., & Mooney, D. J. (2001). Hydrogels for tissue engineering. *Chemical Reviews*, *101*(7), 1869-1879. DOI: 10.1021/cr000108x

91. Liberski, A. R. (2016). Three-dimensional printing of alginate: From seaweeds to heart valve scaffolds. *QScience Connect*, *2016*(2), 3. DOI: 10.5339/connect.2016.3

92. Lin, C. C., & Anseth, K. S. (2009). PEG hydrogels for the controlled release of biomolecules in regenerative medicine. *Pharmaceutical Research*, *26*(3), 631-643. DOI: 10.1007/s11095-008-9801-2

93. Lin, D. C., Dimitriadis, E. K., & Horkay, F. (2007). Robust strategies for automated AFM force curve analysis-II: adhesion-influenced indentation of soft, elastic materials. *Journal of Biomechanical Engineering*, *129*(6), 904–912. DOI: 10.1115/1.2800826

94. Lin-Gibson, S., Bencherif, S., Cooper, J. A., Wetzel, S. J., Antonucci, J. M., Vogel, B. M., Horkay, F., & Washburn, N. R. (2004). Synthesis and characterization of PEG Dimethacrylates and their hydrogels. *Biomacromolecules*, *5*(4), 1280–1287. DOI: 10.1021/bm0498777

95. Locke, M., Feisst, V., & Dunbar, P. R. (2011). Concise review: Human adipose-derived stem cells: Separating promise from clinical need. *Stem Cells*, *29*(3), 404–411. DOI: 10.1002/stem.593

96. López-Álvarez, M., Rodríguez-Valencia, C., Serra, J., & González, P. (2013). Bio-inspired ceramics: Promising scaffolds for bone tissue engineering. *Procedia Engineering*, 59, 51–58. http://dx.doi.org/10.1016/j.proeng.2013.05.093

97. Lourenço, A.F.H.F. (2011). 'The influence of cell density and culture conditions within 3D hydrogel matrices on mesenchymal stem cells behavior', Master of Biomedical Engineering, University of Porto, Porto, Portugal.

98. Lu, T.-Y., Lin, B., Kim, J., Sullivan, M., Tobita, K., Salama, G., & Yang, L. (2013). Repopulation of decellularized mouse heart with human induced pluripotent stem cell-derived cardiovascular progenitor cells. *Nature Communications*, *4*, 2307. DOI: 10.1038/ncomms3307

99. Mandrycky, C., Wang, Z., Kim, K., & Kim, D. H. (2015). 3D bioprinting for engineering complex tissues. *Biotechnology Advances*, *34*(4), 422-434. DOI: 10.1016/j.biotechadv.2015.12.011

100. Marga, F., Jakab, K., Khatiwala, C., Shepherd, B., Dorfman, S., Hubbard, B., … Gabor, F. (2012). Toward engineering functional organ modules by additive manufacturing. *Biofabrication*, *4*(2), 22001. Retrieved from http://www.ncbi.nlm.nih.gov/pubmed/22406433

101. Mauney, J. R., Nguyen, T., Gillen, K., Kirker-Head, C., Gimble, J. M., & Kaplan, D. L. (2007). Engineering adipose-like tissue in vitro and in vivo utilizing human bone marrow and adipose-derived mesenchymal stem cells with silk fibroin 3D scaffolds. *Biomaterials*, *28*(35), 5280-5290. DOI: 10.1016/j.biomaterials.2007.08.017

102. Melchels, F. P., Dhert, W.J.A., Hutmacher, D.W., & Malda, J. (2014). Development and characterisation of a new bioink for additive tissue manufacturing. *Journal of Materials Chmistry* B, *2*, 2282-2289. DOI: 10.1039/c3tb21280g

103. Meshel, A. S., Wei, Q., Adelstein, R. S., & Sheetz, M. P. (2005). Basic mechanism of three-dimensional collagen fibre transport by fibroblasts. *Nature Cell Biology*, *7*(2), 157–164. DOI: 10.1038/ncb1216

104. Miller, J. S. (2014). The Billion Cell Construct: Will Three-Dimensional Printing Get Us There? *PLoS Biology*, *12*(6), e1001882. DOI: 10.1371/journal.pbio.1001882

105. Miller, J. S., Stevens, K. R., Yang, M. T., Baker, B. M., Nguyen, D.-H. T., Cohen, D. M., Toro, E., Chem, A.A., Galie, P.A., Yu, X., Chaturvaedi, R., Bhatia, S.N., & Chen, C.

S. (2012). Rapid casting of patterned vascular networks for perfusable engineered three-dimensional tissues. *Nature Materials*, *11*(7), 768–774. DOI: 10.1038/nmat3357

106. Mironov, V., Kasyanov, V., Drake, C., & Markwald, R. R. (2008). Organ printing: promises and challenges. *Regenerative Medicine*, *3*(1), 93–103. Retrieved from http://ovidsp.ovid.com/ovidweb.cgi?T=JS&PAGE=reference&D=med5&NEWS=N&AN=18154465

107. Mironov, V., Visconti, R. P., Kasyanov, V., Forgacs, G., Drake, C. J., & Markwald, R. R. (2009). Organ printing: Tissue spheroids as building blocks. *Biomaterials*, *30*(12), 2164-2174. DOI: 10.1016/j.biomaterials.2008.12.084

108. Mizuno, H., Tobita, M., & Uysal, A. C. (2012). Concise review: Adipose-derived stem cells as a novel tool for future regenerative medicine. *Stem Cells*, *30*(5), 804-810. DOI: 10.1002/stem.1076

109. Muller, M., Gennisson, J. L., Deffieux, T., Tanter, M., & Fink, M. (2009). Quantitative Viscoelasticity Mapping of Human Liver Using Supersonic Shear Imaging: Preliminary In Vivo Feasability Study. *Ultrasound in Medicine and Biology*, *35*(2), 219–229. DOI: 10.1016/j.ultrasmedbio.2008.08.018

110. Murphy, S. V. & Atala, A. (2014). 3D bioprinting of tissues and organs. *Nature Biotechnology*, *32*(8), 773-785. DOI: 10.1038/nbt.2958

111. Nakatsu, M. N., Sainson, R. C. A., Aoto, J. N., Taylor, K. L., Aitkenhead, M., Pérez-del-Pulgar, S., … Hughes, C. C. W. (2003). Angiogenic sprouting and capillary lumen formation modeled by human umbilical vein endothelial cells (HUVEC) in fibrin gels: The role of fibroblasts and Angiopoietin-1. *Microvascular Research*, *66*(2), 102–112. DOI: 10.1016/S0026-2862(03)00045-1

112. Nichol, J. W., Koshy, S. T., Bae, H., Hwang, C. M., Yamanlar, S., & Khademhosseini, A. (2010). Cell-laden microengineered gelatin methacrylate hydrogels. *Biomaterials*, *31*(21), 5536-5544. DOI: 10.1016/j.biomaterials.2010.03.064

113. Nicolas, A., Geiger, B., & Safran, S. A. (2004). Cell mechanosensitivity controls the anisotropy of focal adhesions. *Proceedings of the National Academy of Sciences of the United States of America*, *101*(34), 12520–5. DOI: 10.1073/pnas.0403539101

114. Normand, V., D.L.Lootens, Amici, E., Plucknett, K. P., & Aymard, P. (2000). New Insight into Agarose Gel Mechanical Properties. *Biomacromolecules*, *1*(4), 730–738. DOI: 10.1021/bm005583j

115. O'Brien, F. J. (2011). Biomaterials & scaffolds for tissue engineering. *Materials Today*, *14*(3), 88–95. DOI: 10.1016/S1369-7021(11)70058-X

116. Okabe, K., Yamada, Y., Ito, K., Kohgo, T., Yoshimi, R., & Ueda, M. (2009). Injectable soft-tissue augmentation by tissue engineering and regenerative medicine with human mesenchymal stromal cells, platelet-rich plasma and hyaluronic acid scaffolds. *Cytotherapy*, *11*(3), 307–16. Retrieved from http://www.ncbi.nlm.nih.gov/pubmed/19333802

117. Ozbolat, I. T., & Hospodiuk, M. (2016). Current advances and future perspectives in extrusion-based bioprinting. *Biomaterials*, *76*, 321–343. DOI: 10.1016/j.biomaterials.2015.10.076

118. Pampaloni, F., Reynaud, E. G., & Stelzer, E. H. K. (2007). The third dimension bridges the gap between cell culture and live tissue. *Nature Reviews Molecular Cell Biology*, *8*(10), 839–845. DOI: 10.1038/nrm2236

119. Pataky, K., Braschler, T., Negro, A., Renaud, P., Lutolf, M. P., & Brugger, J. (2012). Microdrop printing of hydrogel bioinks into 3D tissue-like geometries. *Advanced Materials*, *24*(3), 391–396. DOI: 10.1002/adma.201102800

120. Pati, F., Ha, D. H., Jang, J., Han, H. H., Rhie, J. W., & Cho, D. W. (2015). Biomimetic 3D tissue printing for soft tissue regeneration. *Biomaterials*, *62*, 164-175. DOI: 10.1016/j.biomaterials.2015.05.043

121. Pati, F., Jang, J., & Ha, D.-H. (2014). Printing three-dimensional tissue analogues with decellularized extracellular matrix bioink. *Nature Communications*, *5*(9), 3935. DOI: 10.1038/ncomms4935

122. Pati, F., Jang, J., Lee, J. W., & Cho, D. W. (2015). Extrusion bioprinting. In *Essentials of 3D Biofabrication and Translation*, 123–152. DOI: 10.1016/B978-0-12-800972-7.00007-4

123. Patrick, C. W. (2001). Tissue engineering strategies for adipose tissue repair. *The Anatomical Record*, *263*(4), 361–366. DOI: 10.1002/ar.1113

124. Pei, P., Qi, X., Du, X., Zhu, M., Zhao, S., & Zhu, Y. (2016). Three-dimensional printing of tricalcium silicate/mesoporous bioactive glass cement scaffolds for bone tissue regeneration. *Journal of Materials Chemistry B*, *4*, 7452-7463. DOI: 10.1039/C6TB02055K

125. Peltola, S. M., Melchels, F. P. W., Grijpma, D. W., & Kellomäki, M. (2008). A review of rapid prototyping techniques for tissue engineering purposes. *Annals of Medicine*, *40*(4), 268–280. DOI: 10.1080/07853890701881788.

126. Petersen, O. W., Rønnov-Jessen, L., Howlett, A. R., & Bissell, M. J. (1992). Interaction with basement membrane serves to rapidly distinguish growth and differentiation pattern of normal and malignant human breast epithelial cells. *Proceedings of the National Academy of Sciences of the United States of America*, *89*(19), 9064–9068. Retrieved from: http://www.jstor.org/stable/2360332

127. Pittenger, M. F. (1999). Multilineage Potential of Adult Human Mesenchymal Stem Cells. *Science*, *284*(5411), 143–147. DOI: 10.1126/science.284.5411.143

128. Pittenger, M. F., Mackay, a M., Beck, S. C., Jaiswal, R. K., Douglas, R., Mosca, J. D., Moorman, M.A., Simonetti, D.W., Craig, S., & Marshak, D. R. (1999). Multilineage potential of adult human mesenchymal stem cells. *Science (New York, N.Y.)*, *284*(5411), 143–147. DOI: 10.1126/science.284.5411.143

129. Plotnikov, S. V., Pasapera, A. M., Sabass, B., & Waterman, C. M. (2012). Force fluctuations within focal adhesions mediate ECM-rigidity sensing to guide directed cell migration. *Cell*, *151*(7), 1513–1527. DOI: 10.1016/j.cell.2012.11.034

130. *Prusa i3*, 2016. RepRap. Available at: http://reprap.org/wiki/Prusa_i3. Accessed 8 December 2016.

131. *Prusa Mendel (Iteration 2)*, 2016. RepRap. Available at: http://reprap.org/wiki/Prusa_i2. Accessed 8 December 2016,

132. Re'em, T., Tsur-Gang, O., & Cohen, S. (2010). The effect of immobilized RGD peptide in macroporous alginate scaffolds on TGF-beta1-induced chondrogenesis of human mesenchymal stem cells. *Biomaterials*, *31*(26), 6746–6755. DOI: 10.1016/j.biomaterials.2010.05.025

133. Reitinger, S., Wissenwasser, J., Kapferer, W., Heer, R., & Lepperdinger, G. (2012). Electric impedance sensing in cell-substrates for rapid and selective multipotential

differentiation capacity monitoring of human mesenchymal stem cells. *Biosensors and Bioelectronics*, *34*(1), 63–69. DOI: 10.1016/j.bios.2012.01.013

134. *RepRap*, 2016. RepRap. Available at: http://reprap.org/. Accessed 8 January 2017.

135. Rowley, J. A., Madlambayan, G., & Mooney, D. J. (1999). Alginate hydrogels as synthetic extracellular matrix materials. *Biomaterials*, *20*(1), 45–53. Retrieved from: https://www.ncbi.nlm.nih.gov/pubmed/9916770

136. Scarritt, M. E., Pashos, N. C., & Bunnell, B. A. (2015). A review of cellularization strategies for tissue engineering of whole organs. *Frontiers in Bioengineering and Biotechnology*, *3*(March), 43. DOI: 10.3389/fbioe.2015.00043

137. Scott, M. A., Nguyen, V. T., Levi, B., & James, A. W. (2011). Current methods of adipogenic differentiation of mesenchymal stem cells. *Stem Cells and Development*, *20*(10), 1793–804. Retrieved from http://www.pubmedcentral.nih.gov/articlerender.fcgi?artid=3182038&tool=pmcentrez&rendertype=abstract

138. Seebach, C., Schultheiss, J., Wilhelm, K., Frank, J., & Henrich, D. (2010). Comparison of six bone-graft substitutes regarding to cell seeding efficiency , metabolism and growth behaviour of human mesenchymal stem cells (MSC) in vitro. *Injury*, *41*(7), 731–738. DOI: 10.1016/j.injury.2010.02.017

139. Seol, Y. J., Kang, H. W., Lee, S. J., Atala, A., & Yoo, J. J. (2014). Bioprinting technology and its applications. *European Journal of Cardio-Thoracic Surgery*. DOI: 10.1093/ejcts/ezu148

140. Shoichet, M. S., Li, R. H., White, M. L., & Winn, S. R. (1996). Stability of hydrogels used in cell encapsulation: An in vitro comparison of alginate and agarose. *Biotechnology and Bioengineering*, *50*(4), 374–381. DOI: 10.1002/(SICI)1097-0290(19960520)50:4<374::AID-BIT4>3.0.CO;2-I

141. Smidsrød, O., & Skjak-Braek, G. (2000). Alginate as immobilization matrix for cells. *Minerva Biotecnologica*, *12*(4), 223–233. DOI: 10.1016/0167-7799(90)90139-O

142. Sodian, R., Lemke, T., Fritsche, C., Hoerstrup, S. P., Fu, P., Potapov, E. V., Hausmann, H., & Hetzer, R. (2002). Tissue-engineering bioreactors: a new combined cell-seeding and perfusion system for vascular tissue engineering. *Tissue Engineering*, *8*(5), 863–870. DOI: 10.1089/10763270260424222

143. Song, S. J., Choi, J., Park, Y. D., Hong, S., Lee, J. J., Ahn, C. B., Choi, H., & Sun, K. (2011). Sodium Alginate Hydrogel-Based Bioprinting Using a Novel Multinozzle Bioprinting System. *Artificial Organs*, *35*(11), 1132-1136. DOI: 10.1111/j.1525-1594.2011.01377.x

144. Sterodimas, A., De Faria, J., Nicaretta, B., & Pitanguy, I. (2010). Tissue engineering with adipose-derived stem cells (ADSCs): Current and future applications. *British Journal of Plastic Surgery*, *63*, 1886–1892. DOI: 10.1016/j.bjps.2009.10.028

145. Takahashi, K., & Yamanaka, S. (2006). Induction of Pluripotent Stem Cells from Mouse Embryonic and Adult Fibroblast Cultures by Defined Factors. *Cell*, *126*(4), 663-676. DOI: 10.1016/j.cell.2006.07.024

146. Tasoglu, S., & Demirci, U. (2013). Bioprinting for stem cell research. *Trends in Biotechnology*, *31*(1), 10-19. DOI: 10.1016/j.tibtech.2012.10.005

147. *The story of RepRap Prusa Mendel*, 2014. Makingsociety. *MakingSoceity* Available at: http://makingsociety.com/2014/01/reprap-prusa-mendel-3d-printing-podcast. Accessed 8 December 2016.

148. Tønnesen, H. H., & Karlsen, J. (2002). Alginate in drug delivery systems. *Drug Development and Industrial Pharmacy*, *28*(6), 621–630. DOI: 10.1081/DDC-120003853

149. Vacanti, J., & Langer, R. (1999). Tissue engineering: the design and fabrication of living replacement devices for surgical reconstruction and transplantation. *Lancet*, *354*(Supp I), 32-34. DOI: 10.1016/S0140-6736(99)90247-7

150. Van Den Bulcke, A. I., Bogdanov, B., De Rooze, N., Schacht, E. H., Cornelissen, M., & Berghmans, H. (2000). Structural and Rheological Properties of Methacrylamide Modified Gelatin Hydrogels. *Biomacromolecules*, *1*(1), 31-38. DOI: 10.1021/bm990017d

151. Van Vlierberghe, S., Dubruel, P., & Schacht, E. (2011). Biopolymer-based hydrogels as scaffolds for tissue engineering applications: A review. *Biomacromolecules*, *12*(5), 1387-1408. DOI: 10.1021/bm200083n

152. Wall, M. E., Bernacki, S. H., & Loboa, E. G. (2007). Effects of serial passaging on the adipogenic and osteogenic differentiation potential of adipose-derived human mesenchymal stem cells. *Tissue Engineering*, *13*(6), 1291–1298. DOI:10.1089/ten.2006.0275

153. Wang, L., Shansky, J., Borselli, C., Mooney, D., & Vandenburgh, H. (2012). Design and fabrication of a biodegradable, covalently crosslinked shape-memory alginate scaffold for cell and growth factor delivery. *Tissue Engineering Part A*, *18*(19–20), 2000–2007. DOI: 10.1089/ten.tea.2011.0663

154. Wang, N., Butler, J. P., & Ingber, D. E. (1993). Mechanotransduction Across the Cell Surface and Through the Cytoskeleton. *Science*. *260*(5111), 1124-1127. DOI: 10.1126/science.7684161

155. Wang, X.F., Song, Y., Liu, Y.-S., Sun, Y., Wang, Y., Wang, Y., & Lyu, P.J. (2016). Osteogenic Differentiation of Three- Dimensional Bioprinted Constructs Consisting of Human Adipose-Derived Stem Cells In Vitro and In Vivo. *PLoS ONE*, *11*(6), e0157214. DOI: 10.1371/journal.pone.0157214

156. Wei, X., Yang, X., Han, Z., Qu, F., Shao, L., & Shi, Y. (2013). Mesenchymal stem cells: a new trend for cell therapy. *Acta Pharmacologica Sinica*, *34*(6), 747–54. DOI: 10.1038/aps.2013.50

157. Wells, P. N. T., & Liang, H.D. (2011). Medical ultrasound: imaging of soft tissue strain and elasticity. *Journal of The Royal Society Interface*, *8*(64), 1521–1549. Retrieved from: http://rsif.royalsocietypublishing.org/content/early/2011/06/16/rsif.2011.0054

158. Winer, J. P., Oake, S., & Janmey, P. A. (2009). Non-linear elasticity of extracellular matrices enables contractile cells to communicate local position and orientation. *PLoS ONE*, *4*(7). DOI: 10.1371/journal.pone.0006382

159. Wong, W. H., & Mooney, D. J. (1997). Synthesis and Properties of Biodegradable Polymers Used as Synthetic Matrices for Tissue Engineering. In A. Atala & D. J. Mooney (Eds.), *Synthetic Biodegradable Polymer Scaffolds* (51–82), Boston, MA. Boston. DOI: 10.1007/978-1-4612-4154-6_4

160. Wu, Z., Su, X., Xu, Y., Kong, B., Sun, W., & Mi, S. (2016). Bioprinting three-dimensional cell-laden tissue constructs with controllable degradation. *Scientific Reports*, *6*, 24474. DOI: 10.1038/srep24474

161. Yao, R., Zhang, R., Lin, F., & Luan, J. (2013). Biomimetic injectable HUVEC-adipocytes/collagen/alginate microsphere co-cultures for adipose tissue engineering. *Biotechnology and Bioengineering*, *110*(5), 1430–1443. DOI: 10.1002/bit.24784

162. Yarak, S., & Okamoto, O. K. (2010). Human adipose-derived stem cells: current challenges and clinical perspectives. *Anais Brasileiros de Dermatologia*, *85*(5), 647–656. DOI: 10.1590/S0365-05962010000500008

163. Yu, G., Floyd, Z. E., Wu, X., Hebert, T., Halvorsen, Y. C., Buehrer, B. M., & Gimble, J. M. (2011). Adipogenic differentiation of adipose-derived stem cells. *Methods in Molecular Biology*, *702*, 193–200. DOI: 10.1007/978-1-61737-960-4_14

164. Zhu, Y., Dong, Z., Wejinya, U. C., Jin, S., & Ye, K. (2011). Determination of mechanical properties of soft tissue scaffolds by atomic force microscopy nanoindentation. *Journal of Biomechanics*, *44*(13), 2356-2361. DOI: 10.1016/j.jbiomech.2011.07.010

Chapter 8: Supplementary Material

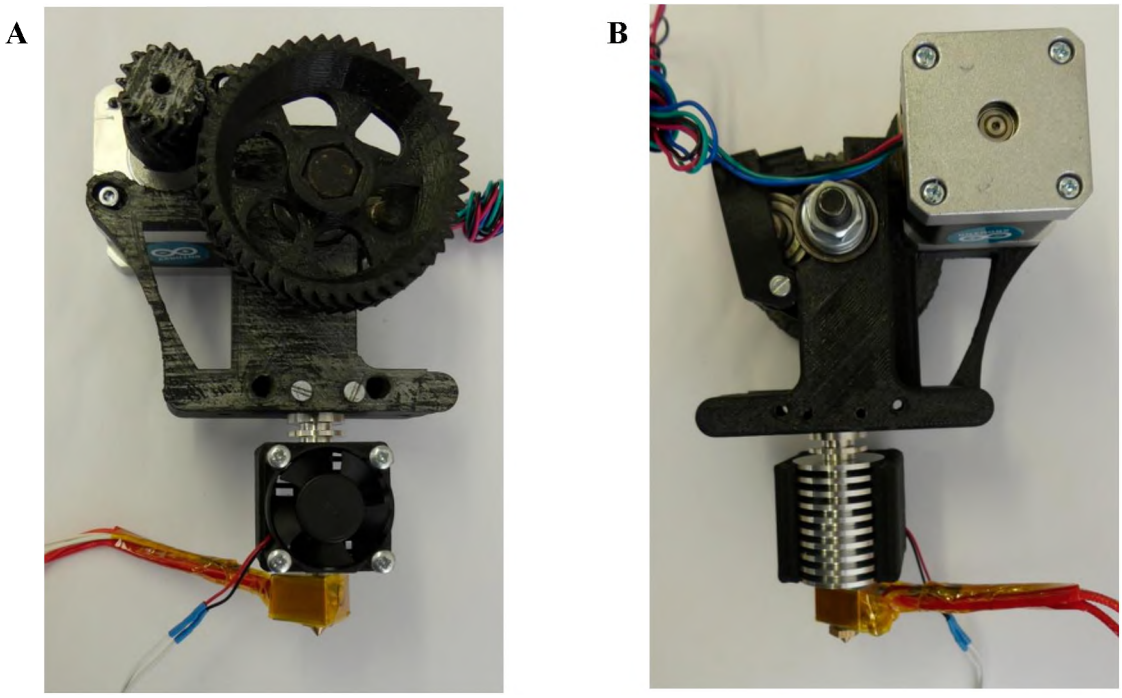

Figure S1: Greg's Wade thermoplastic RepRap Prusa i3 extruder. A: Front view. B: Back view.

Figure S2: Polylactic acid (PLA) 3D printed part printed using the RepRap Prusa i3.

Figure S3: Vivid Air biosafety cabinet used for housing the RepRap Prusa i3 3D printer. The cabinet included a broad-range UV sterilisation lamp as well as an air filter.

Video S1: Polylactic acid (PLA) printing using the RepRap Prusa i3.

Video S2: Agarose printing using the RepRap Prusa i3 modified with a screw-driven extruder.

Video S3: Freeform reversible embedding of suspended hydrogels (FRESH) printing of a sodium alginate grid structure.

G-code 1: G-code for printing square constructs (10 mm x 10 mm x 2 mm). Pronterface controller software was used for controlling the printer. The print head was positioned over a plastic culture dish using X, Y & Z offsets prior to initiating the printing process. Print speed was set to 2 mm/s in Cura software.

- ;Basic settings: Layerheight: 1 Walls: 0.5 Fill: 0
- ;Print time: 1 minutes
- ;Filament cost: None
- ;M190 S0 ;Uncomment to add your own bed temperature line
- ;M109 S0 ;Uncomment to add your own temperature line
- G21 ;metric values
- G90 ;absolute positioning
- M82 ;set extruder to absolute mode
- M107 ;start with the fan off
- G92 E0 ;zero the extruded length
- G92 E0 ;zero the extruded length again
- G1 F9000
- ;Put printing message on LCD screen
- M117 Printing...
- ;TweakAtZ instances: 1
- ;Layer count: 2
- ;LAYER:0
- G0 F9000 X95.250 Y95.250 Z1.000
- ;TYPE:WALL-OUTER
- G1 F240 E0.00000
- G1 F120 X104.750 Y95.250 E1.20958
- G1 X104.750 Y104.750 E2.41916
- G1 X95.250 Y104.750 E3.62873
- G1 X95.250 Y95.250 E4.83831
- G0 F9000 X95.750 Y95.750
- G1 F120 X95.750 Y104.250 E5.92056
- G1 X104.250 Y104.250 E7.00282
- G1 X104.250 Y95.750 E8.08507
- G1 X95.750 Y95.750 E9.16732
- ;LAYER:1
- G0 F9000 X95.750 Y95.750 Z2.000
- ;TYPE:WALL-OUTER
- G1 F120 X95.750 Y104.250 E10.24958
- G1 X104.250 Y104.250 E11.33183
- G1 X104.250 Y95.750 E12.41409
- G1 X95.750 Y95.750 E13.49634
- G0 F9000 X95.250 Y95.250
- G1 F120 X104.750 Y95.250 E14.70592
- G1 X104.750 Y104.750 E15.91549
- G1 X95.250 Y104.750 E17.12507
- G1 X95.250 Y95.250 E18.33465
- M107
- G1 F240 E13.33465
- G0 F9000 X95.250 Y95.250 Z7.000
- ;TweakAtZ V4.0.2: executed at 7.00 mm
- M117 Printing... tw@ 7.0
- ;End GCode
- G91 ;relative positioning
- G1 E-1 F300 ;retract the filament a bit before lifting the nozzle, to release some of the pressure
- G1 Z+0.5 E-5 X-20 Y-20 F9000 ;move Z up a bit and retract filament even more
- G28 X0 Y0 ;move X/Y to min endstops, so the head is out of the way
- M84 ;steppers off
- G90 ;absolute positioning

G-code 2: G-code for printing grid constructs (19 mm x 10 mm x 2 mm). Pronterface controller software was used for controlling the printer. The print head was positioned over a plastic culture dish using X, Y & Z offsets prior to initiating the printing process. Print speed was set to 2 mm/s in Cura software.

- ;Basic settings: Layerheight: 1 Walls: 0.5 Fill: 0
- ;Print time: 2 minutes
- ;Filament cost: None
- ;M190 S0 ;Uncomment to add your own bed temperature line
- ;M109 S0 ;Uncomment to add your own temperature line
- G21 ;metric values
- G90 ;absolute positioning
- M82 ;set extruder to absolute mode
- M107 ;start with the fan off
- G92 E0 ;zero the extruded length
- G92 E0 ;zero the extruded length again
- G1 F9000
- ;Put printing message on LCD screen
- M117 Printing...
- ;TweakAtZ instances: 1
- ;Layer count: 2
- ;LAYER:0
- G0 F9000 X90.750 Y95.250 Z1.000
- ;TYPE:WALL-OUTER
- G1 F240 E0.00000
- G1 F120 X109.250 Y95.250 E2.35549
- G1 X109.250 Y104.750 E3.56507
- G1 X100.750 Y104.750 E4.64732
- G1 X100.750 Y104.250 E4.71099
- G1 X108.750 Y104.250 E5.72958
- G1 X108.750 Y95.750 E6.81183
- G1 X100.250 Y95.750 E7.89409
- G1 X100.250 Y103.896 E8.93127
- G1 X99.396 Y104.750 E9.08504
- G1 X90.750 Y104.750 E10.18588
- G1 X90.750 Y95.250 E11.39546
- G0 F9000 X91.250 Y95.750
- G1 F120 X91.250 Y104.250 E12.47771
- G1 X99.750 Y104.250 E13.55997
- G1 X99.750 Y95.750 E14.64222
- G1 X91.250 Y95.750 E15.72448
- ;LAYER:1
- G0 F9000 X91.250 Y95.750 Z2.000
- ;TYPE:WALL-OUTER
- G1 F120 X91.250 Y104.250 E16.80673
- G1 X99.750 Y104.250 E17.88898
- G1 X99.750 Y95.750 E18.97124
- G1 X91.250 Y95.750 E20.05349
- G0 F9000 X90.750 Y95.250
- G1 F120 X109.250 Y95.250 E22.40898
- G1 X109.250 Y104.750 E23.61856
- G1 X100.750 Y104.750 E24.70081
- G1 X100.750 Y104.250 E24.76448
- G1 X108.750 Y104.250 E25.78307
- G1 X108.750 Y95.750 E26.86532
- G1 X100.250 Y95.750 E27.94757
- G1 X100.250 Y103.896 E28.98476
- G1 X99.396 Y104.750 E29.13853
- G1 X90.750 Y104.750 E30.23937
- G1 X90.750 Y95.250 E31.44895
- M107
- G1 F240 E26.44895
- G0 F9000 X90.750 Y95.250 Z7.006
- ;TweakAtZ V4.0.2: executed at 7.01 mm

- M117 Printing... tw@ 7.0
- ;End GCode
- G91 ;relative positioning
- G1 E-1 F300 ;retract the filament a bit before lifting the nozzle, to release some of the pressure
- G1 Z+0.5 E-5 X-20 Y-20 F9000 ;move Z up a bit and retract filament even more
- G28 X0 Y0 ;move X/Y to min endstops, so the head is out of the way
- M84 ;steppers off
- G90 ;absolute positioning

G-code 3: G-code for printing a Rhodes University (RU) construct. Pronterface controller software was used for controlling the printer. The print head was positioned over a plastic culture dish using X, Y & Z offsets prior to initiating the printing process. Print speed was set to 2 mm/s in Cura software.

- ;Basic settings: Layer height: 1 Walls: 0.5 Fill: 0
- ;Print time: 1 minutes
- ;Filament used: 0.023m 0.0g
- ;Filament cost: None
- G21 ;metric values
- G90 ;absolute positioning
- M82 ;set extruder to absolute mode
- M107 ;start with the fan off
- G92 E0 ;zero the extruded length
- G92 E0 ;zero the extruded length again
- G1 F9000
- ;Put printing message on LCD screen
- M117 Printing...
- ;TweakAtZ instances: 1
- ;Layer count: 2
- ;LAYER:0
- G0 F9000 X93.703 Y95.779 Z1.000
- ;TYPE:WALL-OUTER
- G1 F240 E0.00000
- G1 F120 X94.099 Y95.779 E0.05042
- G1 X94.099 Y100.034 E0.59218
- G1 X94.462 Y100.137 E0.64023
- G1 X97.175 Y95.779 E1.29384
- G1 X97.465 Y95.779 E1.33076
- G1 X94.058 Y100.889 E2.11274
- G1 X94.199 Y101.153 E2.15085
- G1 X97.682 Y101.153 E2.59432
- G1 X97.682 Y104.236 E2.98686
- G1 X93.703 Y104.236 E3.49348
- G1 X93.703 Y95.779 E4.57026
- G1 F240 E-0.42974
- G0 F9000 X94.099 Y101.549
- G1 F240 E4.57026
- G1 F120 X94.099 Y103.840 E4.86196
- G1 X97.286 Y103.840 E5.26774
- G1 X97.286 Y101.549 E5.55944
- G1 X94.099 Y101.549 E5.96522
- G1 F240 E0.96522
- G0 F9000 X99.632 Y104.221
- G1 F240 E5.96522
- G1 F120 X99.632 Y95.764 E7.04200
- G1 X106.297 Y95.764 E7.89061
- G1 X106.297 Y104.221 E8.96739
- G1 X105.901 Y104.221 E9.01781
- G1 X105.901 Y96.160 E10.04417
- G1 X100.026 Y96.160 E10.79220
- G1 X100.026 Y104.221 E11.81856
- G1 X99.632 Y104.221 E11.86872

- ;LAYER:1
- G1 F240 E6.86872
- G0 F9000 X97.682 Y104.236 Z2.000
- ;TYPE:WALL-OUTER
- G1 F240 E11.86872
- G1 F120 X93.703 Y104.236 E12.37535
- G1 X93.703 Y95.779 E13.45212
- G1 X94.099 Y95.779 E13.50254
- G1 X94.099 Y100.034 E14.04431
- G1 X94.462 Y100.137 E14.09235
- G1 X97.175 Y95.779 E14.74597
- G1 X97.465 Y95.779 E14.78289
- G1 X94.058 Y100.889 E15.56487
- G1 X94.199 Y101.153 E15.60297
- G1 X97.682 Y101.153 E16.04644
- G1 X97.682 Y104.236 E16.43898
- G0 F9000 X97.286 Y103.840
- G1 F120 X97.286 Y101.549 E16.73068
- G1 X94.099 Y101.549 E17.13646
- G1 X94.099 Y103.840 E17.42816
- G1 X97.286 Y103.840 E17.83394
- G1 F240 E12.83394
- G0 F9000 X99.632 Y104.221
- G1 F240 E17.83394
- G1 F120 X99.632 Y95.764 E18.91072
- G1 X106.297 Y95.764 E19.75934
- G1 X106.297 Y104.221 E20.83612
- G1 X105.901 Y104.221 E20.88654
- G1 X105.901 Y96.160 E21.91289
- G1 X100.026 Y96.160 E22.66092
- G1 X100.026 Y104.221 E23.68728
- G1 X99.632 Y104.221 E23.73745
- M107
- G1 F240 E18.73745
- G0 F9000 X99.632 Y104.221 Z6.791
- ;TweakAtZ V4.0.2: executed at 6.79 mm
- M117 Printing... tw@ 6.8
- ;End GCode
- G91 ;relative positioning
- G1 E-1 F300 ;retract the filament a bit before lifting the nozzle, to release some of the pressure
- G1 Z+0.5 E-5 X-20 Y-20 F9000 ;move Z up a bit and retract filament even more
- G28 X0 Y0 ;move X/Y to min endstops, so the head is out of the way
- M84 ;steppers off
- G90 ;absolute positioning

G-code 4: G-code for printing single layer rectangular constructs (15 mm x 10 mm x 1 mm). Pronterface controller software was used for controlling the printer. The print head was positioned over a plastic culture dish using X, Y & Z offsets prior to initiating the printing process. Print speed was set to 2 mm/s in Cura software.

- ;Basic settings: Layerheight: 1 Walls: 0.5 Fill: 0
- ;Print time: 0 minutes
- ;Filament cost: None
- ;M190 S0 ;Uncomment to add your own bed temperature line
- ;M109 S0 ;Uncomment to add your own temperature line
- G21 ;metric values
- G90 ;absolute positioning
- M82 ;set extruder to absolute mode
- M107 ;start with the fan off
- G92 E0 ;zero the extruded length
- G92 E0 ;zero the extruded length again
- G1 F9000

- ;Put printing message on LCD screen
- M117 Printing...
- ;TweakAtZ instances: 1
- ;Layer count: 1
- ;LAYER:0
- G0 F9000 X99.760 Y92.751 Z1.000
- ;TYPE:WALL-OUTER
- G1 F240 E0.00000
- G1 F120 X100.259 Y92.750 E0.06353
- G1 X100.259 Y107.249 E1.90960
- G1 X99.747 Y107.249 E1.97479
- G1 X99.760 Y92.751 E3.82074
- M107
- G1 F240 E-1.17926
- G0 F9000 X99.760 Y92.751 Z6.007
- ;TweakAtZ V4.0.2: executed at 6.01 mm
- M117 Printing... tw@ 6.0
- ;End GCode
- G91 ;relative positioning
- G1 E-1 F300 ;retract the filament a bit before lifting the nozzle, to release some of the pressure
- G1 Z+0.5 E-5 X-20 Y-20 F9000 ;move Z up a bit and retract filament even more
- G28 X0 Y0 ;move X/Y to min endstops, so the head is out of the way
- M84 ;steppers off
- G90 ;absolute positioning

G-code 5: G-code for printing dual layer rectangular constructs (15 mm x 10 mm x 2 mm). Pronterface controller software was used for controlling the printer. The print head was positioned over a plastic culture dish using X, Y & Z offsets prior to initiating the printing process. Print speed was set to 2 mm/s in Cura software.

- ;Basic settings: Layer height: 1 Walls: 0.5 Fill: 0
- ;Print time: 0 minutes
- ;Filament cost: None
- ;M190 S0 ;Uncomment to add your own bed temperature line
- ;M109 S0 ;Uncomment to add your own temperature line
- G21 ;metric values
- G90 ;absolute positioning
- M82 ;set extruder to absolute mode
- M107 ;start with the fan off
- G92 E0 ;zero the extruded length
- G92 E0 ;zero the extruded length again
- G1 F9000
- ;Put printing message on LCD screen
- M117 Printing...
- ;TweakAtZ instances: 1
- ;Layer count: 2
- ;LAYER:0
- G0 F9000 X99.760 Y92.751 Z1.000
- ;TYPE:WALL-OUTER
- G1 F240 E0.00000
- G1 F120 X100.259 Y92.750 E0.06353
- G1 X100.259 Y107.250 E1.90973
- G1 X99.747 Y107.249 E1.97492
- G1 X99.760 Y92.751 E3.82087
- ;LAYER:1
- G0 F9000 X99.760 Y92.751 Z2.000
- ;TYPE:WALL-OUTER
- G1 F120 X100.259 Y92.750 E3.88440
- G1 X100.259 Y107.249 E5.73047
- G1 X99.758 Y107.250 E5.79426
- G1 X99.747 Y107.250 E5.79566
- G1 X99.760 Y92.751 E7.64173
- M107

- G1 F240 E2.64173
- G0 F9000 X99.760 Y92.751 Z7.014
- ;TweakAtZ V4.0.2: executed at 7.01 mm
- M117 Printing... tw@ 7.0
- ;End GCode
- G91 ;relative positioning
- G1 E-1 F300 ;retract the filament a bit before lifting the nozzle, to release some of the pressure
- G1 Z+0.5 E-5 X-20 Y-20 F9000 ;move Z up a bit and retract filament even more
- G28 X0 Y0 ;move X/Y to min endstops, so the head is out of the way
- M84 ;steppers off
- G90 ;absolute positioning